

**A MARINE MAGNETOTELLURIC STUDY OF THE
SAN DIEGO TROUGH, PACIFIC OCEAN, USA**

A Thesis

Presented to the

Faculty of

San Diego State University

In Partial Fulfillment

of the Requirements for the Degree

Master of Science

in

Geological Sciences

by

Lisl Laura Lewis

Summer 2005

SAN DIEGO STATE UNIVERSITY

The Undersigned Faculty Committee Approves the

Thesis of Lisl Laura Lewis:

A Marine Magnetotelluric Study of the San Diego Trough, Pacific Ocean, USA

George Jiracek, Chair
Department of Geological Sciences

Robert Mellors
Department of Geological Sciences

Robert Nelson
Department of Physics

Steven Constable
Institute for Geophysical and Planetary Physics
Scripps Institution of Oceanography

Approval Date

Copyright © 2005

by

Lisl Laura Lewis

All Rights Reserved

ABSTRACT OF THE THESIS

A Marine Magnetotelluric Study of the San Diego Trough,
Pacific Ocean, USA

by

Lisl Laura Lewis

Master of Science in Geological Sciences

San Diego State University, 2005

Several expeditions to the San Diego Trough (SDT) offshore San Diego resulted in the acquisition of ten marine magnetotelluric (MMT) seafloor sites in a profile across the SDT. The MMT method measures the passive electric and magnetic signals from the Earth's interaction with the Sun, and results in calculations of the subsurface resistivity at the location of the seafloor sites.

The SDT is an 1100 m deep basin located 30 miles west of the city of San Diego and flanked by the Thirtymile Bank to the west and the Coronado Bank to the east. These bathymetric features are part of the California continental borderland, the broad tectonic plate boundary between the Pacific and North American plates. Previous geophysical and geological studies conducted in the region have resulted in the mapping and interpretation of the shallow (top 2-3 km below the seafloor) geologic structure, but no studies have been able to image the deeper structure of the SDT area.

The data from this MMT investigation suggest a geoelectric structure that agrees with the seismic data in the top 2-3 km but introduces new evidence for deeper structure. Several faults are identified in the San Diego Trough and evidence suggests that the Coronado Bank Fault Zone is active, perhaps similar to the "creeping" segment of the San Andreas Fault in Parkfield, California.

TABLE OF CONTENTS

	PAGE
ABSTRACT.....	iv
LIST OF TABLES.....	viii
LIST OF FIGURES.....	ix
ACKNOWLEDGEMENTS.....	xii
 CHAPTER	
1 INTRODUCTION.....	1
2 BACKGROUND GEOLOGY.....	4
California Continental Borderland Region.....	4
Lithologic Units.....	6
Tectonic History.....	7
San Diego Trough.....	8
Thirtymile Bank.....	10
Large-Scale Landslides.....	11
Coronado Bank.....	12
Previous Work.....	13
3 THEORY AND METHODOLOGY.....	15
Seafloor Resistivity.....	15
Physical Properties.....	15
Porosity Effects.....	16
The Magnetotelluric Method.....	18
Magnetotelluric Theory.....	20

Quasi-Static Approximation	21
Plane-Wave Assumption.....	24
1-D Case.....	24
TE and TM Modes	26
Seafloor MT	28
Seafloor MT Instrumentation.....	33
History.....	33
SIO Seafloor MT Receiver	35
Magnetic and Electric Sensors.....	36
Electronics.....	37
Operation.....	39
The San Diego Trough Experiment	41
Geologic Structure of San Diego Trough Area.....	41
Instruments and Deployments.....	42
Processing Procedure	43
4 RESULTS	45
Three Expeditions: An Overview	45
Frequency Domain Responses.....	52
Noisy Short Period Data	52
3-D Effects	53
Negative Phases	53
Rotations and Decomposition.....	55
Groom-Bailey Decomposition.....	59
“ <i>Strike</i> ” Program.....	60
Inversion	61

Regularized Inversion Methods	61
2-D WinGLink	62
Inversion Process	63
Modeling Results	64
Comparison of Models.....	66
Persistent Features	66
5 DISCUSSION.....	68
Persistent Features	68
(1) Conductive Shallow Sediments.....	70
Sediment Thickness	70
Clay Effects.....	73
Heat Flow, Porosity and Temperature	73
Turbidity Channels.....	75
(2) Undulating Basal Boundary That Dips to the East	78
(3) Narrow Conductor in Eastern Part of the Basin.....	80
(4) Resistive Section Off the Profile to the East.....	80
(5) Conductive Region Off the Profile to the West	82
6 CONCLUSIONS.....	83
Active Faulting.....	84
Similarities to the San Andreas Fault.....	85
REFERENCES	87
APPENDICES	
A GROOM-BAILEY DECOMPOSITION	95
B APPARENT RESISTIVITY AND PHASE PLOTS	107
C DATA FITS	114

LIST OF TABLES

	PAGE
Table 1. Ranges of Rock Resistivities	42
Table 2. SDT-1.....	45
Table 3. SDT-2.....	46
Table 4. SDT-3.....	46

LIST OF FIGURES

	PAGE
Figure 1. Regional elevation map of the California continental borderland.....	4
Figure 2. Regional tectonostratigraphic terranes of the California continental borderland	5
Figure 3. Schematic cross section of the southern California margin.	8
Figure 4. Bathymetric map of the offshore San Diego Trough region	9
Figure 5. Fault plane geometries for the major faults in the San Diego Trough area.....	10
Figure 6. Bathymetric map across the San Diego Trough	11
Figure 7. Seismic line USGS-112.....	12
Figure 8. The naturally-occurring electromagnetic energy spectrum	19
Figure 9. Attenuation of the electric field amplitude at various depths.....	23
Figure 10. Attenuation of the electric and magnetic fields due to a layer of seawater	29
Figure 11. Forward model response of seafloor MT site in 1000 m of seawater with 300 m of sediments (1.5 Ω m) underlying the site	30
Figure 12. Forward model response of seafloor MT site in 1000 m of seawater with 300 m of resistive rocks (10 Ω m) underlying the site	31
Figure 13. Forward model response of seafloor MT site in 1000 m of seawater with 300 m of sediments (1.5 Ω m) underlying the site and a 300 m topographic high adjacent to the site.....	32
Figure 14. Electric and magnetic field distortions due to a sinusoidal topography in both the land and seafloor environment.....	32
Figure 15. Apparent resistivities and phases from TM and TE modes in both the land and seafloor environments	33
Figure 16. Electric current lines in the seafloor environment.....	34
Figure 17. The modern SIO seafloor MMT receiver.....	35

Figure 18. Magnetic induction coils during the manufacturing process at SIO	36
Figure 19. Schematic diagram of a Ag-AgCl electrode identifying all of the featured components	37
Figure 20. The SIO Mark III data logger, with key features identified	38
Figure 21. SIO custom acoustic unit in a deep water pressure case	38
Figure 22. The mechanical release attaches the frame to the concrete anchor via an anchor cable	39
Figure 23. Seafloor MT receiver being deployed	40
Figure 24. Cartoon drawing of the MT seafloor receivers	40
Figure 25. The process flow for handling MMT data	44
Figure 26. Frequency vs. time plot of Site S05	48
Figure 27. “Disk write” noise in ten minutes of time series data from sites S04, S05 and S06	49
Figure 28. One hour of time series data from sites S01, S02, S03, S04, S05 and S06	50
Figure 29. One hour of time series data from sites S07, A02, S08 and S09	51
Figure 30. One hour of time series data from sites S10 and S1151	
Figure 31. G-B analysis for Site S05	54
Figure 32. Site S09 apparent resistivity and phase curves	55
Figure 33. Apparent resistivity and phase results before and after G-B decomposition	57
Figure 34. Trade-off between RMS misfit and tau (smoothing parameter) values	64
Figure 35. Undecomposed inversion model and decomposed inversion model using G-B analysis	67
Figure 36. Joint modes 2-D inversion preferred model of the San Diego Trough	69
Figure 37. Seismic line USGS-112 with notable features identified	72
Figure 38. The variation of conductivity with increasing temperature	74
Figure 39. Calculated pore-fluid conductivity with depth based on a geothermal gradient of 150° C/ km	75

Figure 40. A 2-D gravity model of the towed gravity measurements across the San Diego Trough.....	76
Figure 41. Heat flow distribution and turbidity current channels across the San Diego Trough.....	77
Figure 42. Fault plane geometries for the major faults in the San Diego Trough area.....	81
Figure 43. Polar diagram of site S01.	108
Figure 44. Polar diagram of site S02.	108
Figure 45. Polar diagram of site A02.....	109
Figure 46. Polar diagram of site S03.	109
Figure 47. Polar diagram of site S05.	110
Figure 48. Polar diagram of site S11.	110
Figure 49. Polar diagram of site S10.	111
Figure 50. Polar diagram of site S09.	111
Figure 51. Polar diagram of site S08.	112
Figure 52. Polar diagram of site S07.	112
Figure 53. Polar diagram of site S06.	113
Figure 54. Site S06.....	115
Figure 55. Site S07.....	116
Figure 56. Site A02.....	117
Figure 57. Site S10.....	118
Figure 58. Site S11.....	119
Figure 59. Site S08.....	120
Figure 60. Site S03.....	121
Figure 61. Site S09.....	122
Figure 62. Site S02.....	123
Figure 63. Site S01.....	124

ACKNOWLEDGEMENTS

There were more than a few moments during the past 4 years when I was extremely close to abandoning this effort. The reason that I persisted was purely because of the sideline cheering and support that I received from a handful of people in my life – Rob Evans, Kerry Key, Steve Constable and Arnold Orange were the loudest in encouraging me to not give up. Rob Evans especially devoted a lot of his time and patience to helping me get through this, even though he had no direct affiliation or reason to do so other than his generous nature. I am so grateful for this support.

I also would like to thank the management of A.G.O. (AOA Geomarine Operations) for allowing my work schedule to be flexible when needed, my committee members at SDSU and SIO for their ideas and editorial support, and my husband Rhodri for making sure that I stayed nourished and sane during the dark times.

CHAPTER 1

INTRODUCTION

Over the past decade, the San Diego Trough (SDT) has been a testing ground for the development of the marine magnetotelluric (MMT) receiver by Scripps Institution of Oceanography (SIO). The marine magnetotelluric (MMT) method is the technique of tapping into the earth's natural electromagnetic energy by measuring simultaneous orthogonal magnetic and electric fields and using these data to calculate the electrical resistivity distribution. Electrical resistivity is one of the physical properties of the Earth that can be measured and can be used to differentiate between different kinds of rocks. This is an especially useful geophysical tool when the geologic situation or target is not visible on the surface of the Earth. The subset of the electromagnetic geophysical method that utilizes the Earth's natural electromagnetic field is magnetotellurics.

The MMT receiver is the piece of geophysical equipment that was developed for carrying out MMT measurements at the bottom of the ocean. The proximity to SIO, easy access for local vessels, a flat seafloor in 1100 m of water, and the two-dimensional (2-D) bathymetric structure of the area make the SDT an ideal location for implementing new ideas on how to make seafloor MMT measurements. Prior to the set of experiments described in this thesis, collecting useful MMT measurements in strategic locations and actually interpreting the data from a geological point of view was never a priority.

Interest in the geologic structure of the area swelled after the author took a course in Extensional Tectonics from Dr. Mark Legg at San Diego State University. Dr. Legg's

passion for the offshore California continental borderland (CCB) region inspired the author and her thesis committee. The CCB region is part of the broad tectonic boundary between the North American plates and the Pacific plate. Most of this region is underwater, and therefore relatively little is known about the forces that have shaped this complicated plate boundary.

MMT is an ideal tool for mapping the geologic structure at depth, since the technique is sensitive to contrasts in resistivity. Although the geologic structure of the Earth can often be evaluated at the Earth's surface and then extrapolated down into the deeper part of the Earth's crust, it is only by measuring the physical properties of the rocks using remote sensing geophysical techniques such as seismic, gravity, or electromagnetic methods that insight is gained on the geologic structure at depth. The distribution of resistivity contrasts can provide another perspective of the geologic structure, with emphasis on the pore fluid distribution, offering insight into tectonic activity. Overall rock resistivity can be overwhelmingly influenced by the presence of pore fluids in the rock.

The resulting union of the MMT development expeditions to the SDT and the subsequent analysis of the geoelectric structure of the area is far from conclusive, but the results detailed in this thesis highlight geologic features that may have a significant impact on the population of southern California. The differing electrical properties of subsurface geologic rock units make MMT investigations such as this one useful in differentiating the distribution of the rock types at depth. Evidence for active faulting in the SDT area, only 50 km from the California coastline, indicates an earthquake hazard perhaps not fully recognized.

Chapter 2 describes the regional geology of southern California, with primary focus on the offshore San Diego area. Chapter 3 explains the theory and methodology of marine magnetotellurics and specifically the work that was carried out for the purpose of this thesis. The results of the thesis work and the observations regarding those data are described in Chapter 4. Chapter 5 is a discussion of those results and an interpretation of what the results mean in the context of the regional geological situation. The conclusions that are drawn are detailed in Chapter 6.

CHAPTER 2

BACKGROUND GEOLOGY

CALIFORNIA CONTINENTAL BORDERLAND REGION

The California continental borderland (CCB), located offshore Southern California, is a geologically complex part of the broad tectonic boundary between the North American and Pacific plates. The CCB spans the approximate area from Point Arguello in the north ($\sim 34.5^\circ$ N) to Cedros Island in the south ($\sim 28.5^\circ$ N), and from the mainland California coast to the Patton Escarpment located 270 km to the west (Moore, 1969) (Figure 1). Half of the borderland region lies south of the international border between the USA and Mexico.

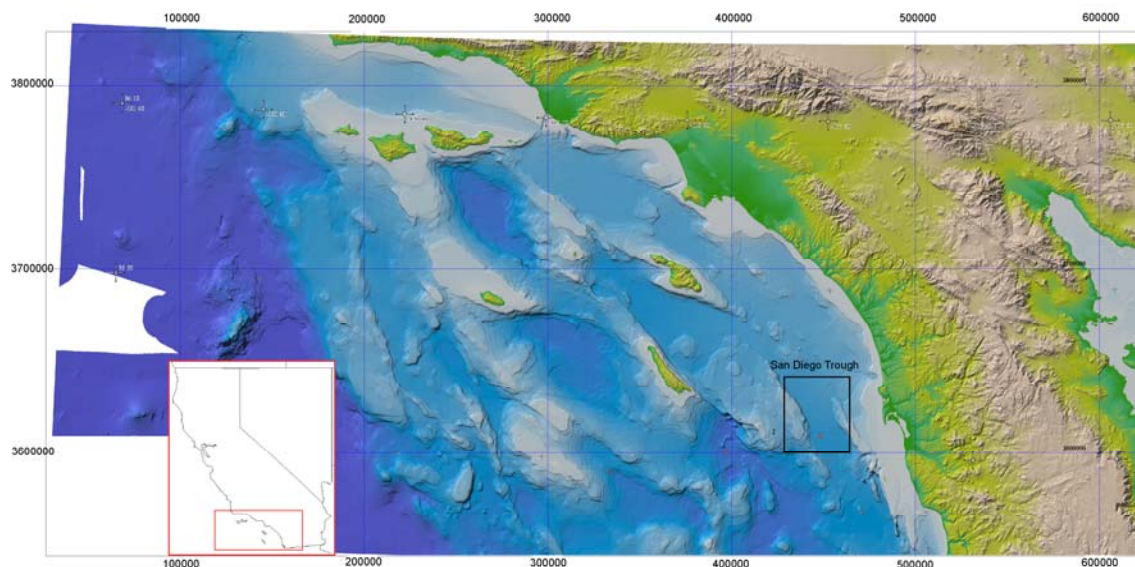


Figure 1. Regional elevation map of the California continental borderland, with the San Diego Trough study area in a black rectangle. Map courtesy of Kerry Key, Scripps Institution of Oceanography; data from the National Geophysical Data Center (NGDC).

The CCB is divided into four tectonostratigraphic terranes (Howell and Vedder, 1981) which are differentiated by their physiographic character and geomorphology (Figure 2): Patton, Nicolas, Catalina and Santa Ana (going from west to east). Several authors (Moore, 1969; Legg et al., 2004; ten Brink et al., 2000) prefer to divide the CCB into two zones, the inner continental borderland (ICB) and the outer continental borderland (OCB), each of the two parts consisting of an eastern zone floored by thick Mesozoic to Paleogene sedimentary sequences and a western zone floor by coeval mélangé deposits (Teng and Gorsline, 1991).

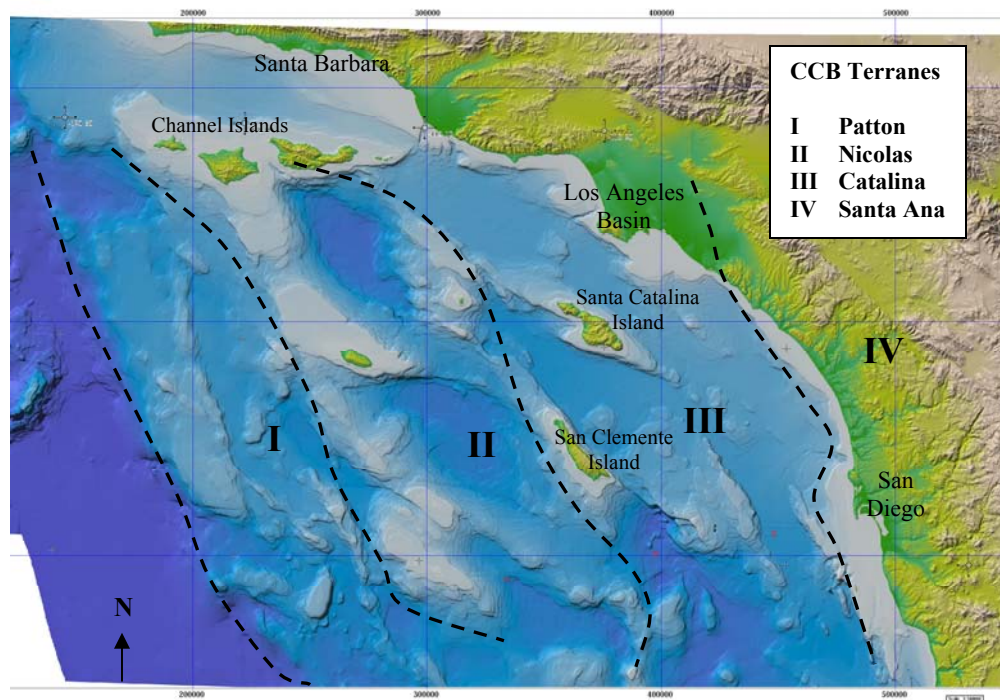


Figure 2. Regional tectonostratigraphic terranes of the California continental borderland (after Howell and Vedder, 1981 and Legg et al., 2004).

The CCB region is characterized by northwest-trending, dextral strike-slip faults with oblique components at bends and step-overs that create pull-apart basins and pressure ridges. The sub parallel ridge and trough physiographic character of the borderland is distinct from

both the adjacent Pacific Ocean basin to the west and the Peninsular Ranges to the east (Legg and Kennedy, 1991). Superimposed on the terranes are Neogene and Quaternary structures which dominate the modern geomorphic configuration of the borderland (Teng and Gorsline, 1991). The Basin and Range type bathymetric character is the result of extensive faulting and rifting as the continental borderland evolved from a subduction zone convergent margin to the present day oblique transform margin (Luyendyk et al., 1980; Luyendyk, 1991).

Lithologic Units

Because the CCB is underwater and offshore research is expensive, detailed information about the lithology is limited. The dominant basement unit, at least in the ICB region, is the Catalina Schist, which is characterized by relatively high-temperature and high pressure / high temperature metamorphism. The Catalina Schist outcrops in only a few subaerial places throughout the CCB, the type area being on Santa Catalina Island which is composed of blueschist, greenschist, amphibolite and sausserite gabbro intruded by Miocene igneous rocks (Platt, 1975; Sorensen et al., 1991; Legg and Kamerling, 2003). The protoliths of the Catalina Schist are sedimentary, mafic and ultramafic rocks that have undergone recrystallization in blueschist through amphibolitic facies conditions, postulated to have done so during early Cretaceous subduction (Platt, 1975; Grove and Bebout, 1995). The emplacement of the schist is thought to be the result of extreme crustal extension and exhumation in the form of a metamorphic core complex (ten Brink et al., 2000; Crouch and Suppe, 1993), although competing models also exist (Vedder, 1987; Mann and Gordon, 1996).

Miocene volcanic sequences overlie the Catalina Schist throughout the entire CCB region, including the SDT basin. These sequences consist of interlayered volcanics,

volcaniclastics and diatomaceous shales from mid-late Miocene. Overlying the Miocene sequences are hemipelagic layers of mostly flat-lying basin fill sediments of Pliocene age and younger (Vedder, 1987).

Tectonic History

During the Mesozoic and Paleogene time, the Farallon oceanic plate was subducted under the North American plate, forming a continental margin arc-trench system (Crouch and Suppe, 1993). The lithotectonic belts that were created in this system include the Franciscan accretionary wedge, the Great Valley forearc-basin sequence and the Coast Range ophiolites, as well as accreted arcs and mélanges and the magmatic arc of the Sierra Nevada – Peninsular Ranges (Crouch and Suppe, 1993). The subduction regime was disrupted around 28 Ma when the East Pacific Rise encountered the North American plate in the region of the present day CCB (Atwater and Stock, 1998). The Monterey microplate fragment of the Farallon Plate stopped subducting around 20-18 Ma (ten Brink et al., 2000; Nicholson et al., 1994) and the subduction regime evolved into a strike-slip regime with the formation of the San Andreas Fault system.

The regime change involved the rifting and $\sim 105^\circ$ clockwise rotation of the western Transverse Range province during early Miocene time, which resulted in the oblique extension of the continental margin (Luyendyk et al., 1980). The autochthonous Catalina Schist basement that underlaid the area was then uplifted and exposed at the surface during middle Miocene time (Legg et al., 2004; Crouch and Suppe, 1993; ten Brink et al., 2000). Regional extension-related volcanism with calc-alkaline chemistry (Wiegand, 1994) subsequently covered the exposed surfaces with volcanic and volcaniclastic rocks (Legg and Kennedy, 1991; Crouch and Suppe, 1993; Bohannon and Geist, 1998), juxtaposing

distinctive lithologic units against each other. The oblique extension included block faulting and tilting in order to create the present day horst and graben geomorphology of the ICB. There may have also been significant strain partitioning between the strike-slip faults and the normal faults as the tectonic setting evolved into different regimes (Legg and Kamerling, 2003). Figure 3 illustrates a postulated model for the present day tectonic regime offshore southern California.

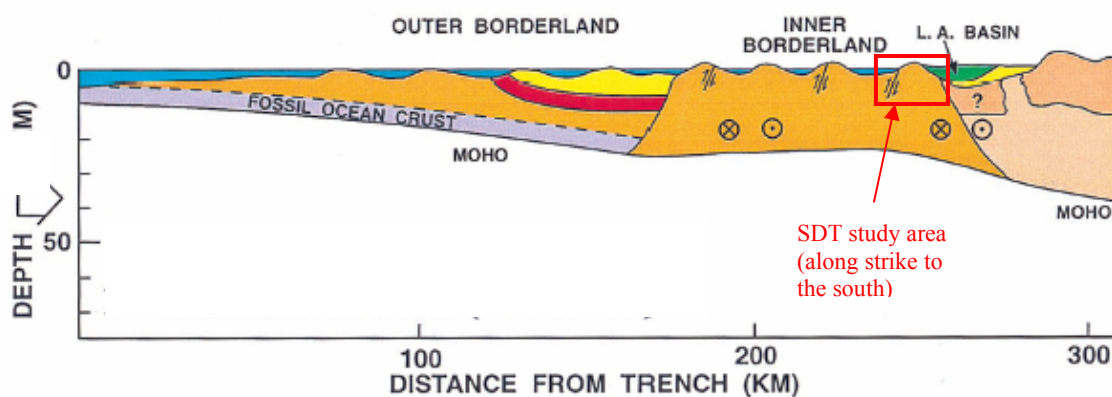


Figure 3. Schematic cross section of the southern California margin (modified from Plate 4 in ten Brink et al., 2000, p. 5852). The along-strike location of the SDT magnetotelluric study is shown in red box outline.

At present, there is evidence to suggest that the ICB is now in a compressional regime (Rivero et al., 2000; ten Brink et al., 2000). Pliocene sediments have been mapped as folded in a contractional way, though the overlying Quaternary sediments are nearly flat-lying. The 1986 Oceanside earthquake (M_w 5.3) had a dominant component of thrust (reverse) movement, although most of the aftershocks were strike-slip (Hauksson and Jones, 1988; Pacheco and Nabelek, 1988).

SAN DIEGO TROUGH

The seafloor to the west of the southern California coastline is characterized by trans-tensional and trans-pressure basins and ridges. The San Diego Trough (SDT) is an 1100+

m deep elongate sedimentary basin that is bound by the Thirtymile Bank to the west and the Coronado Bank to the east and is approximately 30 miles from the California coastline (Figure 1). The banks on either side of the trough have steep flanks on the basin side and the floor of the basin is relatively flat (Figure 4). Although the Thirtymile Bank and the Coronado Bank are similar in geomorphology and alignment, they are believed to be underlain by different terranes since the San Diego Trough is located on the boundary between the Catalina and the Santa Ana terranes.

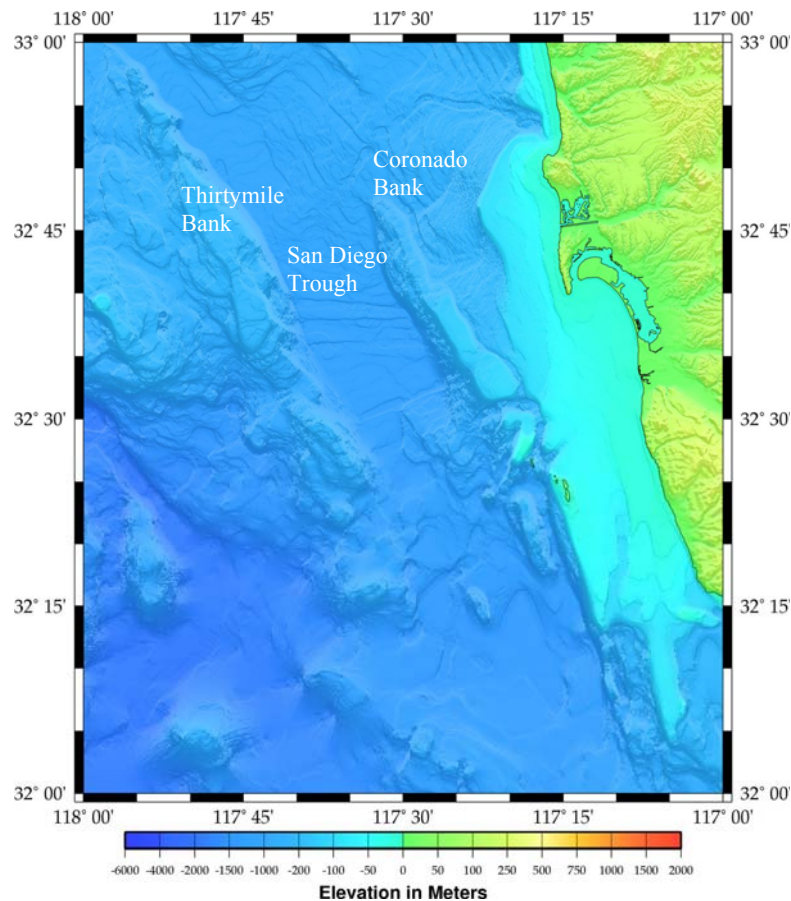


Figure 4. Bathymetric map of the offshore San Diego Trough region.

Several faults have been mapped in the San Diego Trough area. These include the Thirtymile Bank detachment fault, Coronado Bank fault zone, San Diego Trough fault, Oceanside fault and the Rose Canyon fault (e.g., Rivero et al., 2000). The SDT fault zone is

mapped as trending directly along the axis of the basin, except in the south where the fault lies along the east side of the bathymetric trough (Legg, 1985). Figure 5 illustrates the geometry of these various faults.

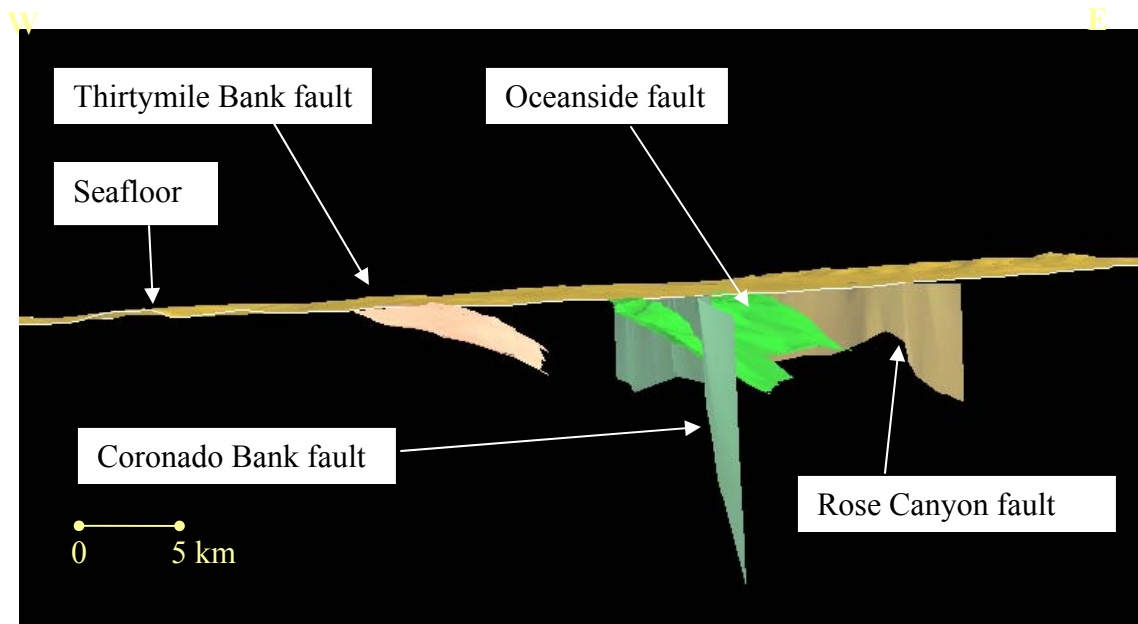


Figure 5. Fault plane geometries for the major faults in the San Diego Trough area, looking north (image is courtesy of Southern California Earthquake Center (SCEC)). No vertical exaggeration.

Thirtymile Bank

Thirtymile Bank on the west side of the San Diego Trough is a northwest trending ridge of Catalina Schist covered by Miocene volcanic and volcanoclastic rock. Bottom sample lithologies from Thirtymile Bank include glaucophane and riebeckite schist, volcanic and volcanoclastic rocks (Vedder et al., 1974) (Figure 6). The lithologic distribution of these samples supports the seismic evidence for an eastward dipping Thirtymile Bank detachment fault, visible as a strong reflector on USGS-112, and overlain by Miocene volcanic units (Figure 7, p.12). Bathymetric maps, seismic data and bottom samples indicate that the steep escarpment on the eastern flank of Thirtymile Bank results from normal faulting, landslides

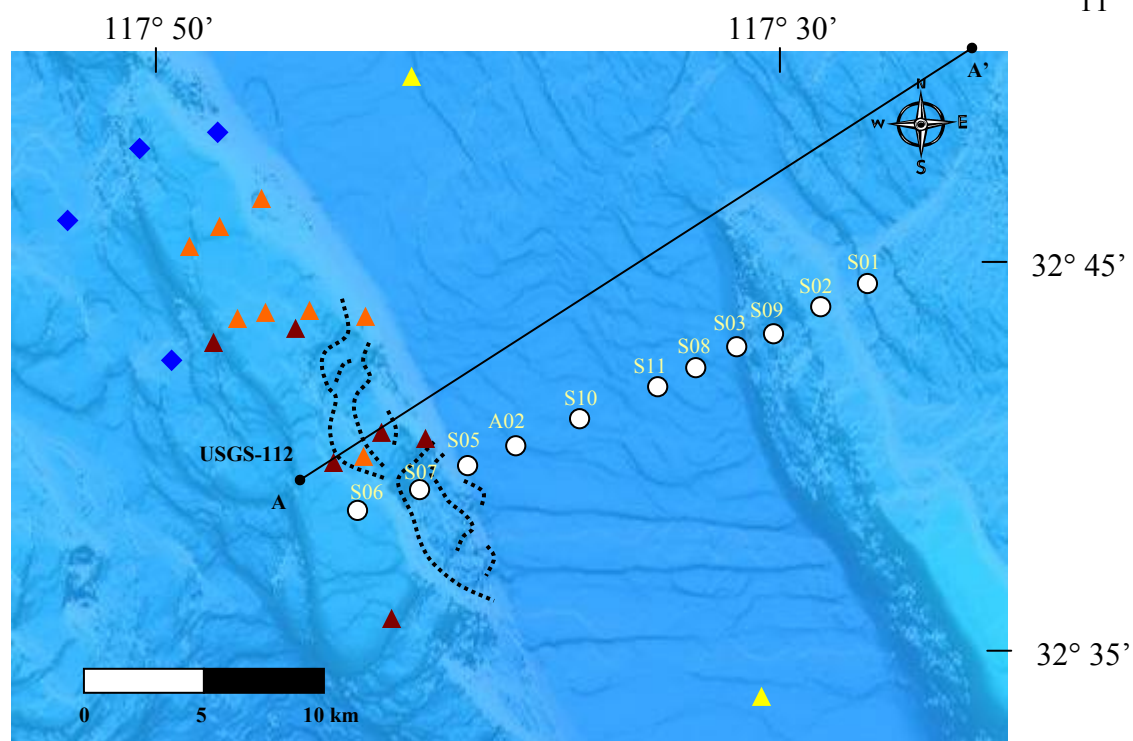


Figure 6. Bathymetric map across the San Diego Trough showing the morphology of the Thirtymile Bank landslide complex, USGS bottom samples, location of seismic line USGS-112 and seafloor MT sites (modified after Legg and Kamerling, 2003). White circles are seafloor MT sites; dotted black lines outline the landslide complex; blue diamonds are bottom samples of Catalina Schist; orange triangles are Miocene age volcaniclastic and sedimentary bottom samples; dark red triangles are volcanic bottom samples; yellow triangles are Quaternary or Pliocene age bottom samples.

and slumping (Legg and Kamerling, 2003). The Thirtymile Bank detachment fault is suggested by some (e.g., Rivero et al., 2000) to presently have compressional motion, although this belief is disputed by others (e.g., Legg and Kamerling, 2003). The orientation and position of the fault plane inferred from the 1986 Oceanside earthquake projects downdip of the Thirtymile Bank fault (Rivero et al., 2000).

Large-Scale Landslides

Comparisons of rock types, stratigraphy and structure between the submarine Thirtymile Bank and sub-aerial Santa Catalina Island indicate strong similarities. The

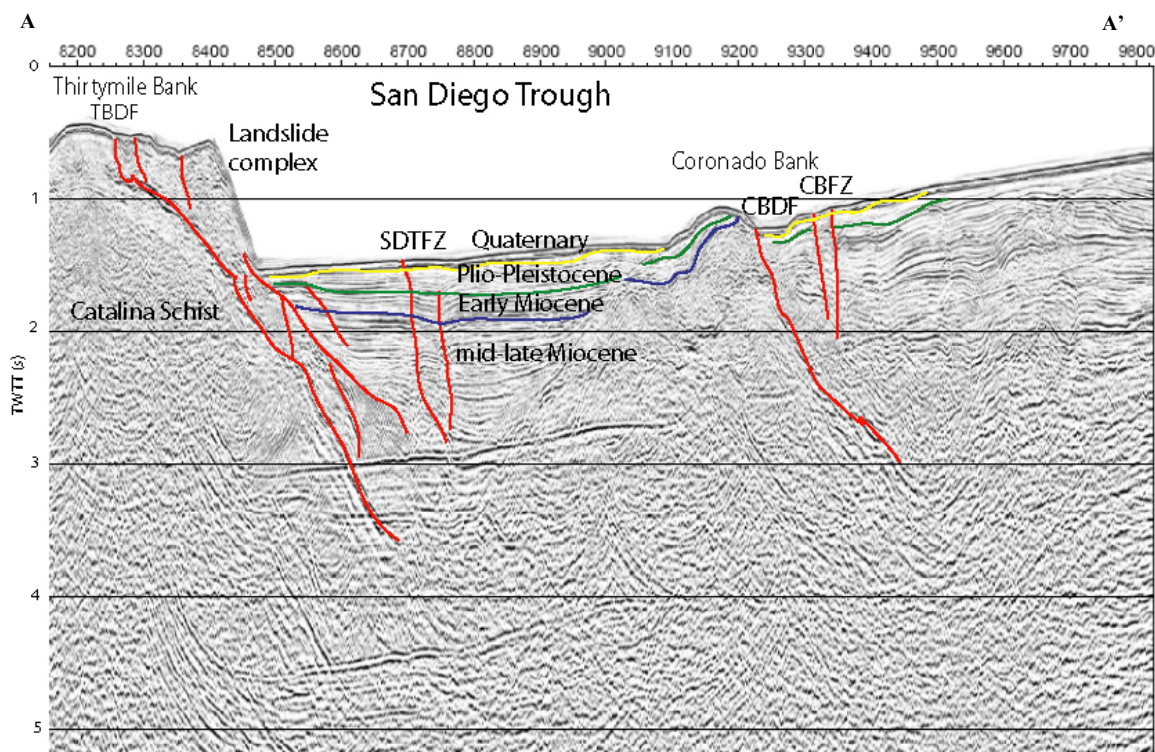


Figure 7. Seismic line USGS-112 with notable features identified. Vertical exaggeration is approximately 5 times the horizontal. Interpretation of faults and unit identification based on Legg and Kamerling (2003). Location of seismic line is shown in Figure 6.

eastern flank of Thirtymile Bank contains a postulated submarine landslide complex of Miocene volcanic rocks that would have slid down the Catalina Schist detachment surface. Similarly, the Fisherman Cove slide on Santa Catalina Island resulted from volcanic rocks overlaying sheared and fractured glaucophane schist (Cann, 1985). These similarities enable geologic relationships to be studied and insights revealed for the SDT study area based on the more easily studied Catalina Island geology.

Coronado Bank

Bottom samples from the Coronado Bank yielded sedimentary and volcanoclastic rocks (Vedder et al., 1974). The Coronado Islands in Mexico south of this bank are entirely composed of similar sedimentary sequences. Further to the east on the mainland, the

Peninsular Batholith underlies similar sediments. There is sparse evidence of Catalina Schist east of the Coronado Bank area, although there is schist in the San Onofre Breccia as well as an outcrop of Catalina Schist on the Palos Verdes Peninsula.

Several researchers have mapped a detachment fault as trending along the west side of the Coronado Bank (Nicholson et al., 1993, Sorlien et al., 1993). There is also evidence that the east side of the Coronado Bank is a major fault zone (Legg and Kennedy, 1991; Kennedy et al., 1980). The Coronado Bank detachment fault is suggested to be the southern extension of the Oceanside detachment fault, which has evidence for motional strain in the form of a reactivated blind thrust (Rivero et al., 2000).

Previous Work

The San Diego Trough has been studied using seismic refraction and reflection techniques (Shor et al., 1976; Vedder et al., 1974; Kennedy et al., 1980; Teng and Gorsline, 1991; Legg et al., 1992; Bohannon and Geist, 1998; ten Brink et al., 2000), both towed and shipboard gravity measurements (Ridgway, 1997; Ridgway and Zumberge, 2002), and heat flow measurements (Lee and Henyey, 1975). A large scale study conducted just north of this area, the LARSE (Los Angeles Region Seismic Experiment) project from 1994 included seismic, gravity and heat flow studies over the ICB. There has also been a significant amount of proprietary geoscience work done in the ICB, especially seismic reflection work. The findings from the proprietary studies are not included in this investigation, although some references cited (e.g., Ridgway and Zumberge, 2002) include results drawn from these proprietary data.

The basic structure of the SDT is postulated to be a tilted half-graben with the Thirtymile Bank detachment fault on the west side of the basin dipping east and then a

westward-tilted block, the Coronado Bank, of volcanic and sedimentary units on the east side of the basin. The two structures are separated by the strike-slip SDT Fault, which trends approximately through the middle of the basin. It is presently unknown what structure is at depth below the basin fill.

There are several competing estimates for the depth of the sediments in the middle of the basin – towed gravity results estimate the depth to be 3.4 km (Ridgway and Zumberge, 2002), while the seismic refraction work (Shor et al., 1976) shows the sediment thickness to be 3.0 km and seismic reflection data from lines USGS-112 and USGS-114 show the sediment thickness to be 3622 m below the seafloor. The character and composition of the basin fill may provide insights to tectonic phenomena as well. For example, evidence of block faulting and tilting within basin sediments, along with local sedimentation rates and stratigraphic correlations, can constrain the timing of the earthquake activity in the CCB region.

Because the San Diego Trough is situated at or near the border of the Catalina and Santa Ana terranes, which is marked by the presence of Catalina Schist, it may be possible to identify and understand the transition from one terrane to another using geophysical measurements. The differing electrical properties of schist, volcanics, and sediments make it possible that magnetotelluric investigations could help resolve the deeper geologic structure of the region beneath the San Diego Trough.

CHAPTER 3

THEORY AND METHODOLOGY

The following section is derived from Chapter 2 of Key (2003).

SEAFLOOR RESISTIVITY

Physical Properties

The physical properties of rocks vary greatly depending on composition and tectonic setting. The properties that are typically measured are acoustic velocity (using the seismic technique), density (using gravity measurements and gamma-gamma logs), susceptibility (via magnetic surveys), and resistivity (using electrical and electromagnetic methods). Of these four properties, it is common for resistivity measurements to vary by several orders of magnitude, far more than other properties typically measured. This is one of the reasons why measuring resistivity is appealing, since contrasts in resistivity should clearly stand out.

In favorable geological settings, one should be able to determine the subsurface geoelectric structure and correlate them with the local structure. Such settings include plate tectonic boundaries such as oceanic spreading centers, where highly resistive volcanic material lies near highly conductive magma and fluids; active faults, where fluids are distributed along the strike of the fault (e.g., Bedrosian et al., 2004); and heavily mineralized zones where the alteration to the host geologic structures creates a conductive anomaly against unaltered rock.

Porosity Effects

In the uppermost seafloor, one of the primary controls on electrical resistivity is the amount of seawater present and the nature of its distribution. Because intrusive igneous rocks tend to have low porosities (small amounts of interconnected pore fluid) they tend to have the highest resistivity (~1,000 to 10,000 Ωm). In contrast, unconsolidated sediments, which can have connected porosities in excess of 60% at the seafloor, have low resistivities (~ 2-3 Ωm). As sedimentary rocks consolidate, porosity decreases, the pore fluid becomes less connected, and resistivity increases. The relationship between bulk resistivity measured by EM techniques and the porosity of the seafloor is often characterized by Archie's law (Archie, 1942) for clay-free rocks,

$$\rho_m = \rho_f \theta^{-m} \quad (1)$$

where ρ_m is the measured resistivity (Ωm), ρ_f is the pore fluid resistivity (Ωm), usually assumed to be that of seawater (at least in the uppermost seafloor), θ is the fractional porosity, and m is the sediment cementation coefficient that typically varies between 1.4 and 1.8 for marine sediments (Jackson et al., 1978), and is slightly higher (2-3) for volcanic rocks. Low values of m are used when the pore-fluid is well-connected, and when $m = 1.2$, it is nearly at the Hashin-Shtrikman bounds (Hashin and Shtrikman, 1962), which are formally the tightest bounds that can be placed on an isotropic two phase material and a variety of other relationships for specific geometries of pore fluid (e.g., Schmeling, 1986; Heinson and Constable, 1992). The low end ($m = 1.2$) corresponds to an ideal case of material spheres completely covered in a pore fluid, whereas the opposite end (high m values of the Hashin-

Shtrikman bounds) corresponds to a case where there are isolated fluid packets that do not interact.

Archie's Law assumes that the rock itself does not contribute to the overall conduction because the rock matrix is usually several orders of magnitude more resistive than seawater. If there is clay present in the subsurface, this can alter the measured resistivity because of the double-layer, surface conduction process (Ward, 1990). There are other relationships for a two-phase material that account for the rock conductivity (the reciprocal of resistivity), usually deeper in the crust or mantle in the presence of partial melt. The controlling parameters of resistivity in the marine environment (which is a region of high fluid concentrations) have been shown to be primarily influenced by the resistivity of the fluid itself, whereas in other environments which may have low fluid concentrations ($< 1 \text{ S/m}$), the surface conductance due to mobile ions in local clay becomes more important (Wildenschild et al., 2000). Because of the dependency of resistivity on pore fluid content, which in turn is related to rock type, investigating the variations in electrical conductivity through the subsurface can provide useful insight into the regional lithology and potentially the presence of faulted or fractured regions of seafloor.

The temperature of the substructure also has a significant influence on the conductivity and therefore porosity, especially in the marine environment. Higher temperatures increase the mobility of the dissolved ions in solution, therefore, causing lower resistivity. The geothermal gradient, which can vary regionally depending on the tectonic conditions, can counteract the effects of cementation with depth.

THE MAGNETOTELLURIC METHOD

The magnetotelluric (MT) method is the measurement of the Earth's naturally occurring, time-varying EM fields. The electromagnetic fields are generated by two sources. First is the interaction of the Earth's magnetic field with the solar wind (charged particles emitted from the sun) that results in fluctuations in the magnetosphere. The fields resulting from this interaction typically contain frequencies below 1 Hz. Second is the electromagnetic energy that comes from lightning activity which typically results in frequencies above 1 Hz. The naturally-occurring electromagnetic spectrum for the full range of relevant frequencies is illustrated in Figure 8.

The lower frequencies that are generated by the interaction of Earth's magnetosphere and solar wind are related to the level of sunspot activity. It is the breakdown of sunspots which release plasma that travel outwards from the sun, some of which interact with Earth's magnetic field. The movements of these charged particles in Earth's magnetosphere occur on such an immense scale that the net effect of this energy, when coupled through the ionosphere, is to act like a plane wave of EM energy at the Earth's surface.

EM energy from lightning becomes trapped between the Earth's surface and the ionosphere, resonating around the planet and resulting in the enhancement of certain frequencies which are a function of the Earth's waveguide geometry. One of the key resonant frequencies is called the Schumann resonance, at about 7.8 Hz, where the wavelength is equal to Earth's circumference.

Scientists in the 1950s realized that measuring the time-varying electric and magnetic fields at a given location could result in repeatable calculations of the Earth's geoelectric properties at that location (Tikhonov, 1950; Cagniard, 1953). The naturally occurring

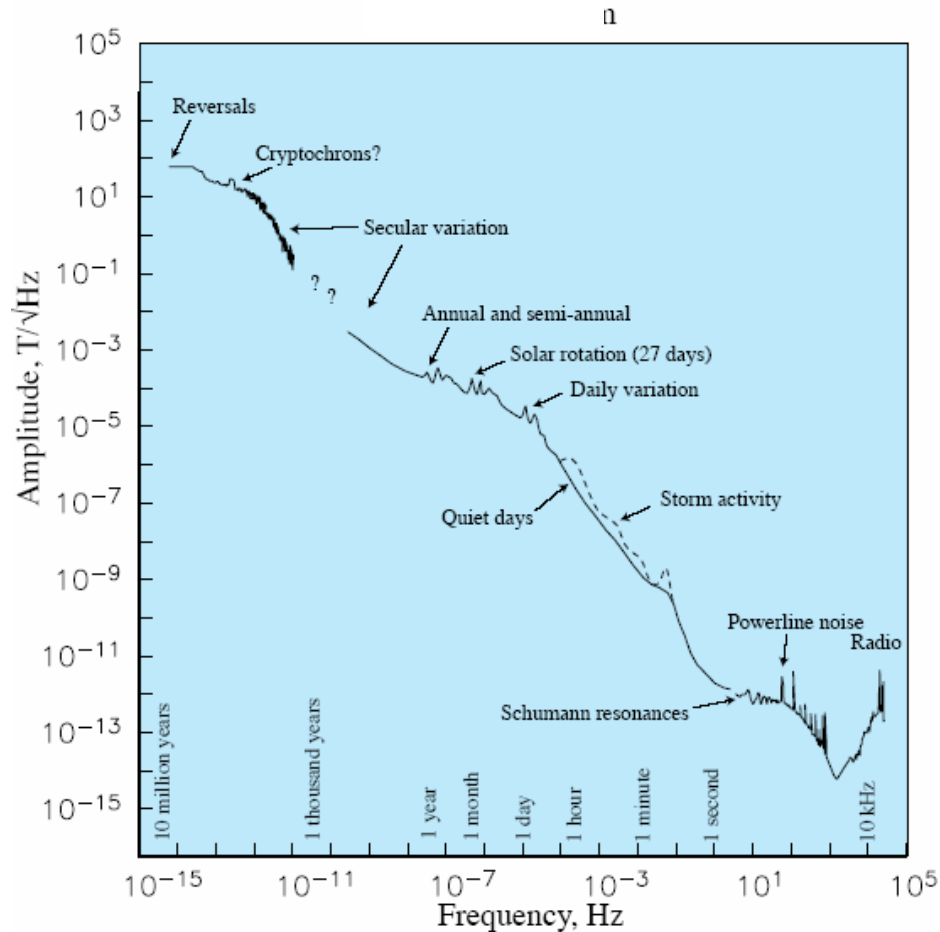


Figure 8. The naturally-occurring electromagnetic energy spectrum.
Source: Constable, S., and Constable, C. 2004, *Satellite Magnetic Field Measurements: Applications in Studying the Deep Earth*, in Sparks, R.S.J., and Hawkesworth, C.T., Eds., *State of the Planet: Frontiers and Challenges in Geophysics*: Am. Geophys. Union, Geophys. Mono. 150, p. 149.

magnetic fields generate secondary electric and magnetic fields within electrically conductive material in the Earth, and the depth at which currents are induced is dependent on the frequency of the field. Thus, by measuring a broad spectrum of electric and magnetic fields it is possible to infer Earth's conductivity as a function of depth.

Exploiting the MT energy requires simultaneous measurement of orthogonal components of both the electric field and the magnetic field, referred to as E_x , E_y , H_x and H_y . An MT measurement relies on constructing the frequency dependent ratio of an electric field

component to its orthogonal magnetic field component. The ratio of the two, assuming plane wave source geometry, obviates the need to understand details of the source. The horizontal electric and magnetic field components are related to each other by the 2-x-2 complex magnetotelluric impedance tensor (Eq. 15) which contains information about the subsurface conductivity.

Magnetotelluric Theory

Two of Maxwell's equations (Faraday's Law and Ampere's Law) form the basis for the MT method:

$$\nabla \times \mathbf{E} = -\frac{\partial \mathbf{B}}{\partial t} \quad (2)$$

$$\nabla \times \mathbf{H} = \mathbf{J} + \frac{\partial \mathbf{D}}{\partial t} \quad (3)$$

where

- \mathbf{E} = electric field intensity (V/m, volts/meter)
- \mathbf{J} = electric current density (A/m², amperes/meter squared)
- \mathbf{H} = magnetic field intensity (A/m, amperes/meter)
- \mathbf{B} = magnetic flux density (T, tesla)
- \mathbf{D} = electric displacement (C/m², coulombs/meter squared)

The fundamental relationships that relate these quantities together are as follows:

$$\begin{aligned} \mathbf{B} &= \mu \mathbf{H} \\ \mathbf{D} &= \varepsilon \mathbf{E} \\ \mathbf{J} &= \sigma \mathbf{E} \\ \sigma &= 1/\rho \end{aligned}$$

where

- ε = dielectric permittivity (F/m, farads/meter)
- μ = magnetic permeability (H/m, henrys/meter)
- σ = electric conductivity (S/m, siemens/meter)
- ρ = resistivity (Ωm , Ωmeter)

When the above relations are substituted into Maxwell's equations, the electromagnetic properties of matter – dielectric permittivity, magnetic permeability and electric conductivity (sometimes expressed as its reciprocal, the resistivity) – can be described. By taking the curl of the first Maxwell's equation and substituting for \mathbf{B} , the relation becomes

$$\nabla \times (\nabla \times \mathbf{E}) = -\mu \left(\nabla \times \frac{\partial \mathbf{H}}{\partial t} \right) \quad (4)$$

The above equation can then be manipulated using fundamental relationships and vector identities to become wave equation

$$\nabla^2 \mathbf{E} = \mu \left(\sigma \frac{\partial \mathbf{E}}{\partial t} + \varepsilon \frac{\partial^2 \mathbf{E}}{\partial t^2} \right) \quad (5)$$

The Fourier transformation of the above equation from time to frequency domain yields the general form of the Helmholtz equation

$$\left(\nabla^2 + \kappa^2 \right) \mathbf{E}(x, y, z, \omega) = 0 \quad (6)$$

where ω is the angular frequency $2\pi f$ and κ is the complex wave number or propagation constant, which is a function of the properties of the medium, given by

$$\kappa = \omega \left[\left(\varepsilon - i \frac{\sigma}{\omega} \right) \mu \right]^{1/2} . \quad (7)$$

Quasi-Static Approximation

One condition which is assumed to hold true for MT methodology is the quasi-static approximation. It says that conductive currents in the earth are significantly greater than

displacement currents. Displacement currents are defined using variations in the electric field over time; conduction currents are defined by the flow of ions or electrons that create ohmic heat or loss. Written another way, the quasi-static approximation is stated as:

$$\sigma \gg \omega\epsilon.$$

This is based on the premise that MT relies on relatively low frequencies in order to evaluate the Earth's conductivity distribution. The implication is that the dielectric permittivity can be neglected, thus placing ultimate EM reliance on the conductivity of the material. Assuming the quasi-static approximation, the wave number, κ , can be rewritten as:

$$\kappa \cong (-i\sigma\mu\omega)^{\frac{1}{2}} = \left(\frac{\sigma\mu\omega}{2}\right)^{\frac{1}{2}} - i\left(\frac{\sigma\mu\omega}{2}\right)^{\frac{1}{2}} = (\sigma\mu\omega)^{\frac{1}{2}} e^{-i\frac{\pi}{4}}. \quad (8)$$

As long as the quasi-static approximation holds true, the wave equations for MT can be rewritten as

$$\nabla^2 \mathbf{E} = \mu\sigma \frac{\partial \mathbf{E}}{\partial t} \quad (9)$$

$$\nabla^2 \mathbf{H} = \mu\sigma \frac{\partial \mathbf{H}}{\partial t} \quad (10)$$

The removal of the second derivatives takes the MT application out of the wave equation regime and into the diffusion regime. If electromagnetic energy propagates in the manner stated above and the magnitude of the various currents hold true, one can solve the Helmholtz equation (given above in Eq. 6) as an ordinary differential equation yielding

$$\mathbf{E}_x(z) = E_0 e^{\pm i\kappa z} \quad \text{and} \quad \mathbf{H}_y(z) = H_0 e^{\pm i\kappa z}$$

where E_0 and H_0 are the values of the field at $z = 0$. This means that the depth of penetration for the MT signal is tied to the frequency of that signal and conductivity of the materials it is penetrating. The skin depth formula,

$$z = \delta = \left(\frac{2}{\sigma \omega \mu} \right)^{\frac{1}{2}} \text{ or } \delta \cong 0.5 \sqrt{\rho T} \text{ (km)}, \quad (11)$$

(where $T = 1 / f$) defines the depth in the earth at which the incident amplitudes E_0 and H_0 reduce exponentially to $1/e$ (~37%) of their surface strength (Figure 9). Although most of the magnetotelluric energy is reflected from the surface, a significant amount transmits through the earth.

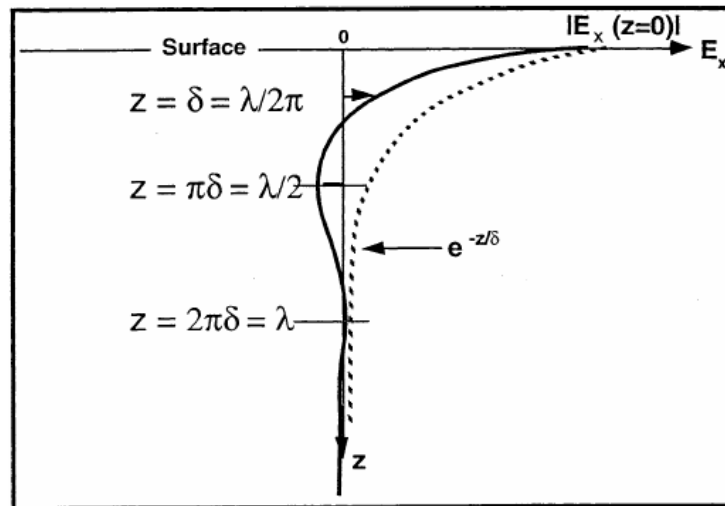


Figure 9. Attenuation of the electric field amplitude at various depths (z). The solid line follows the penetration of a single wavelength; the dotted line shows the exponential decay of z/δ . At one skin depth, $z = \delta$, the incident energy amplitude reduces exponentially to 37%. Source: Jiracek, G.R., Haak, V., and Olsen, K.H., 1995, *Practical Magnetotellurics in Continental Rift Environments*, in Olsen, K.H., Ed., *Continental Rifts: Evolution, Structure and Tectonics*: Elsevier, p. 108).

Plane-Wave Assumption

Standard approaches to modeling and interpreting magnetotelluric data rely on certain key assumptions remaining valid. One of these assumptions is that the source field for the electromagnetic energy is a plane wave that propagates perpendicular to the surface. Because the MT signal originates at a substantial distance in the ionosphere and magnetosphere, the source field is assumed to be a plane wave. Similarly, the large contrast in resistivity between the earth's atmosphere (air is very resistive) and the earth's surface (the Earth is very conductive) requires that the electromagnetic waves propagate vertically below the Earth's surface independent of their origin in the ionosphere. Lower resistivity materials attenuate EM fields more sharply and have smaller skin depths than high resistivity materials. Similarly, high frequency electric and magnetic fields have smaller skin depths compared to low frequency fields.

1-D Case

As stated previously, the ratio of the electric field to the magnetic field determines the surface impedance \mathbf{Z} . Taking $E(\omega) = E_x$ and $H(\omega) = H_y$ of a homogeneous half-space, the relation for the surface impedance Z_s is

$$Z_s = \frac{E_x}{H_y} = \frac{\omega\mu}{\kappa} = \left| \frac{E_x}{H_y} \right| e^{i\phi_z}$$

where ϕ_z is the phase value of the impedance. By incorporating Equation 8 for the propagation constant, κ , the above relation can be rewritten as

$$Z_s = (\omega\mu_0\rho)^{\frac{1}{2}} e^{i\frac{\pi}{4}}$$

or rearranged to be

$$\rho_a = \frac{1}{\omega\mu_0} |Z_s|^2. \quad (12)$$

Here, the magnetic permeability of free space, μ_0 , is assumed for all Earth materials. The apparent resistivity, ρ_a , contains the superimposed effects of reflection and attenuation from each layer in a multiple layer conductivity structure. This is because it is dependent on the surface impedance, Z_s . When the conductivity structure is layered in the z direction, both downward and upward traveling, diffusing energy must be taken into account. The effects of upward and downward traveling electromagnetic fields within each layer add up to become the electrical impedance at the surface (Z_s) of a one-dimensional (1-D) model. The impedance Z_i at the top of the i^{th} layer in a layered 1-D model with N layers can be calculated with the recursive equation

$$\hat{Z}_i = Z_i \frac{\hat{Z}_{i+1} + Z_i \tanh(i\kappa_i h_i)}{Z_i + \hat{Z}_{i+1} \tanh(i\kappa_i h_i)} \quad (13)$$

where h_i is the layer thickness and Z_i is the impedance of layer i (Ward and Hohmann, 1988). The recursion starts at the top of layer N which is bound below by an infinite half-space, Z_{N+1} . The recursive calculation propagates to the layer above and so on up to the surface, such that the actual surface impedance at the top of any layer is independent of the impedance of the layers above it. This recursive impedance relationship explains why a 1-D model for the subsurface in a marine environment will have a surface impedance that does not depend on the ocean layer.

TE and TM Modes

For a 2-D Earth, the apparent resistivity is dependent on the source field polarization and the measurement directions of the electric and magnetic fields. Using the tensor formulation for the electrical impedance,

$$\mathbf{E} = \mathbf{ZH} \quad (14)$$

one can expand the tensors to include the actual measurements that are recorded, i.e.,

$$\begin{pmatrix} E_x \\ E_y \end{pmatrix} = \begin{pmatrix} Z_{xx} & Z_{xy} \\ Z_{yx} & Z_{yy} \end{pmatrix} = \begin{pmatrix} H_x \\ H_y \end{pmatrix}. \quad (15)$$

The impedance tensor \mathbf{Z} can be calculated if two or more source polarizations are present, where the first subscript refers to the electric field direction and the second to the magnetic field direction. In a 1-D conductivity structure,

$$Z_{xx} = Z_{yy} = 0 \text{ and } Z_{yx} = -Z_{xy}.$$

In a 2-D conductivity structure, which is the case when either the x or y axis is aligned with the regional strike, then

$$Z_{xx} = Z_{yy} = 0 \text{ and } Z_{yx} \neq -Z_{xy}.$$

The impedance elements Z_{yx} and Z_{xy} are associated with the TE and TM modes, respectively.

The relation for apparent resistivity is given above in Equation 12 and rewritten here for a 2-D case,

$$\rho_{xy} = \frac{1}{\omega\mu} |Z_{xy}|^2 \quad (16)$$

with the impedance phase defined as

$$\Phi_{xy} = \arctan \left(\frac{\text{Im}(Z_{xy})}{\text{Re}(Z_{xy})} \right) \quad (17)$$

Similar equations also exist for ρ_{yx} and ϕ_{yx} . The off-diagonal impedances in the 2-D case form two independent modes -- transverse electric (TE) and transverse magnetic (TM). The TE mode uses the electric field that is parallel to the regional strike whereas the TM mode uses the electric field that is perpendicular to regional strike. These two modes can also be described by primarily inductive effects (TE) and galvanic effects (TM).

In a 1-D case, the conductivity gradient is only in the vertical direction and so, as shown by Pellerin and Hohmann (1990), there is no opportunity for electrical charges to build up. However, in the 2-D case, the addition of the horizontal variation in resistivity allows a component of the electrical field that will be in the same direction as the conductivity gradient. This is a galvanic effect, and is defined by the total electric field producing electric charges where variations in conductivity occur (Jiracek, 1990). This is most common at boundaries – both discrete and continuous. The excess charges create secondary electric fields which add or subtract vectorially to the primary electric field. The inductive effect follows Faraday’s law, where the time derivative of the primary magnetic field induces voltages and, hence, currents. These currents then produce secondary magnetic fields which may be aligned with the primary magnetic field, changing the overall signature of the measured field.

SEAFLOOR MT

Measuring the resistivity of the subsurface in the ocean environment requires a unique set of considerations. First of all, the MT signal becomes attenuated as it travels through the conductive seawater column so that the high frequency components of the signal get filtered out by the time the signal gets to the seafloor receiver. The overlying sea water has a resistivity value of approximately $0.3 \Omega\text{m}$ and so has a skin depth of ~ 270 m at a period of 1 s. Therefore, the highest frequency that is measured in seafloor MT is related to the ocean depth at the seafloor MT site.

Figure 10 illustrates the attenuation of the electric and magnetic fields over a range of scenarios where the water depth and seafloor resistivity vary as a function of period (Constable et al., 1998; Key, 2003). It is clear that the magnetic field is more sensitive to the variation of seafloor resistivity than is the electric field and this sensitivity extends throughout the entire range of periods. As the seafloor resistivity increases (from solid lines to long dashed lines), so does the impedance, $Z = E/H$, which leads to an increase in the electric field but a decrease in the magnetic field.

The depth of penetration for the resistivity measurements, or MT sensitivity, depends greatly on the composition of the subsurface and the overall conductivity structure. In regions where the seafloor geology is dominantly composed of conductive material (such as sediments), the MT signal is sharply attenuated and does not penetrate to great depth. In regions where the seafloor is more resistive, the MT signal is able to travel through the resistive layers with less attenuation and is able to image to a greater depth but with proportionately lower resolution. In Figure 11 (p. 30), the case is shown for a seafloor MT site in 1000 m of seawater with 300 m of sediments underlying it – the apparent resistivity

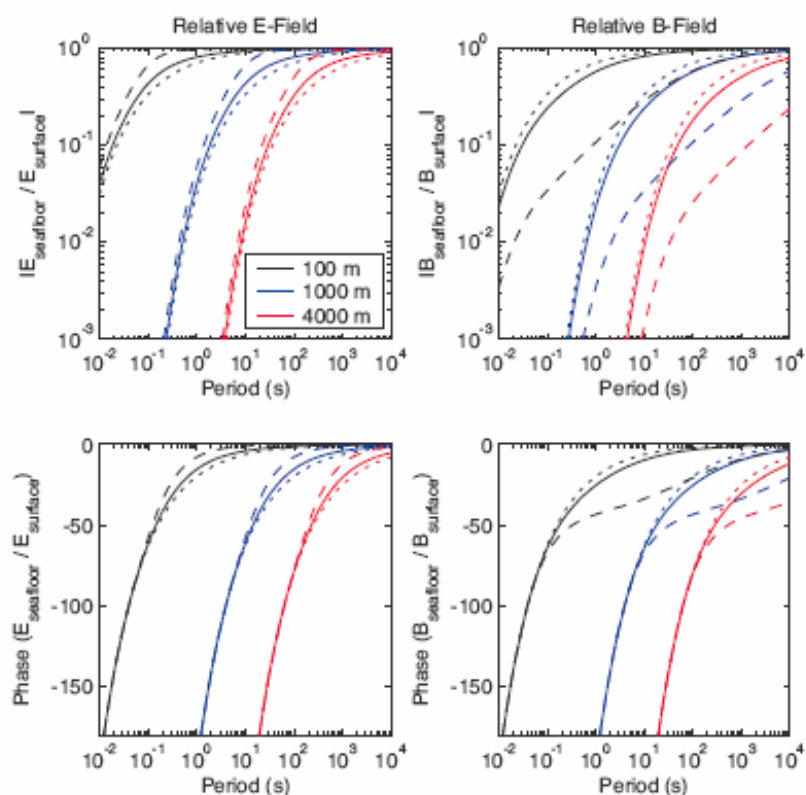


Figure 10. Attenuation of the electric and magnetic fields due to a layer of seawater. The ratio of seafloor to sea surface fields is plotted as a function of period. Seafloor resistivities are $1 \Omega\text{m}$ (solid lines), $100 \Omega\text{m}$ (long dashed lines) and half space attenuation (dotted lines) for seawater. Variation in water depths are illustrated in black (100m), blue (1000m) and red (4000m). Source: Key, K. W., 2003, Application of Broadband Marine Magnetotelluric Exploration to a 3D Salt Structure and a Fast-Spreading Ridge, Ph.D. dissertation, Univ. of Cal., San Diego, p. 15.

is predicted to have an ascending branch on a ρ_a versus period sounding curve and the phases are expected to be low, $< 35^\circ$. Similarly, in the same seafloor setting with resistive rocks rather than sediments, the apparent resistivity is expected to have a sharper ascending branch and the phase is expected to be closer to zero degrees (Figure 12, p. 31). The addition of a 300 m high topographic feature on the seafloor has the effect of causing a negative phase response in the TE mode (Figure 13, p. 32).

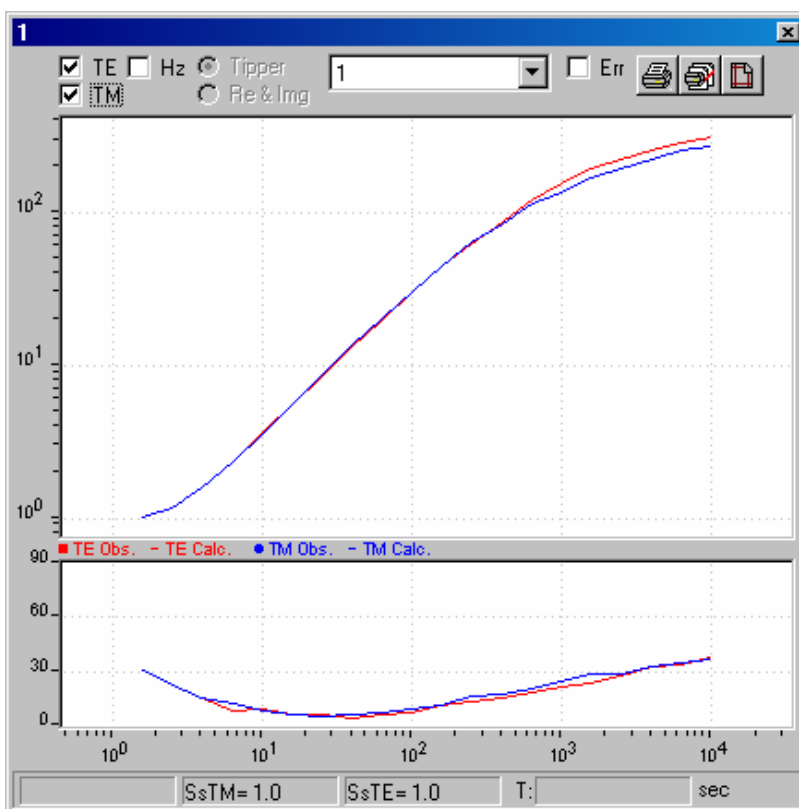


Figure 11. Forward model response of seafloor MT site in 1000 m of seawater with 300 m of sediments ($1.5 \Omega\text{m}$) underlying the site. Note that the phases are predicted to be less than 35° .

The topographic distortion in the marine environment is described in detail by Schwalenberg and Edwards (2004), but to summarize, the distortion occurs primarily in the TM mode electric fields and the TE mode magnetic fields (Figure 14, p. 32). This distortion appears in the form of decreased E and H fields, respectively, when the measurements are made at the bottom of a hill but increased E and H above a rise on the seafloor.

Subsequently, the apparent resistivities and phases also become distorted by topography but in a slightly different way (Figure 15, p. 33). TM apparent resistivities on land are smaller below a hill but they are greater above a hill in the marine environment. TE mode apparent resistivities and phases are significantly distorted in a marine environment

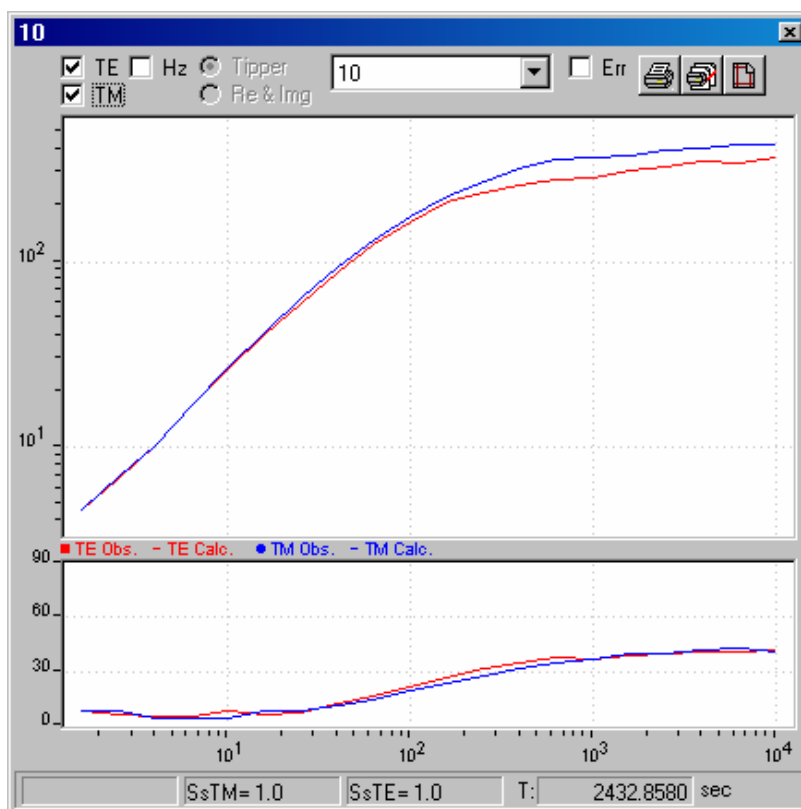


Figure 12. Forward model response of seafloor MT site in 1000 m of seawater with 300 m of resistive rocks (10 Ω m) underlying the site. Note the phase that is approximately 0 for the top 30 s.

that has topography (Schwalenberg and Edwards, 2004) whereas they experience very little distortion due to topography on land (Jiracek, 1990).

On the seafloor, both modes are affected and the apparent resistivities behave in an opposite way compared to the land response. Similarly, it has been shown that with increasing conductivity contrast and/or with decreasing period, both the TE mode apparent resistivity and phase become more distorted (Schwalenberg and Edwards, 2004). It has also been shown that if a seafloor site is at the top of a hill, it has high TM apparent resistivity and if a site is in a depression on the seafloor, it has a low TM apparent resistivity. According to Schwalenberg and Edwards, the effect of this topography would be as much as 1.4 times the

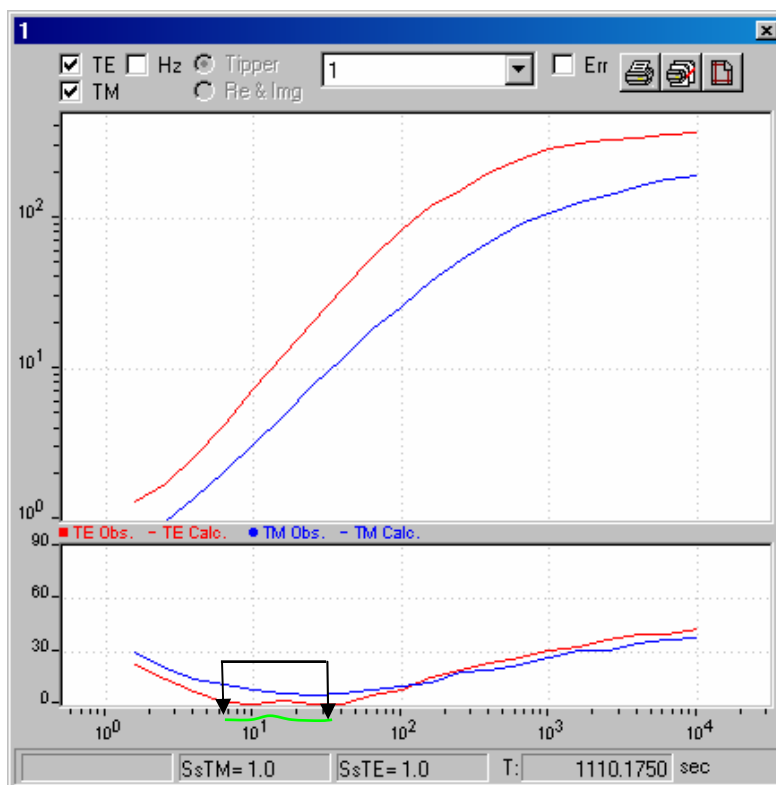


Figure 13. Forward model response of seafloor MT site in 1000 m of seawater with 300 m of sediments ($1.5 \Omega\text{m}$) underlying the site and a 300 m topographic high adjacent to the site. TE mode is the top curve in the apparent resistivity graph (in red). Note the negative phases in the TE mode (in green, also indicated in black arrows).

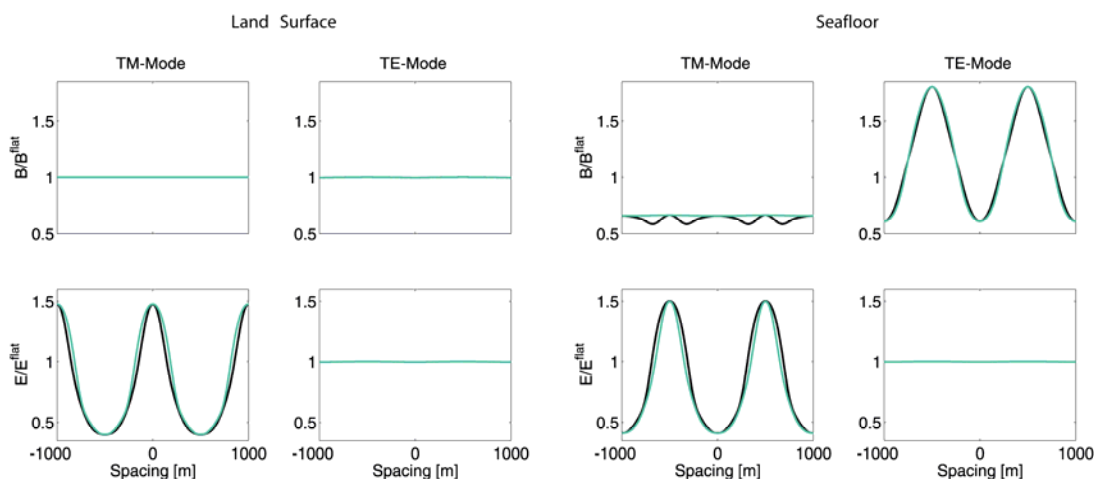


Figure 14. Electric and magnetic field distortions due to a sinusoidal topography in both the land and seafloor environment, shown for both the TE mode and the TM modes. In the marine environment, the TM mode electric fields and the TE mode magnetic fields are distorted by the topography and the TM mode magnetic field is reduced by the effect of the sea water.

Source: Schwalenberg, K., and Edwards, R.N., 2004, The Effects of Seafloor Topography on Magnetotelluric Fields: An Analytical Formulation Confirmed with Numerical Results: *Geophys. J. Int.*, 159, p. 613.

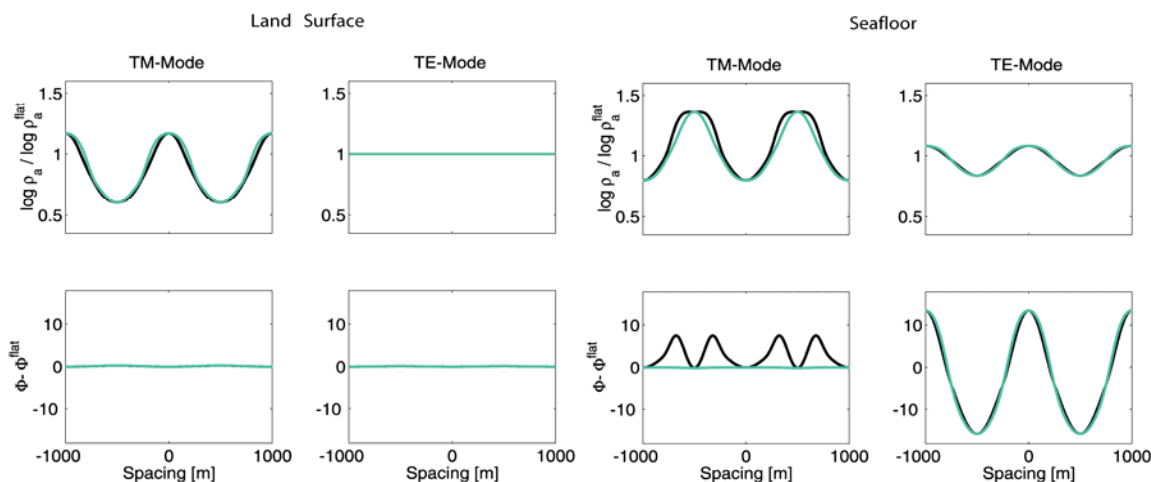


Figure 15. Apparent resistivities and phases from TM and TE modes in both the land and seafloor environments. On land, distortion primarily appears in the TM mode but on the seafloor, both TE and TM apparent resistivities and phases are affected. Source: Schwalenberg, K., and Edwards, R.N., 2004, The Effects of Seafloor Topography on Magnetotelluric Fields: An Analytical Formulation Confirmed with Numerical Results: *Geophys. J. Int.*, 159, p. 614.

original for a hill and 0.75 times the value for a depression. It has been shown that the current streamlines converge at the tops of hills and diverge in valleys (Figure 16).

SEAFLOOR MT INSTRUMENTATION

History

The evolution of the marine magnetotelluric (MMT) receiver started with Professor Charles Cox at SIO, who made deepwater MT measurements in the 1960s. The original MMT receiver was developed to investigate the mantle conductivity in the deep ocean, requiring only long period range functionality, on the order of several hundred seconds (Constable et al., 1998). These original MMT receivers were effective at period ranges of 1,000 s to 100,000 s and utilized fluxgate or torsion fiber magnetic sensors and water-chopped electric field sensors (Filloux, 1987).

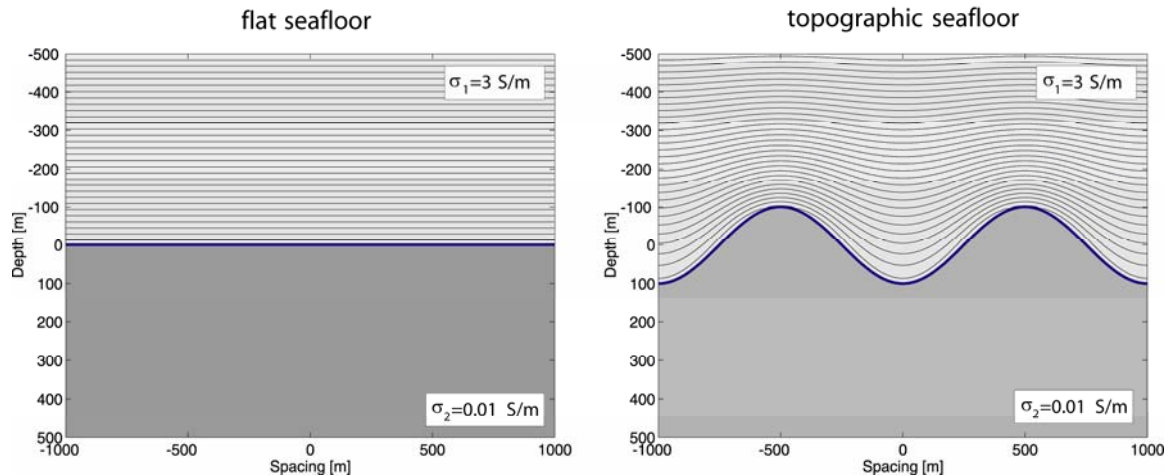


Figure 16. Electric current lines in the seafloor environment, showing the effects of a sinusoidal topographic seafloor.

Source: Schwalenberg, K., and Edwards, R.N., 2004, The Effects of Seafloor Topography on Magnetotelluric Fields: An Analytical Formulation Confirmed with Numerical Results: *Geophys. J. Int.*, 159, p. 617.

MT measurements in the marine environment had been experimentally performed in the petroleum industry since the 1960s as well, when scientists at Mobil Oil Company attempted a moored MT system in 10 m water (Hoehn and Warner, 1960). However, these early attempts used land-type instrumentation and involved bulky recording systems as was standard in that day.

Advancements in technology and successful application of MT to the petroleum industry emerged in the 1990's, proving it possible to make good MMT measurements in depths relevant to hydrocarbon exploration (Constable et al., 1998). The development of the broadband MT receiver in the 1990s was the direct result of increasing demand to image subsurface contrasts in resistivity at depths appropriate for petroleum exploration. The modern MMT instrument is an autonomous data logger that is deployed from a ship using a crane. The intrinsically buoyant design allows the seafloor receiver to float back up to the sea surface when the appropriate acoustic command signal is sent.

SIO Seafloor MT Receiver

The principal components of a modern broadband MMT instrument are (Figure 17):

- a single polyethelene frame that houses the data logger and acoustic release unit
- a glass flotation package attached to the top of the frame
- two orthogonal horizontal electric dipole sensors, which are made up of four orthogonal semi-rigid arms threaded through the frame, containing electrodes in each of the ends
- two orthogonal induction coil magnetometers, threaded through the frame
- a custom-made concrete anchor with acoustic release mechanisms

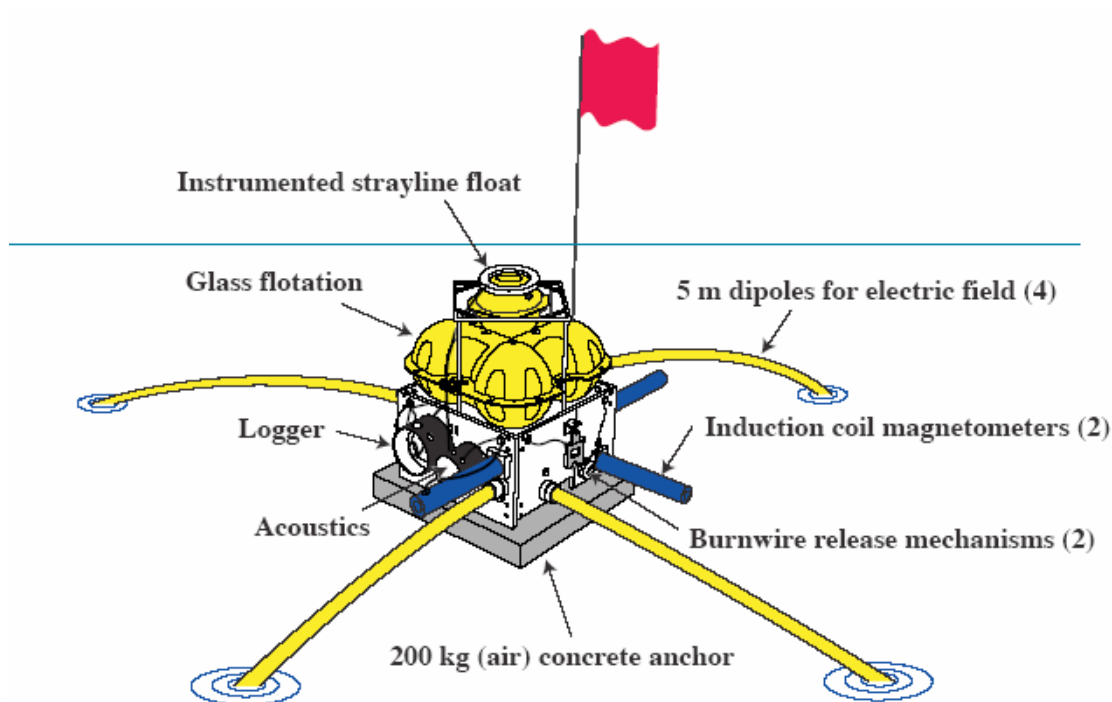


Figure 17. The modern SIO seafloor MMT receiver, with all of the major features identified. Note that drawing represents the instrument sitting on the ocean surface, about to sink to the seafloor. The blue line in the background is the ocean horizon in the distance and the rings around the ends of the electric field dipole sensors represent the places where the ends of the dipoles are already underwater (drawing courtesy of Scripps Institution of Oceanography).

Magnetic and Electric Sensors

The magnetic field data are collected using magnetic induction coils manufactured by SIO and housed in pressure cases rated to full ocean depth (Figure 18).



Figure 18. Magnetic induction coils during the manufacturing process at SIO (photo courtesy of Scripps Institution of Oceanography).

The electric field data are collected using perpendicular semi-rigid dipole arms that hold Ag-AgCl electrodes at the ends. The Ag-AgCl electrodes contain a rod of pure silver that is surrounded by AgCl saturated solution, all sealed within a porous tube into which an underwater connector is built (Figure 19). Underwater cables connect the magnetic and electric sensors to the data logger, which houses the low-noise amplifiers, clock, analog-to-digital converter (ADC), compass, and storage media.

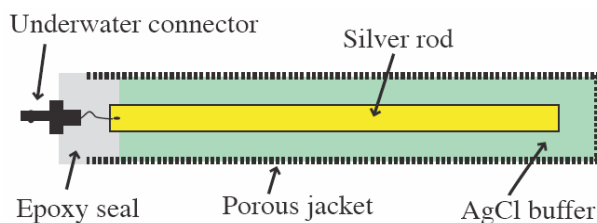


Figure 19. Schematic diagram of a Ag-AgCl electrode identifying all of the featured components (drawing courtesy of Scripps Institution of Oceanography).

Electronics

The data logger is housed inside an aluminum pressure housing that is rated to full ocean depth (~6000 m). The electronic components consist of circuitry dedicated to electric and magnetic field amplifiers, an ADC, clock, compass, and storage media (Figure 20). Custom made battery packages are mounted to the underside of the circuit board backplane, and the entire cylinder slides into the pressure tube. High pressure underwater bulkhead connectors allow sensor cables to feed sensor signal into the amplifier boards on the analog side of the data logger. Endcap ports provide serial and Ethernet communication with the data logger in order to efficiently program and download data. A vacuum port is used to exchange damp air trapped in the logger during assembly with dried air.

The acoustic unit is designed in a similar way: an aluminum pressure housing cylinder that contains a removable circuit board section with battery packs attached below (Figure 21).

The entire package is mounted on a custom-built 200 kg concrete anchor. The large anchor provides stability to the instrument, thereby reducing motional noise on the magnetic sensors. The instrument sits in concrete grooves that are designed to prevent sideways motion of the package, and it is held in place by a non-magnetic stainless steel anchor cable

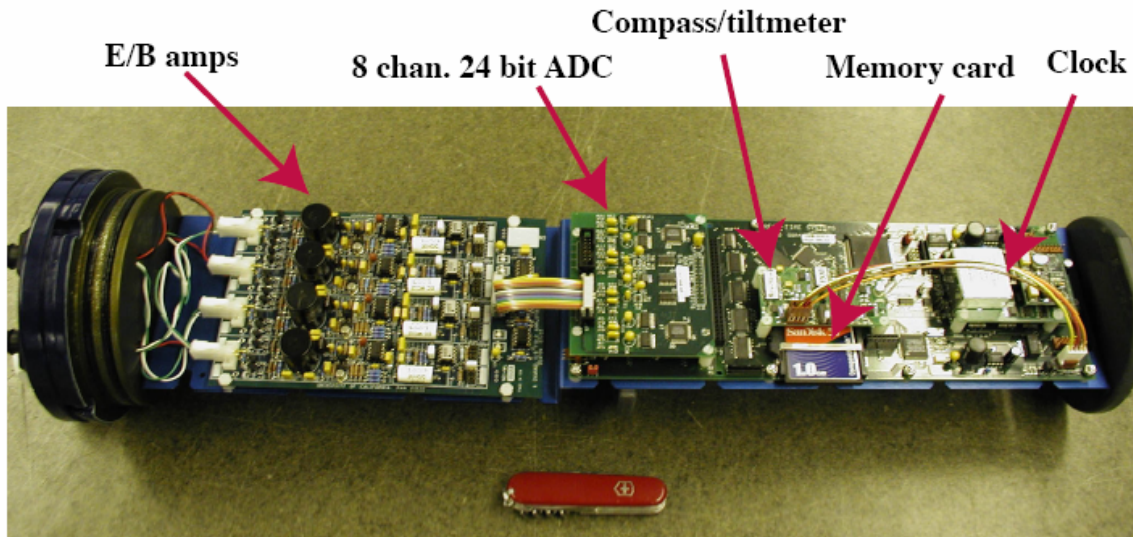


Figure 20. The SIO Mark III data logger, with key features identified (photo courtesy of Scripps Institution of Oceanography).

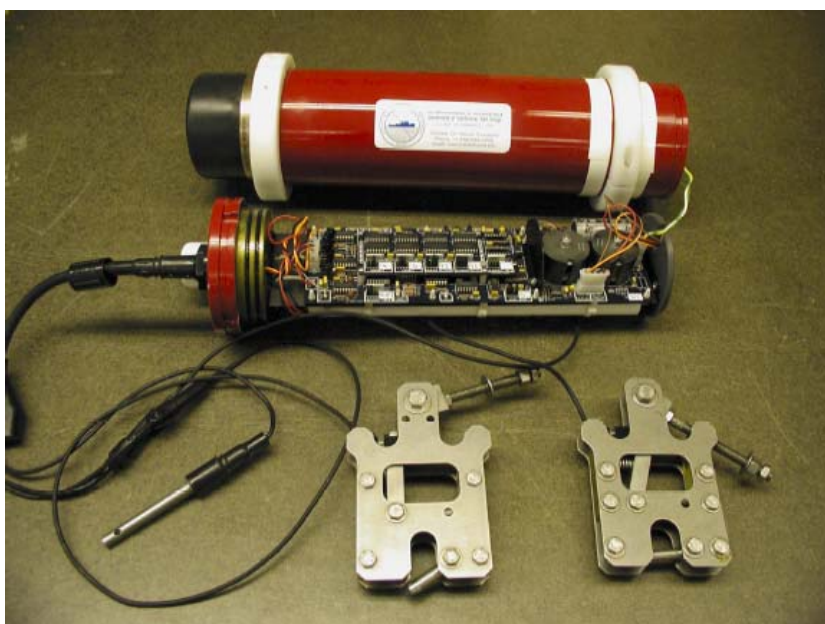


Figure 21. SIO custom acoustic unit in a deep water pressure case. Transponder is mounted to end of the pressure case, visible on the left. The battery pack and electronics slide into the pressure case and cables connect between the endcap and the mechanical release mechanisms (photo courtesy of Scripps Institution of Oceanography).

tightened to maintain good coupling between the anchor and the instrument. The anchor cable is threaded through the concrete anchor and connected to a mechanical release latch that is triggered acoustically via a burnwire (Figure 22 a and b) when the MMT receiver is called back to the surface.

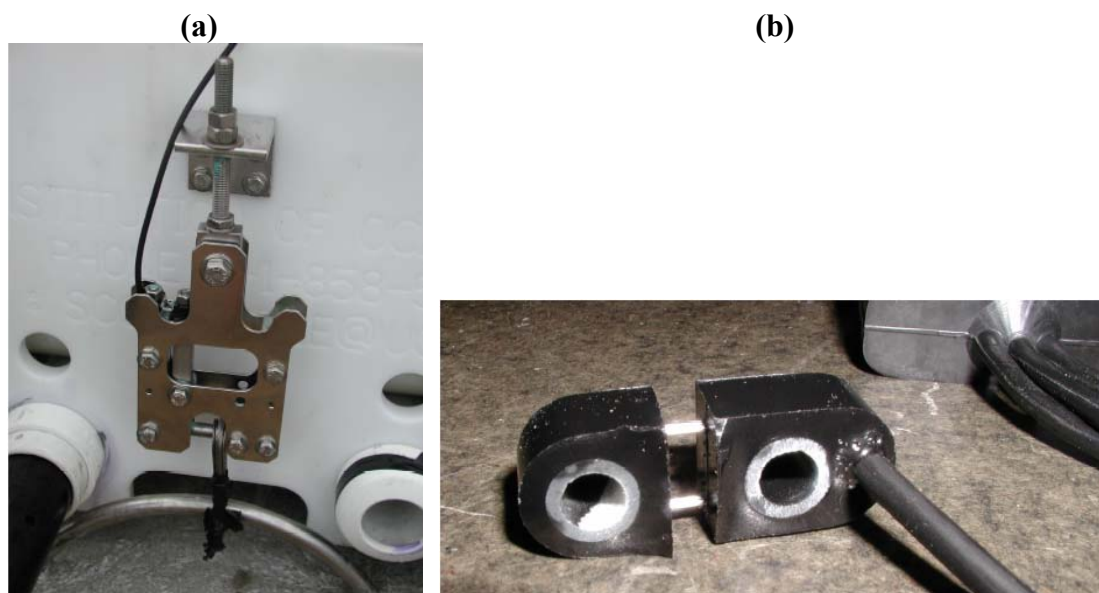


Figure 22. (a) The mechanical release attaches the frame to the concrete anchor via an anchor cable; along with (b) a close view of the acoustic burnwire, built by EdgeTech. Photo courtesy of Scripps Institution of Oceanography.

Operation

MMT receiver deployment is done by attaching the instrument package to the ship's crane via a release hook and instrument lifting strap. Once the ship arrives at the designated dropsite, the instrument package is lowered into the water by the crane and an operator pulls the release hook (Figure 23). The instrument then sinks to the seafloor where its position is measured using underwater acoustics which are tied to the ship's GPS location.

Once the units are on the seafloor, the MT receivers record the magnetic and electric variations in time and store the time series to the internal hard disk or compact flash card

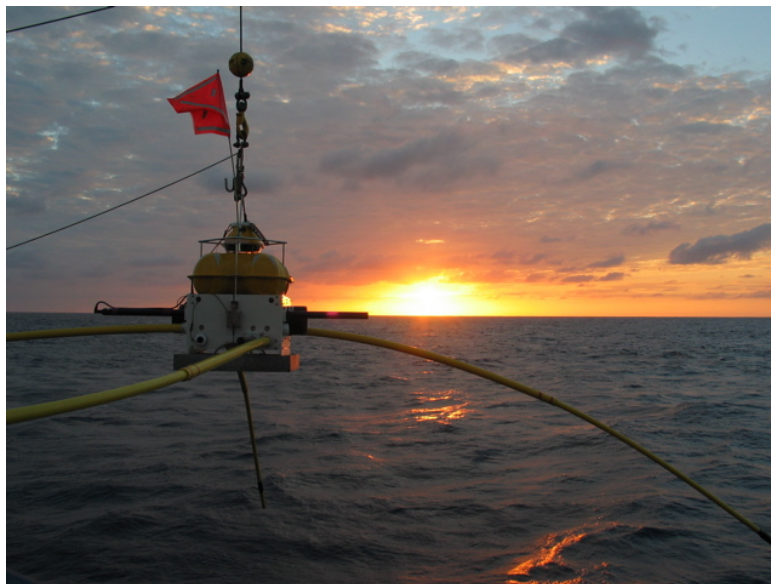


Figure 23. Seafloor MT receiver being deployed (photo courtesy of Scripps Institution of Oceanography).

(Figure 24). Typically a duration of 36 – 72 hours on the seafloor is sufficient to process MT data, but the receivers can stay on the seafloor for up to 2 months.

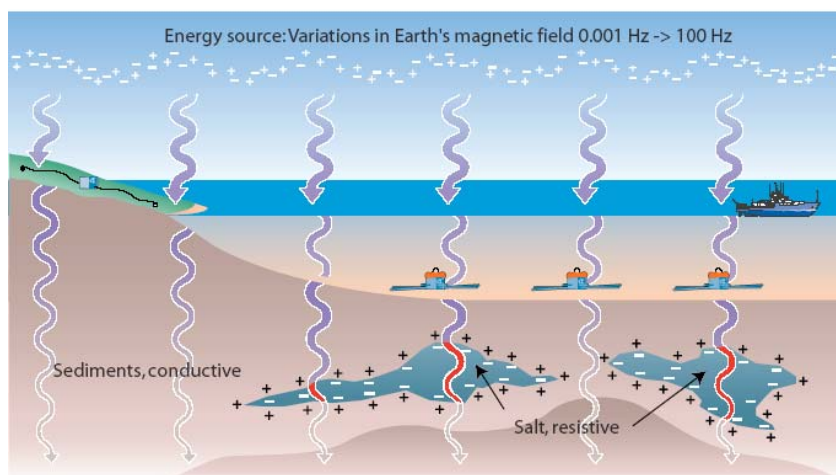


Figure 24. Cartoon drawing of the MT seafloor receivers (and land remote site on the far left) collecting the natural MT signal while stationed on the seafloor (drawing courtesy of Scripps Institution of Oceanography).

After sufficient time has elapsed, an acoustic command is sent to the housed acoustic unit which triggers a current to electrolyze the wire that is constraining the mechanical release

latch. Once the receiver is free from the concrete anchor, its own buoyancy brings it to the sea surface. The unit is monitored and tracked acoustically while it is en route to the surface. Rise times are well known and so the surface time is predicted. Once the unit is visually spotted on the sea surface, the research vessel maneuvers close to it and a grappling line is thrown to bring the instrument close enough to be transferred to the crane and pulled up onto the deck. Data are downloaded through an end port on the data logger unit and the data processing can begin (discussed later in this chapter).

THE SAN DIEGO TROUGH EXPERIMENT

Geologic Structure of San Diego Trough Area

As discussed before, the SDT lies on or near the border between two regional tectono-stratigraphic terranes – to the west is the Catalina terrane and to the east is the Santa Ana terrane (Howell and Vedder, 1981; Legg and Kammerling, 2003). The Catalina terrane is characterized by a shallow amount of sediments that are lain directly over a large metamorphic core complex made up of the high temperature, high pressure/temperature ratio Catalina schist. The Santa Ana terrane is defined by the absence of metamorphic rocks and the abundance of sediments. The peninsular batholith, the southern extension of the Sierra Nevada pluton, is also part of the Santa Ana terrane.

Due to the differing geology across the region, conductivity structure may be able to delineate the boundary between these two terranes, or at least provide insight into the complicated tectonic setting. A rough estimate of expected resistivity ranges is presented in Table 1.

Table 1. Ranges of Rock Resistivities

Rock Type	Resistivity Range (Ωm)
Shale	2 - 20
Sandstone	10 - 80
Carbonate	50 - 500
Volcaniclastic	5 - 50
Volcanic flow	100 - 4000
Metamorphic	100 - 10000
Igneous	500 - 10000

Source: Orange, A.S., 1989, Magnetotelluric exploration for hydrocarbons: Proceedings of the IEEE, **77**, No. 2, p. 288.

As shown in Table 1, there is a potentially large contrast between metamorphic rocks (such as the Catalina Schist) and the volcaniclastic sediments (of the Miocene volcanic and volcaniclastic sequences). Similarly, a large contrast is predicted between sedimentary sands/shales and metamorphic rocks.

Instruments and Deployments

Several expeditions to the San Diego Trough took place over a period of 2 years. The first study (designated as SDT-1) was completed in early April 2003, followed by another study in late April 2003 (referred to as SDT-2). Both of these expeditions acquired MMT data over a period of approximately 5 days. The third survey took place in September 2004 (called SDT-3) and the 2 MMT sites that were occupied at this time contain raw time series of 48 hours in length. The SIO-owned vessels *RV Sproul* and *RV New Horizon* were used for all of the cruises.

The instruments that were deployed on these cruises were the “Mark II” and “Mark III” generation seafloor MT receivers that were designed and manufactured at SIO. These

receivers feature orthogonal horizontal electric dipoles of 10 m in length and orthogonal magnetic coils housed in pressure cases rated to 4000 m water depth. The data logger is a 24-bit system with customized, impedance-matched amplifiers for both the electric and magnetic channels and a flashcard data storage device.

Processing Procedure

The data processing flow, from the initial data download to the selection of apparent resistivity and phase sites that will go into the 2-D inversion algorithm, is illustrated in Figure 25 and described in Chapter 4.

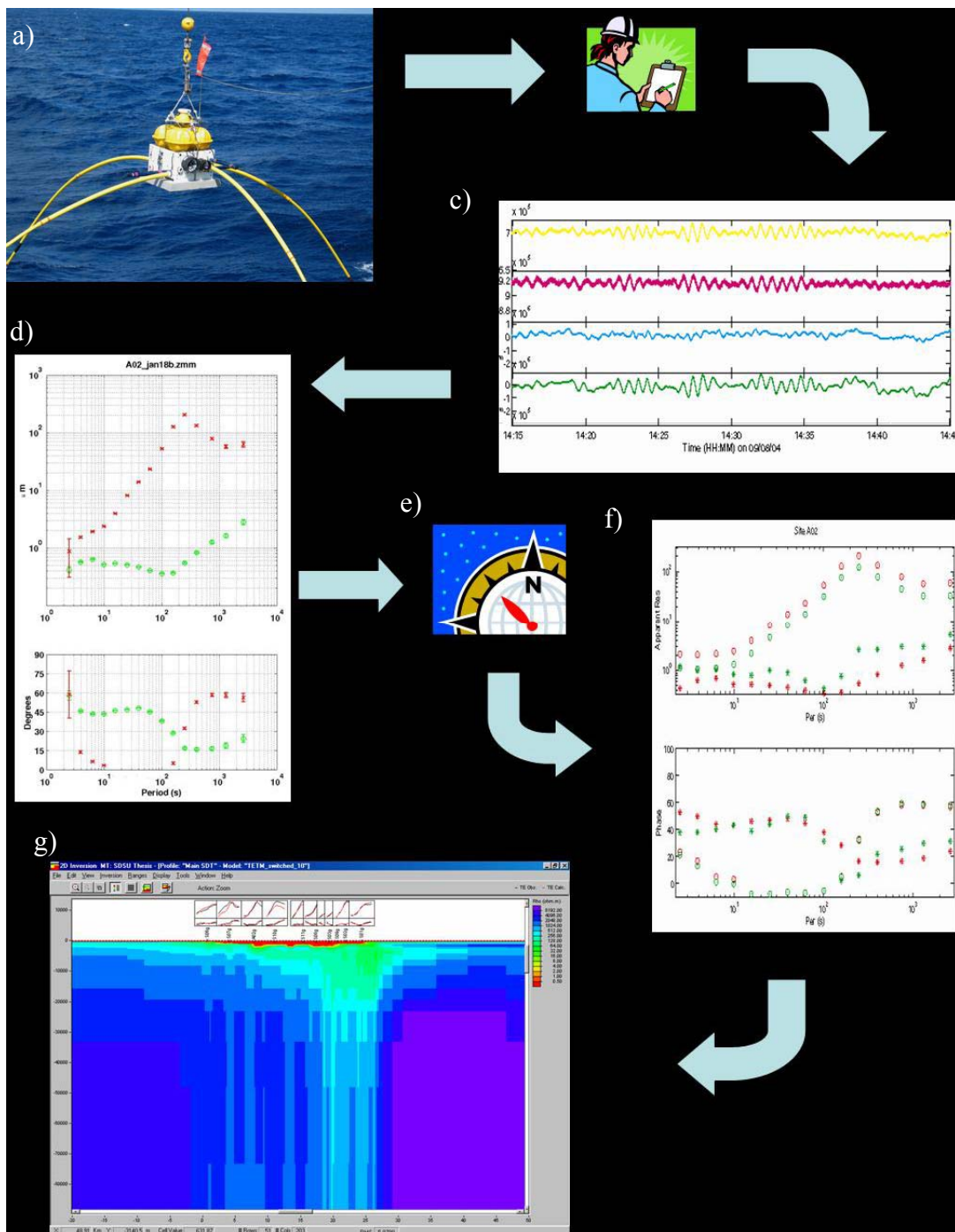


Figure 25. The process flow for handling MMT data: (a) deployment and recovery of seafloor receiver, (b) incorporating the calibration and administrative information for that site, (c) evaluating the time series, (d) computing the apparent resistivity and phase curves, (e) rotating the data to the principal directions, (f) adjusting the apparent resistivity and phase curves, and finally (g) doing a 2-D inversion on the data.

CHAPTER 4

RESULTS

The three expeditions that provided data for this investigation, while successful, were all unique in terms of data-gathering circumstances, personnel and equipment. The acquired data went through approximately the same processing procedure from the time the download cable was connected to the endcap after recovery to the importation of the apparent resistivity and phase files to the *WinGLink* inversion program.

THREE EXPEDITIONS: AN OVERVIEW

The first field study (SDT-1) resulted in the successful recovery of data from 6 sites, 5 of which contain data suitable for further processing. The six receivers that were used on this study were Mk II receivers. After the time series are downloaded from the data logger, the header information was compiled and includes the magnetic sensor calibrations, amplifier calibrations, and electric dipole lengths. The compass orientation on the seafloor was set to a dummy value for this first stage. The six sites for SDT-1 are presented in Table 2.

Table 2. SDT-1

Site	Instrument	Latitude	Longitude	Water Depth	Comments
SO1	Fruitbat	32° 34.50	117° 29.97	525 m	Fine
SO2	Quindal	32° 44.07	117° 31.54	800 m	Fine
SO3	Platypus	32° 43.24	117° 32.75	1067 m	Fine
SO4	Lerp	32° 41.44	117° 38.99	1138 m	Bad coil channel
SO5	Glider	32° 40.77	117° 41.03	1185 m	Problematic app. resistivities
SO6	Bunyip	32° 39.75	117° 44.09	370 m	Excellent quality data

The second expedition (SDT-2) collected data from another 6 sites, 4 of which contain satisfactory data for further processing. The remaining two sites appear to have satisfactory quality time series data, but because they used experimental magnetic coils which had not been calibrated in time for this investigation, they are excluded from this study. The receivers used for this study are also SIO Mk II instruments, except for the two experimental receivers that were not used for this investigation (Table 3).

Table 3. SDT-2

Site	Instrument	Latitude	Longitude	Water Depth	Comments
SO7	Wombat	32° 40.39	117° 42.08	775 m	Problematic app. resistivities
AO2	Glider	32° 41.12	117° 39.75	1150 m	Fine
SO8	Quindal	32° 42.81	117° 34.03	1100 m	Fine
SO9	Goanna	32° 43.66	117° 32.17	950 m	Fine
X016	L-012	32° 41.84	117° 37.35	1100 m	Experimental
X01	L-006	32° 42.55	117° 35.73	1100 m	Experimental

The third expedition, called SDT-3, acquired data from 2 additional MT sites in the center of the San Diego Trough. The two receivers that were used on this study are Mk III receivers (Table 4).

Table 4. SDT-3

Site	Instrument	Latitude	Longitude	Water Depth	Comments
S10	Corella	32° 41.82	117° 39.93	1130 m	Poor quality short period data
S11	Rabbit	32° 42.73	117° 35.33	1090 m	Poor quality short period data

The raw data from seafloor MT instruments across an array is innately more heterogeneous in terms of quality than the land-based equivalent due to the unknown set of

conditions on the seafloor. Several sources of noise affect the performances of the seafloor receivers: motional noise from unstable landing position or bottom currents, environmental noise from wave action and electronic noise from other parts of the MT receiver system. Although all noise is unwanted, the motional, environmental or electronic system noise only severely degrades the quality of the MT data when the noise saturates the amplifiers in the instrument.

Motional noise is the most common type of noise that plagues seafloor MT data. Although the instrument is held to the seafloor via a 200 kg concrete block and the seafloor is often covered in a layer of soft sediment, this does not guarantee a stable landing position on the seafloor. Seafloor conditions are unknown, even after the receiver has acquired its data and is back on the ship. Movement of the electric and magnetic sensors in the conductive seawater environment, even slight, creates eddy currents that induce noise on the channels. The slightest motion – instrument rocking due to landing on a slightly uneven surface, bottom or tidal currents flowing through the site area, and even wave noise due to rough stormy sea conditions – degrades the quality of the time series data. Fortunately, the data on this experiment were acquired during times of good weather and so these measurements have good quality data down to 1-2 s (with the exception of S10 and S11, which are discussed later in this chapter). There is no significant evidence for motional noise on any of the sites, although it is clear that there is a variation in the signal amplitude level (Figure 26).

Electronic noise is a bit trickier. In general, there is no electronic noise except for the predictable “disk write” noise. “Disk write” noise saturates the amplifier and produces unusable sections of MT data (Figure 27, p. 49). This occurs approximately every four hours on the SIO Mark II units when the 8 MB RAM buffer is full and needs to write the data to

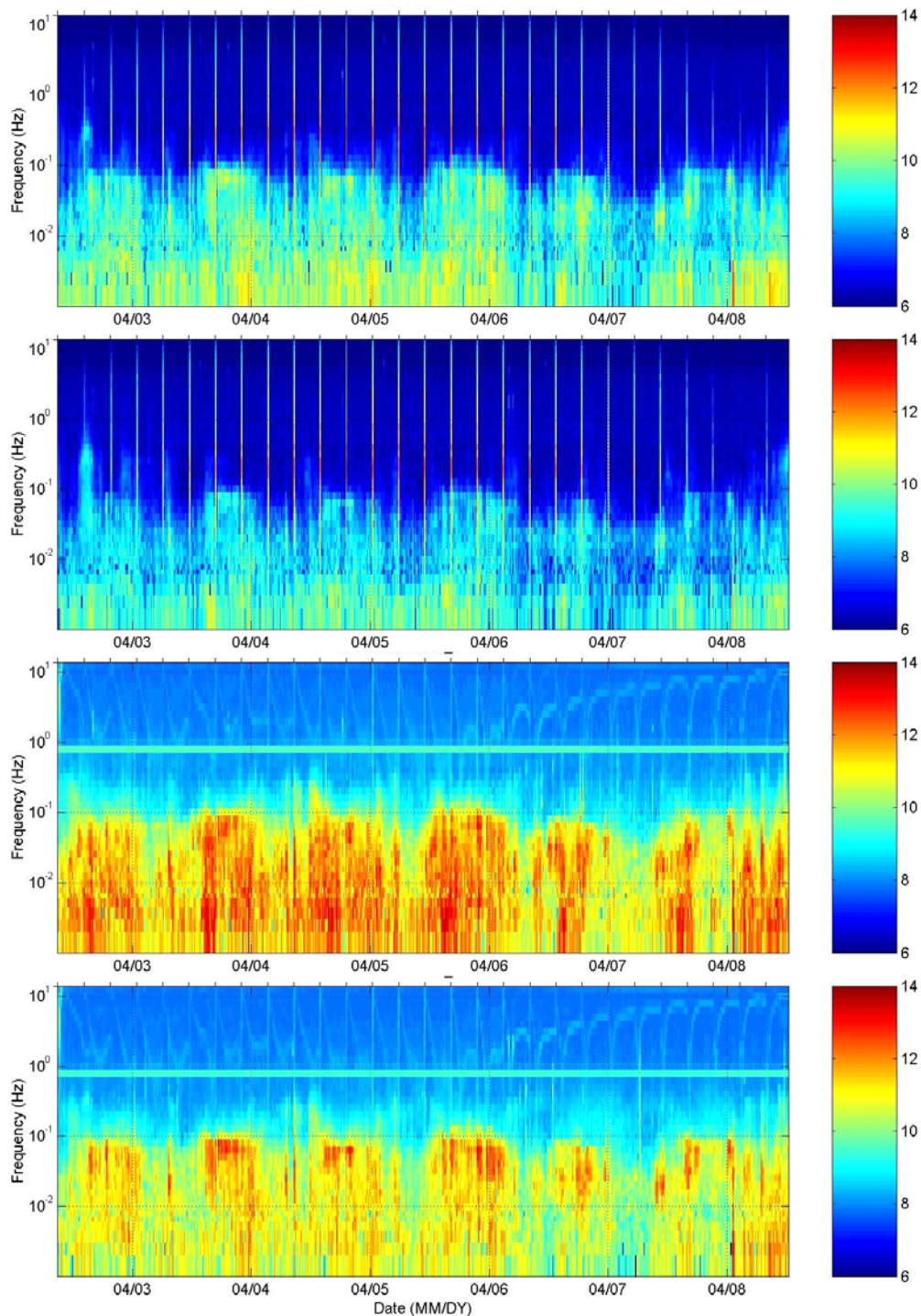


Figure 26. Frequency vs. time plot of Site S05, colors are in log amplitude. Channels are identified at the top of each subplot. The vertical streaks on channels 1 and 2 are the disk write noise. Note the increase in amplitude (hotter colors) in a regular pattern with time over the course of the 5.5 days. This is interpreted to be the effect of the diurnal variation.

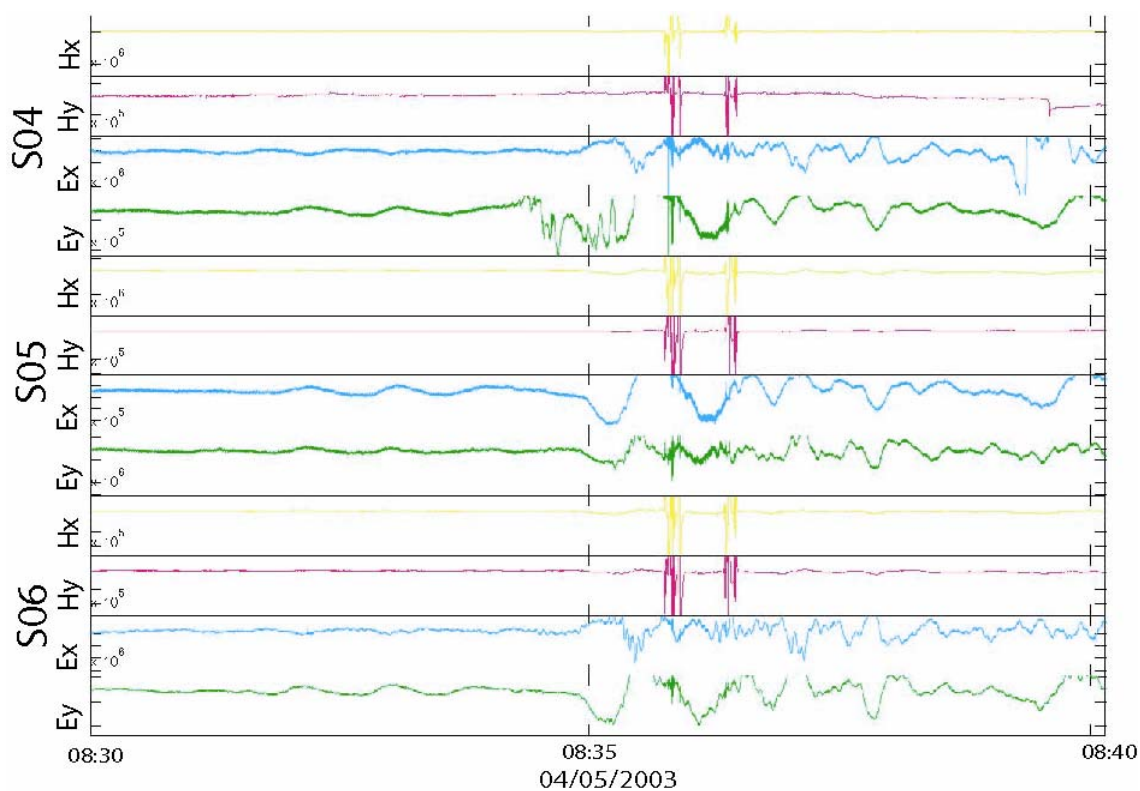


Figure 27. “Disk write” noise in ten minutes of time series data from sites S04, S05 and S06 (top to bottom). Channels ordered as yellow = Hx, magenta = Hy, blue = Ex, green = Ey. Note that the disk write data has saturated the magnetic channels and is barely visible on the electric channels.

the Seagate hard drive and the episode lasts only a few minutes. The spinning up of the hard drive creates an electronic noise that saturates the data on the magnetic channels. These sections of data are handled in Egbert’s *dnff* code as modified by Kerry Key (personal communication, July 25, 2003).

Other kinds of electronic noise appear occasionally in MMT time series data. This noise often takes the form of “spikes” in the data on one or more channels. Spiky data are thought to be caused by some kind of undiagnosed interaction of the electronics with the electric and magnetic sensors. Examples of good quality raw time series data from each of the channels on each of the instruments used in this investigation are given in Figures 28, 29, and 30 (pp. 50-51).

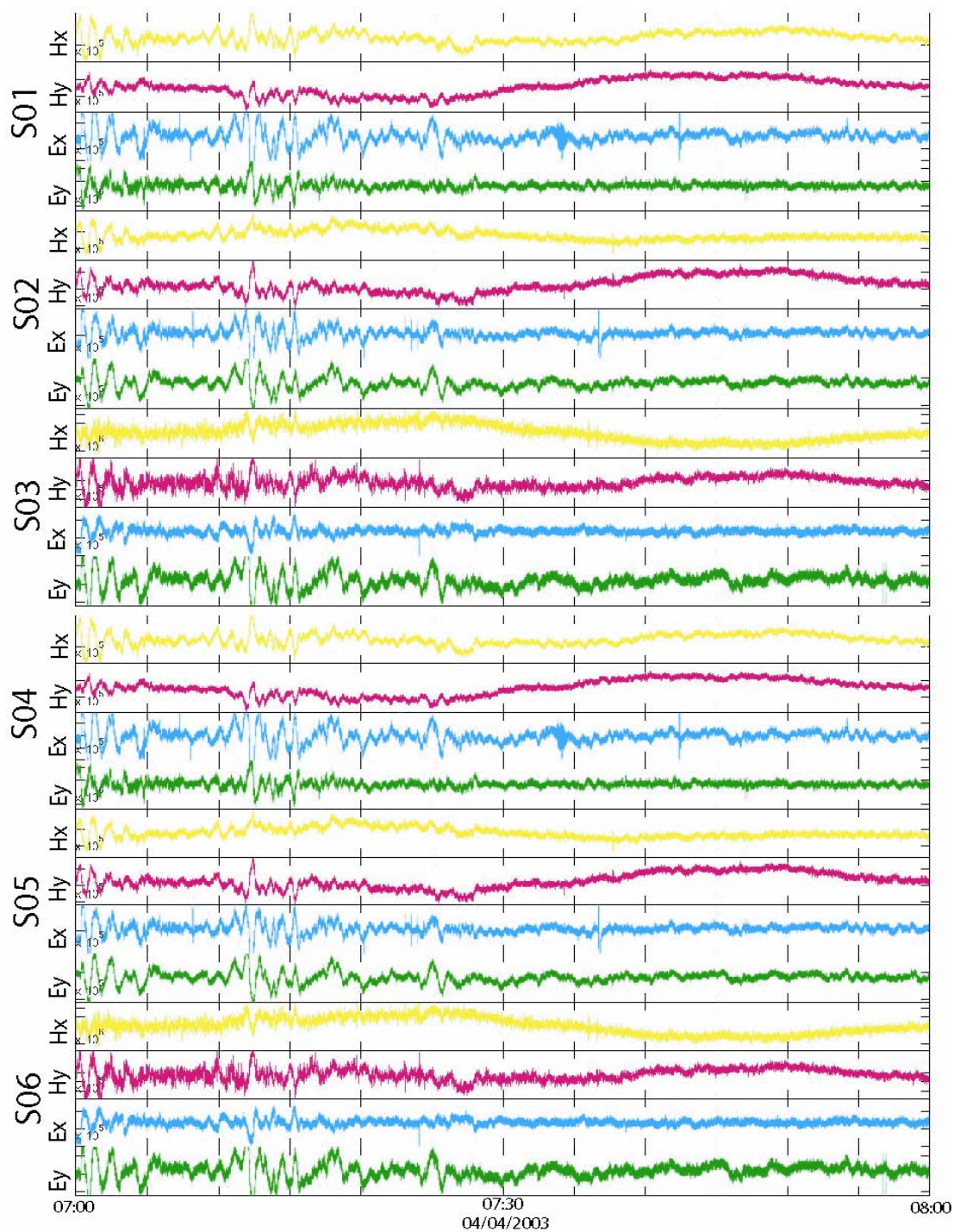


Figure 28. One hour of time series data from sites S01, S02, S03, S04, S05 and S06 (from the top down). Channels ordered as yellow = Hx, magenta = Hy, blue = Ex, green = Ey. These six sites were acquired during the first expedition (SDT-1).

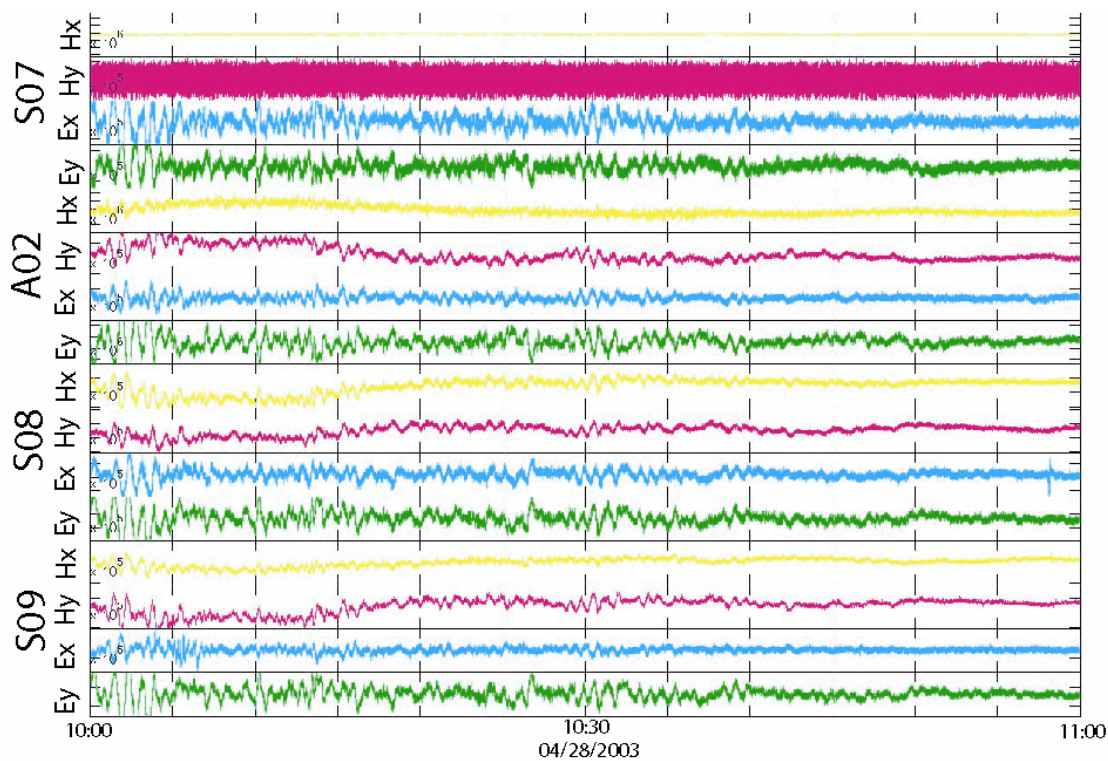


Figure 29. One hour of time series data from sites S07, A02, S08 and S09 (top to bottom). Yellow = Hx, magenta = Hy, blue = Ex, green = Ey. These data were acquired during the second expedition (SDT-2).

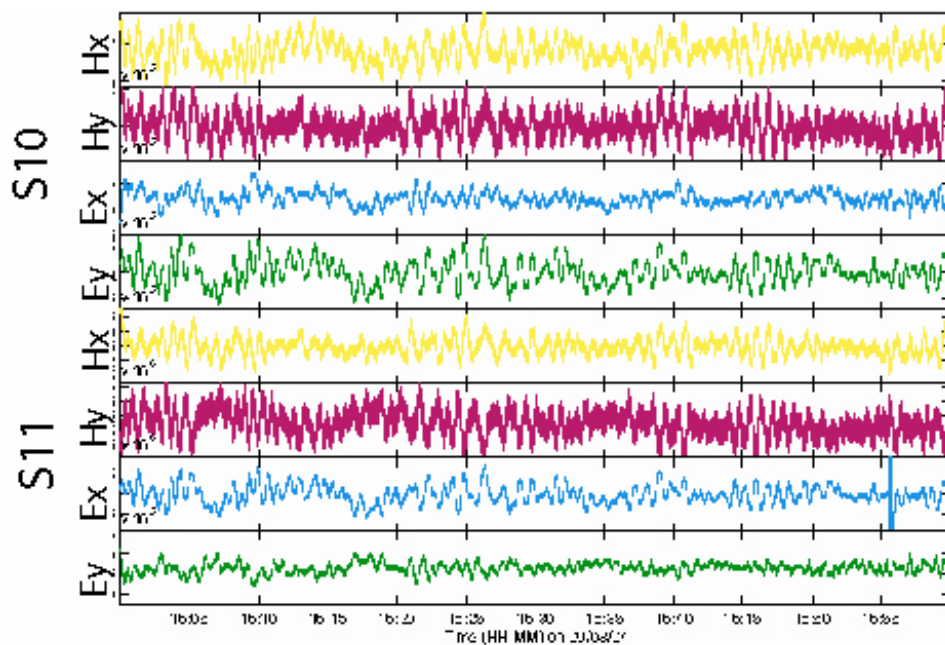


Figure 30. One hour of time series data from sites S10 and S11. Yellow = Hx, magenta = Hy, blue = Ex, green = Ey. These data were acquired during the third expedition (SDT-3).

FREQUENCY DOMAIN RESPONSES

Computing the apparent resistivity and impedance phase curves requires converting the time series data to the frequency domain. The resulting complex Fourier coefficients for each site are used in the multi-station impedance calculation. Data from each group of sites that measured the electric and magnetic signals at the same time stay together throughout this calculation so that the incoherent noise can be removed from all the data. The responses that result from this multi-station MT impedance calculation are unrotated, but will be rotated to the principal axes at a later stage.

The apparent resistivity and impedance phase plots, both before and after Groom-Bailey (G-B) decomposition are presented in Appendix A. A subjective, qualitative evaluation for the twelve acquired sites is as follows:

- 1 Site S06 – excellent quality
- 2 Sites S01, S02, S03, S08, S09 and A02 – good quality
- 3 Sites S10 and S11 – noisy short period data (shorter than 20 s)
- 4 Site S07 – satisfactory quality
- 5 Site S05 – good time series data but unusable apparent resistivity and phase curves.
- 6 Site S04 – dead magnetic channel, therefore it is unusable.

The majority of the data sets are good quality, but there must be some discussion as to why three of the sites (S05, S10 and S11) have problems.

Noisy Short Period Data

The lowest period data point on the apparent resistivity curve for S10 is at 30 s, and for site S11 the lowest period data point is at 20 s. A possible explanation for this unfortunate reduction in the short period limits is a design change in the equipment that

occurred during the lapsed time between the first two expeditions and the third expedition. A change in the process for manufacturing and calibrating the magnetic coils resulted in a new generation of magnetic coil that is 0.5 m longer than the previous generation. The results from other studies using this equipment have identified similar problems with the short period data from seafloor receivers that have used this newest generation of magnetic coil. The additional coil length may in fact leave the instrument more susceptible to motion on the seafloor resulting in noisier magnetic field data.

3-D Effects

Site S05 produced reasonable looking time series data on all channels. However, when the impedance tensor was calculated, the resulting apparent resistivity and phase curves were markedly different from the other sites along the profile. The G-B analysis for this site shows very unusual results (Figure 31). One possible reason for this is the location of site S05 in the close vicinity of the “landslide complex” at the base of Thirtymile Bank (Figure 7). If the receiver had landed anywhere close to this escarpment, there would certainly be 3-D effects from this feature. Similarly, if the receiver had landed in a tilted orientation, that would also explain the unusual results. Because it is unknown where or how exactly the receiver landed on the seafloor, this is the only reasonable explanation for problematic apparent resistivity and phase data, especially since the time series from this site looked reasonable.

Negative Phases

Several of the data sets from sites along this profile have apparent resistivities that climb more steeply than the accepted 45° angle for layered Earth and which have

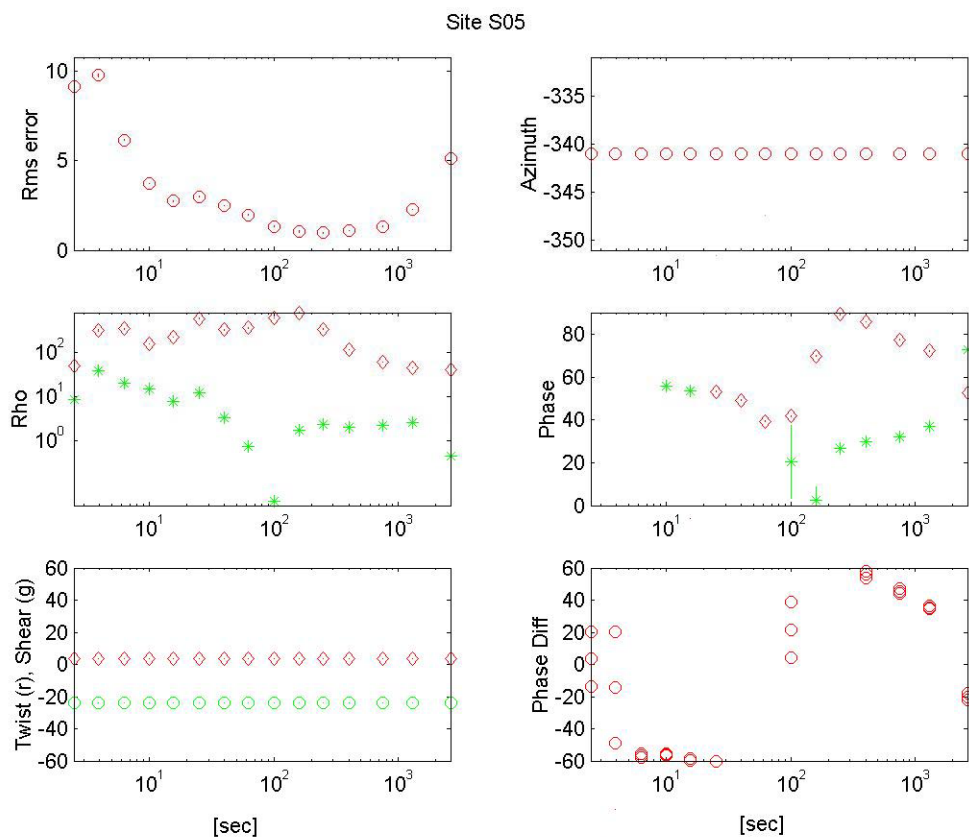


Figure 31. G-B analysis for Site S05, with problematic results for phase and phase difference, as well as the high RMS error values in the 1-30 s period range. The apparent resistivities appear to be reasonable alone, but compared to the rest of the seafloor MT sites, these curves are markedly different.

accompanying phases with negative values (Figure 32). Although these features are very unusual in the land MT environment (usually revealing 3-D data), they are common for marine MT data sets (S. Constable, personal communication, March 11, 2005). The explanation for this phenomenon lies in the environmental conditions in which the MT receiver acquires data. On land, all of the current density, J , flows in the ground and not in the air because of the infinitely high resistivity of air. In the marine environment, the presence of a conductive ocean layer above the location of the seafloor receiver means that current flows across the seafloor boundary. The extensive 2-D structure in the seafloor

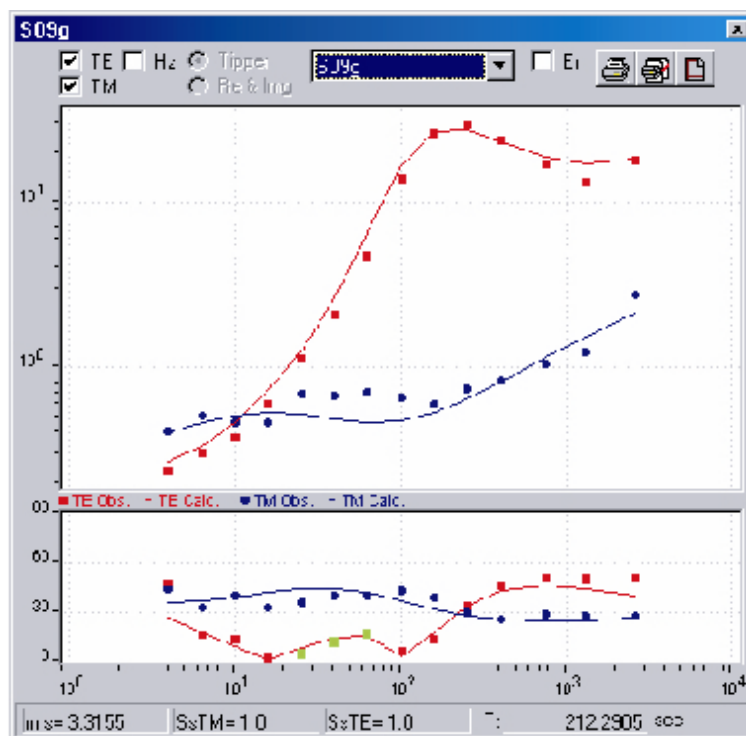


Figure 32. Site S09 apparent resistivity (top) and phase curves (bottom) with the TE (red squares) and the TM (blue circles) mode data points and the model fits (straight lines) through the data. Note that although the phases are negative (green data points in TE curve) and the apparent resistivity is steeply climbing, the model fits the data well.

bathymetry adds boundaries and obstacles to the current flow that may explain the steeply ascending apparent resistivity curves and negative phases.

ROTATIONS AND DECOMPOSITION

Each site of seafloor MT must be rotated from the landing orientation on the seafloor to the principal directions. The three sets of data were each handled slightly differently in terms of azimuthal impedance rotations. The first two sets were rotated to principal directions and the landing orientation was calculated by output files from Egbert's *multmtrn* code, constrained by the land remote site. The third set of data was simply put through the G-B decomposition because one of the principal directions was being adequately revealed as

the strike direction by this process. The premise for being able to use the G-B decomposition, as explained previously, is that the San Diego Trough is a 2-D structure that should be able to be constrained to a 2-D impedance calculation. Polar diagrams show the dimensionality of each site with frequency. The polar diagrams for each of the sites used in this investigation are detailed in Appendix B.

The use of the G-B decomposition method to rotate the data to regional strike means that the TE and TM modes would have been known. However, the TE and TM modes for this study were identified based on previous experience, with the TE mode on top as the more resistive curve and the TM mode on the bottom. The depressed apparent resistivity values in TM mode are characteristic of galvanic effects that occur on the conductive side of bathymetric structure (S. Constable, personal communication, March 11, 2005).

The question about whether it is appropriate or not to decompose marine MT data was evaluated. The application of the Groom-Bailey decomposition method is standard on land due to the well-known effects of local galvanic distortion. However, in the marine environment it is unclear if decomposition helps to contribute to a correct, final inversion result. The argument for not decomposing the data is that the bathymetric effects should not be removed since the marine model inversion needs that information in order to invert properly. This argument has merit if the local bathymetry is 2-D but not if it is 3-D.

Applying Groom-Bailey decomposition forces the impedance tensor into a 2-D regime (where $Z_{xy} = Z_{yx} = 0$, as discussed in Chapter 3). The argument for applying the Groom-Bailey decomposition to this data set is that this study area has a 2-D regional setting; the geologic strike of the San Diego Trough is clearly N30°W. Both the Thirtymile and the Coronado Banks have fault-controlled escarpments trending N30°W, and the San Diego

Trough fault which is mapped directly through the center of the basin also trends N30°W.

An example of the impedance tensor values before and after G-B decomposition is illustrated in Figure 33. These curves are typical for the G-B decomposition results in this study. The complete set of before and after G-B analysis plots is given in Appendix C.

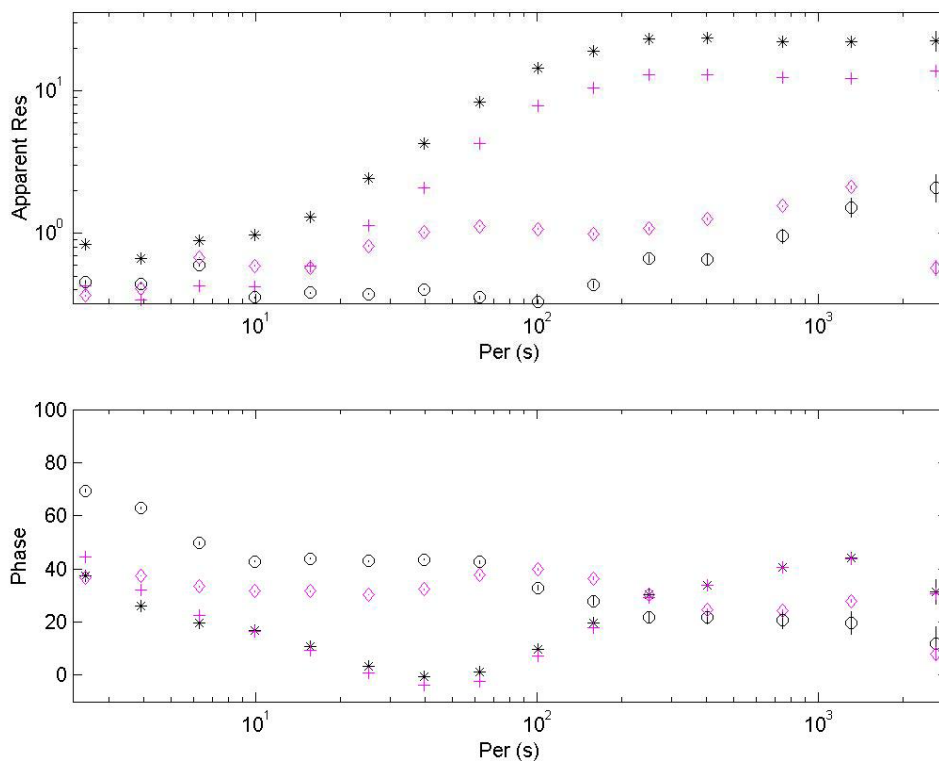


Figure 33. Apparent resistivity and phase results before and after G-B decomposition. Dark = before, light = after; stars = TE, circles = TM.

Since Egbert's code assumes that the operator knows what the orientations of the instruments are, it is at this stage that the typical (land) processor would merely rotate these data to the regional strike. In the marine environment the landing orientation of the seafloor receiver is unknown (as discussed in the Instrumentation section). Therefore, at this stage of the processing, only dummy rotation angles of 0° and 90° are used for the 4 channels (2 electric and 2 magnetic). Once all the data have been processed by the *dnff* and *multmtrn*

programs, it is possible to use the output files from the *multmtrn* code to find the maximum rotation angles using a coherency method. This is done by holding one site fixed (e.g., the land remote site) and then aligning each site's principal impedance directions to the fixed site. The amount of rotation needed to align with the fixed site can then be added to the dummy values to obtain the landing orientation of the data logger on the seafloor.

This iterative process of holding one site fixed and solving for the rotation angles of the other sites works best when there is a land remote site since it is the only site whose orientation is known. The process keeps going until the user is convinced that the rotation directions that have been solved for are the correct ones. Then those new orientation angles are fed back into the original calibration file and the entire process starts again. The final values from the *multmtrn* program are the values that are used in the *WinGLink* inversion regime.

Below are the orientations of the x-directed sensors at the different sites that were calculated using the above procedure:

S01	S02	S03	S05	S06	S07	S08	S09	A02
160°	110°	70°	130°	90°	210°	100°	60°	240°

It should be noted that the procedure to constrain the seafloor orientations was only followed during the first two of the three expeditions in this study because there was also no land remote site during the SDT-3 to provide a known orientation.

A wider band is processed than the data will support, because the short periods are limited by seawater attenuation and the long period are limited by sensor response functions. The limits are evident in the form of outlying or ill-fitting data points and large error bars. It is common to edit out the ill-fitting data points after examining the apparent resistivity and

phase curves. The data set for this study included several sites that had some of the data points removed.

Groom-Bailey Decomposition

MT acquisition requires that orthogonal electric and magnetic time series data are collected simultaneously. The seafloor MT data presented in this thesis do not include a reliable azimuthal measurement of the orthogonal electric and magnetic sensors on the seafloor relative to Earth's magnetic field. Although the data logger actually records compass and tiltmeter values, other hardware inside the data logging system has unfortunately been shown to influence the readings, thus making the measurements unreliable. Therefore, the orientation of the receiver package on the seafloor is ambiguous.

It is normal practice to use the "landing" orientation of the instrument package on the seafloor to rotate each MT tensor collected to a consistent regional geologic strike direction as discussed above. Given that the calculated apparent resistivity and phase curves can vary significantly with even a slight angular rotation of the MT tensor, the lack of orientation is a potentially serious problem. However, under certain sets of conditions it appears to be the case that the "landing" orientation of the package is not important if the MT tensor data are handled carefully and properly. These conditions are met if there is a consistent, regional, 2-D geoelectric strike that strongly influences all MT responses in the survey area in a clear manner.

In previous reports of MMT data analysis, the processing procedure has been to rotate each site until the impedance tensor is at maximum coherency and the diagonal elements Z_{xx} and Z_{yy} are minimized. This approach assumes a quasi 2-D earth structure, not accounting for any surface heterogeneity or local distortions. The rotated impedance tensor is then

assumed to yield values in the two principal directions, one of which is the strike direction. The amount of rotation required to orient the impedance tensor to the principal directions can be used to ascertain the receiver's absolute orientation on the seafloor provided that the regional geoelectric strike can be estimated by other means such as a bathymetric map and/or geologic structure. If the geology in the region is perfectly 2-D and devoid of heterogeneities and local distortion, then this is a valid method. However, because the acquisition surface at the bottom of the ocean is unknown and likely to contain local features which could influence the data, simply rotating the impedance tensor as above can lead to errors in the final MT response function, as has been discussed at length by Jones and Groom (1993).

“Strike” Program

In order to reduce errors in the final rotated MT response function, methodology described by Groom and Bailey (1989) and utilized by McNiece and Jones (2001) in their recently developed algorithm called “*Strike*” was applied. The G-B decomposition method attempts to reduce the MT tensor distortion effects due to local inhomogeneities and aligns the tensor responses in the overall regional principal directions. Because the strike direction often varies with MT sounding depth (or increasing period), the aim was to find a single strike direction that was representative of the major tectonic fabric in the area, and then align all of the MT tensor results along a profile with that direction.

Although each site had an unknown landing orientation on the seafloor, each site was handled using the same sequence of analytical steps during the implementation of *Strike*. Plotting the misfits for the underlying model that are automatically output by the *Strike* program enables the user to confirm that the distortion removal and rotation results are reasonable. Qualitatively, the final responses can be evaluated for consistency from site to

site to assure that the final rotated responses match those expected from a dominant 2-D structure.

The key assumption in this approach, as discussed above, is that there is a single, regional 2-D geoelectric strike that is applicable to all sites on the profile. In the present case, the linear valley and parallel faulting patterns of the San Diego Trough strongly suggest that such a condition is met (as discussed in Chapter 2). When constructing a 2-D model, the same assumption of a strike direction must be made, with a direction of conductivity invariance that is aligned with the strike of the data.

INVERSION

Regularized Inversion Methods

The inversion of electromagnetic sounding data does not yield a unique solution. The standard approach to solving nonlinear inverse problems in MT applications uses successive iterations and linearized inversion. There are several methods available in the public domain (e.g., Rodi and Mackie, 2001; Constable et al, 1987). Most geophysical inverse schemes depend on a sequence of forward modeling where the successive responses are compared to the data. The different schemes use different approaches to searching through model space and to select a preferred model. Most types of inversion used to treat MT data use a first-order Taylor expansion to provide a perturbation to a reference model from which a new forward response is calculated and compared to the data. This iterative process continues until convergence to a predetermined error in matching the data. MT inversions also undergo regularization, which involves simultaneously minimizing the data misfit as well as some other undesirable feature of the model (de Groot-Hedlin and Constable, 2004). If such an

approach is not taken, the resulting models will likely contain spurious features that are not required by the data (Constable et al., 1987).

2-D WinGLink

The data presented in this thesis were inverted using the *WinGLink* program developed by GeosystemTM which utilizes the non-linear conjugate gradient (NLCG) algorithm. This algorithm finds regularized solutions to the 2-D inverse problem for MT data by attempting to minimize an objective function that is the sum of the normalized data misfits and the smoothness of the model. The NLCG method solves minimization problems that are not quadratic, selectively penalizing data residuals and spatial derivatives of resistivity distribution (Rodi and Mackie, 2001). The tradeoff between data misfit and model smoothness is controlled by the regularization parameter tau, where a low value maintains a closer fit to the actual data and a high value sacrifices fit for smoothness. The program inverts using a user-defined 2-D mesh of resistivity blocks, extending laterally and downwards, incorporating topography as well.

One issue that is unique to marine MT data is the effect of seafloor topography, which was discussed previously in this chapter. There are currently several approaches that have been taken to account for the effects of topography. One is to strip out the effects of bathymetry by adjusting the model to look flat (Baba and Seama, 2002). Another approach is to incorporate a simplified version of the bathymetry into the forward calculation used by the inversion routine. The latter approach is the one adopted for this data set.

Modeling was started by generating a fine marine mesh that incorporated each site's location and water depth. Producing the bathymetry that is used in the model is a result of comparing the interpolation between sites with a bathymetric map of the area and trying to

incorporate the seafloor features that are present. Because the San Diego Trough is a relatively flat basin that is bound by the Thirtymile Bank to the west and the Coronado Bank to the east, the resulting topographic section defined for the inversion is fairly simple.

The mesh was further refined by increasing the number of cells both vertically and horizontally in the top 1200 m of the section. The approximate location of the coastline was measured and inserted into the model and a marine section 60 km to the west was also provided. No bathymetry was added to either side of the study area, although there is significant seafloor topographic variation present, especially to the west. It is also important to make sure that station locations have several mesh elements between the station and any sharp changes in bathymetry (Baba and Chave, 2004). This means that the mesh is larger than might be normally used for this number of stations, but is required to give an accurate forward solution.

All of the basins in the CCB are oriented approximately the same direction (~N30W) and the San Diego Trough is no exception. Therefore, this basin is assumed to be 2-D, and this is the premise for all of the processing, inversion and interpretation that has been completed for this study.

Inversion Process

The process of verifying the need for a feature in question involves determining if it is required by the data. This can be done by removing that feature from the working model and then re-running the inversion with this as a starting model to see if that feature comes back as the algorithm tries to lower the RMS misfit while smoothing out the data.

Alternatively, a forward model can be run with and without the feature in question, and if the RMS errors for stations near the feature go unchanged, then the feature cannot be resolved.

Both of these methods were utilized during the process of determining what features are ‘real’ and what are not.

By varying the smoothing parameter ‘tau’ in *WinGLink* and evaluating the RMS misfit accordingly, the optimal fit and smoothness can be attained for the model. Figure 34 shows the numerical analysis that was done for this data set, with the TE mode on the top curve and the TM curve on the bottom.

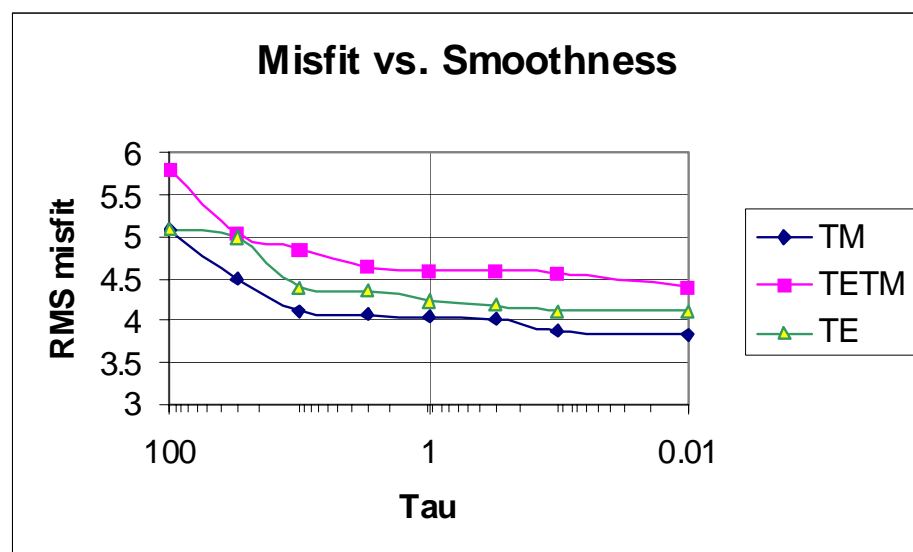


Figure 34. Trade-off between RMS misfit and tau (smoothing parameter) values. The preferred model has a tau of 1 with a RMS misfit of 4.52.

Modeling Results

All of the models started with a half-space or a near half-space. Two-dimensional inversions were initially computed using TE only mode, TM only mode, and then joint modes. The tau values started at 0.01, which means that the inversion algorithm tried to fit the apparent resistivity curves and phases closely, using errors of 10% for the apparent resistivity and 5° for the impedance phases. As the inversions converged to a RMS error that stabilized and would not reduce further, a new inversion was started using a higher value of

tau. The trade-off between RMS misfits and tau values representing model smoothness can only be matched to the specific data set using trial and error.

Although there are several features of the *WinGLink* program that can be varied and potentially affect the inversion results, all of these data were inverted using a consistent set of *WinGLink* features. The ‘uniform’ smoothing algorithm was used rather than the ‘standard’ smoothing algorithm. The ‘uniform’ grid smoothing algorithm assumes that for the purposes of computing the regularization function that the dimensions of the model are all equal. This smoothing algorithm may smear features both vertically and horizontally (*WinGLink* manual). The ‘standard’ smoothing algorithm uses a definition of smoothness that is consistent with the model dimensions. Error values for the data were also kept constant across the series of inversions, as was the marine mesh. *WinGLink* was only recently modified to handle seafloor bathymetry, and several bugs were encountered and had to be rectified.

Multiple sets of 2-D inversion configurations were run on these data: over-rotated data, data with and without Groom-Bailey decomposition, and of course the correct configuration. Although the reversed mode inversions and the over-rotated inversions resulted in models that are not part of the final analysis, the results that came out of this inadvertent experimentation were initially misleading.

The joint mode inversion should achieve a reasonable misfit between the observed and calculated data with no obvious bias errors in fits between stations. One reason for this is the influence of topography on the data which is demonstrably 2-D with an obvious strike direction. The responses in the data for each mode are a combination of the effects of underlying geology and the interaction of the seafloor topography with this geology.

Although algorithms to untangle the effects of topography have been developed, they are not available for use in this data set. Instead, a simulation of the topography is included in the inversions. Since the effects of topography are very different for each mode of data (Schwalenberg and Edwards, 2004), selecting proper TE and TM modes means that the topography is properly accounted for. If the modes are incorrectly identified, then the TM style topographic effects will be applied to TE mode data and vice-versa. This is, as stated above, likely to lead to inconsistent models when each mode is inverted alone and results are compared.

Comparison of Models

Inversions of the San Diego Trough data set were run using two methods: (1) decomposing each site's impedance tensor using the Groom-Bailey method and then inverting the resulting apparent resistivity and phase data, and (2) not applying the G-B decomposition method but merely rotating the impedance tensor using the maximum coherency method and then inverting the resulting apparent resistivity and phase data. As mentioned above, the reason for doing this is the uncertainty in what is best practice for handling seafloor MT data.

The model results for these two methods show noticeable differences, although the basic inversion model is similar (Figure 35).

Persistent Features

Using the chosen configuration of TE apparent resistivity curve on top and TM on the bottom, a simple and persistent resistivity structure came through for the San Diego Trough

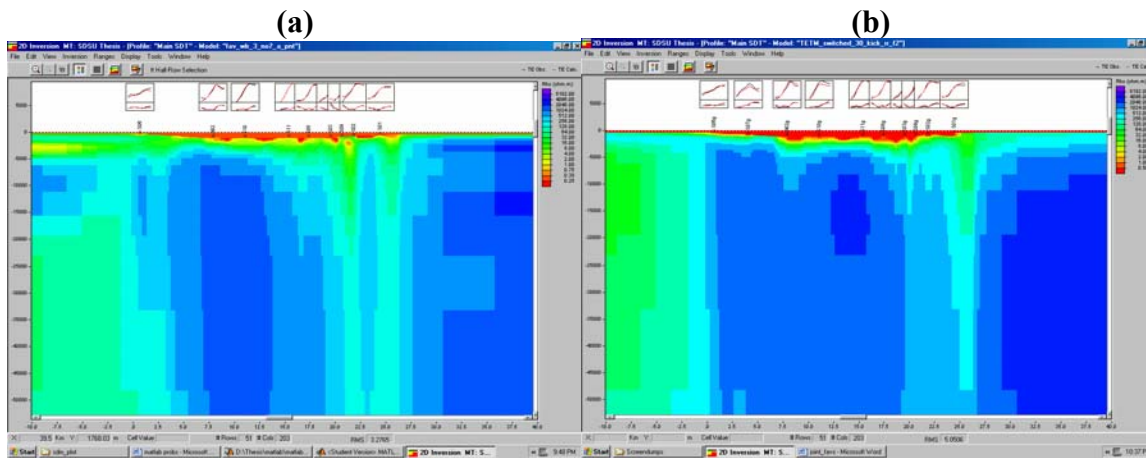


Figure 35. (a) Undecomposed inversion model and (b) decomposed inversion model using G-B analysis.

MT profile. The description, discussion and interpretation of these features are detailed in Chapter 5.

CHAPTER 5

DISCUSSION

This thesis has presented results from the first resistivity investigation conducted in the offshore California borderland region. The resulting resistivity distribution of the subsurface below the San Diego Trough region is qualified by good quality data and thorough analysis of the time series, impedance tensors, and inversion results. Furthermore, the persistent features in the data are consistent with other geophysical and geological data from the same region, or close by. However, there are also features of these data that are not easily explained by geologic information but which are sufficiently well-constrained by the data that they may shed light on previously unknown processes that have occurred within the CCB.

PERSISTENT FEATURES

Using the chosen configuration of TE and TM modes (discussed in detail in Chapter 4), a simple and persistent resistivity structure appears in inversions of data across the San Diego Trough (Figure 36). The five persistent features that the inversion process revealed are:

1. A region of high conductivity ($0.25 - 10 \Omega\text{m}$) in the top 1-2 km below the seafloor, consistent with the presence of largely unconsolidated sediments.
2. An undulating basal boundary to the conductive part of the basin that shallows on the west end to less than 1 km and slopes eastward at approximately $30^\circ - 40^\circ$ to a depth of about 5 km.
3. A narrow region of conductive zones ($10-50 \Omega\text{m}$) that are present from the surface down to 30 km in the eastern half of the basin.

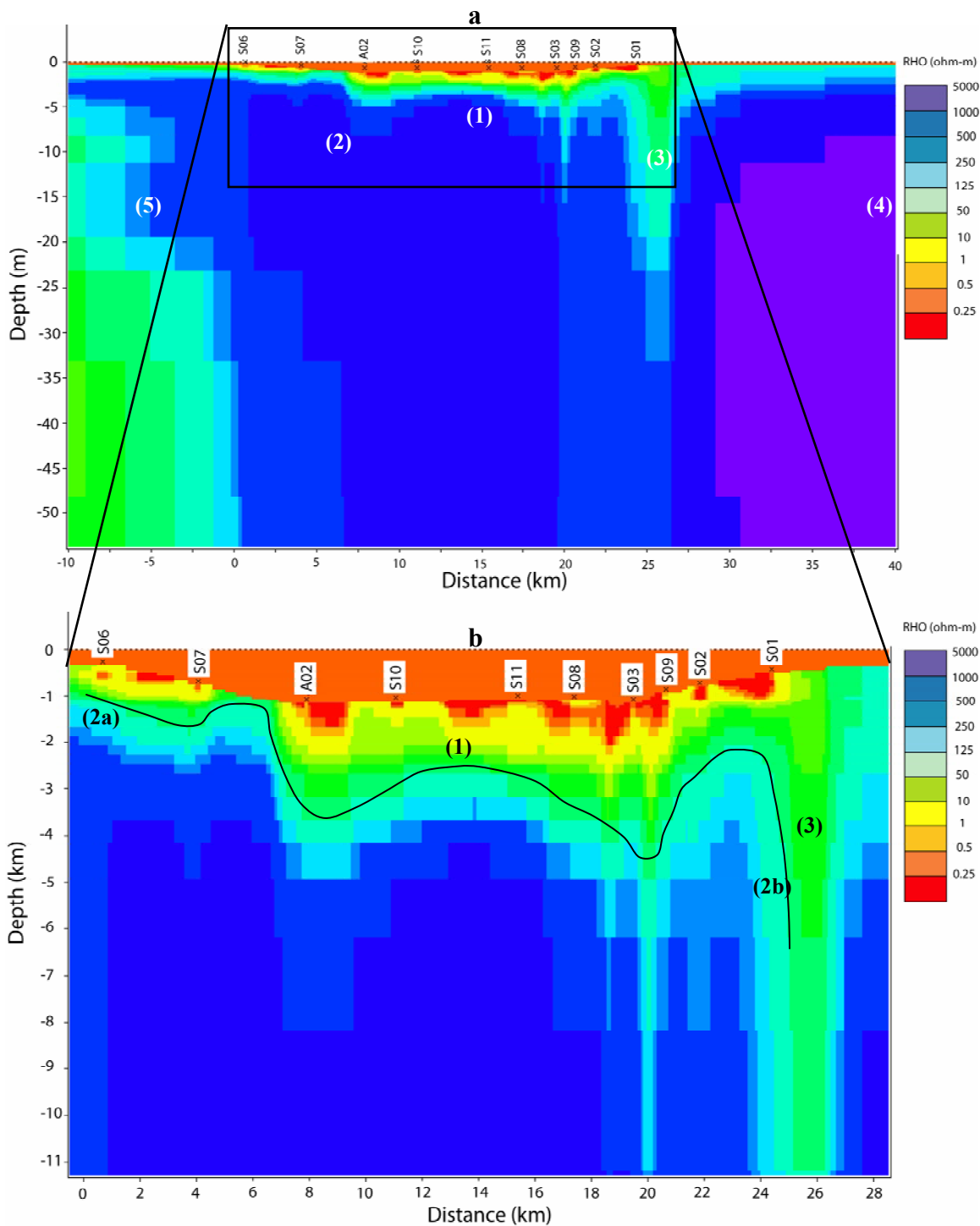


Figure 36. Joint modes 2-D inversion preferred model of the San Diego Trough. The lower graphic (b) is the zoomed in view of the top graphic (a). Persistent features identified in Figure 37a as (1), (2), (3), (4) and (5) with the detailed discussion in the text. Figure 37b includes a line marking the 50 Ω m contour, with features (1), (2a), (2b), and (3) detailed in the text.

4. A resistive section off to the east of the profile that is present from the surface down to 50 km.
5. A conductive section off to the west of the profile that is present from the surface down to 50 km.

All of these features are present in the joint mode inversions. Some of them are present in the response of one mode but not the other. There are some major differences between the TE and TM individual mode inversions. Although it is generally agreed that model results of the separate mode inversions should yield similar 2-D models, this case highlights the fact that the two modes are actually sensitive to different features in the marine environment (as discussed in Chapter 3). The joint mode inversions contain the common features that the two modes share as well as the robust features that each individual mode requires.

(1) Conductive Shallow Sediments

The resistivities from the seafloor down to ~1500 m below the seafloor (total depth of 2500 m below sea level) range 0.20 - 8.00 Ωm , which is expected for seafloor sediments (Key, 2003; Hoversten et al, 1998). Although the actual resistivity for silt and sandstone sedimentary units is on the order of 100 Ωm and higher (Table 1), the saturation of seawater (0.33 Ωm) significantly lowers the resistivity response of seafloor sediments.

SEDIMENT THICKNESS

Sediment thicknesses in the SDT have been measured using refraction and reflection seismic as well as towed gravity techniques. Shor et al. (1976) used the seismic refraction method to estimate a sediment thickness of 3 km across the SDT, Teng and Gorsline (1991) estimate the sediment thickness to be 2 km based on seismic reflection data, and Ridgway

and Zumberge (2002) concluded that the SDT has 3.4 km of sediments. These comparisons means that the sediment thickness estimate based on resistivity values of 0.5 – 5 Ωm is less than those based on seismic or gravity evidence. However, as there are several different units of sedimentary rocks underlying the seafloor of the San Diego Trough, it is reasonable that the contour below 8 Ωm may still include sedimentary units and not all sedimentary units have the same resistivity response. For example, the turbidity and hemipelagic units of Pliocene and Quaternary age should yield a different (lower) resistivity response than sedimentary volcanoclastic units of early-mid Miocene age.

USGS seismic line 112, which was acquired in 1990, shows the deepest part of the basin to be in the center, where the dextral strike-slip SDT fault offsets units laterally (Figure 37). The Pliocene and Quaternary sediments are flat-lying throughout most of the basin. Since these sediments are primarily turbidites and hemipelagics (Teng and Gorsline, 1991), they can be generally classified as sandstone and siltstone for the purposes of resistivity analysis. Below these flat-lying layers are the Miocene volcanoclastic and volcanic units which are mapped as being oriented both horizontally below the central part of the basin and at a western-dipping angle of $\sim 30^\circ$ in the eastern part of the basin, below the Coronado Bank.

The geoelectric structure that comes out of the inversions exhibits a patchiness and inconsistency of low resistivity pockets that is not expected. These pockets are in the very shallow subsurface, shaded in red on Figure 36. Some of the shallow resistivities are slightly less than that of seawater. Although this is unusual, it may be possible if there is any clay present or if there are topographic features on the seafloor which could cause unusually low conductivity responses. Alternatively, the inversion algorithm may have overfit the data in

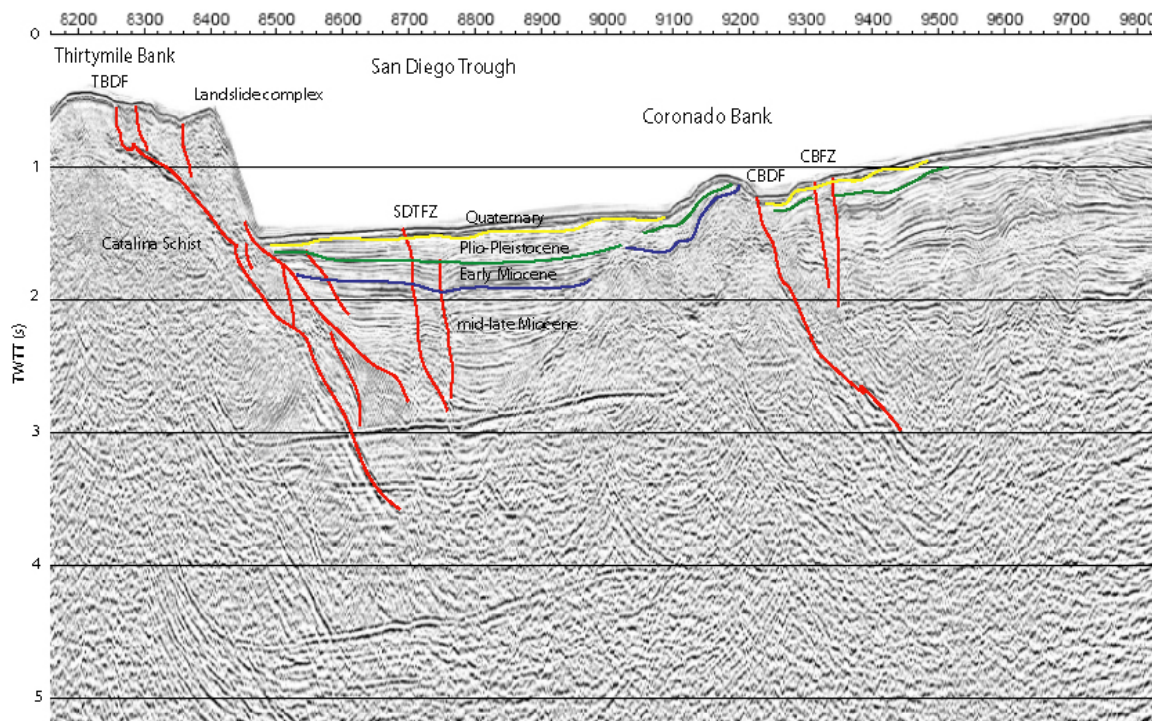


Figure 37. Seismic line USGS-112 with notable features identified. Interpretation of faults and unit identification based on Legg (2003). Location of seismic line is shown in Figure 5.

the short periods and permitted some very high conductive regions while lowering the overall fit to an optimal RMS value.

The resistivities of the shallow sediments in the center of the San Diego Trough are relatively low, in some cases even lower than the resistivity of seawater. As discussed in Chapter 3, the resistivity of seafloor sediments depends on porosity and on the pore-fluid resistivity, which is strongly influenced by temperature. High temperature and/or clay are two of several possible explanations for these highly conductive sediments in the shallow subsurface of the San Diego Trough.

CLAY EFFECTS

Clay can have a significant impact on resistivity measurements on land, but in the marine environment it has been shown (Wildenschild et al., 2000) that the main controlling factors are the salinity and pore water connectedness rather than the presence of clay. The CCB region has documented dredge samples of claystone rocks in some early Miocene strata samples (Vedder, 1987), but none of these confirmed samples were dredged from the San Diego Trough, nor from the bounding banks either side of the San Diego Trough.

However, a shallow seismic deep-tow survey in 1975 measured the acoustic attenuation of some clayey silt at the bottom of the San Diego trough to have a value of 0.36 db/m (Tyce, 1976). This is a relatively low value for attenuation and suggests that significant lithification may have occurred in these relatively young, high-porosity sediments. So while there are references to clay-like silts in the shallow subsurface of the SDT, it is the unconsolidated and high-porosities of the sediments as well as any anomalous heat flow measurements in the region that most likely contribute to the conductive response rather than the presence of clays.

HEAT FLOW, POROSITY AND TEMPERATURE

The highly conductive sediments may be explained by the anomalously high heat flow in the SDT. The geothermal gradient measured in the upper 6-8 m in the SDT region is approximately 120°C/ km for the basin (Lee and Henyey, 1975), with higher gradients found in some places within the Trough. Seama and Matsubayashi (2003) have estimated an empirical relation based on laboratory data between temperature (T) and conductivity (σ) at temperatures up to 300° C as

$$T = 0.34\sigma^2 + 4.2\sigma - 16. \quad (18)$$

Since the conductivity of seawater increases dramatically with temperature, temperatures of 100-300°C in the basin sediments would result in elevated conductivities (Figure 38). Using the measured thermal gradient to compute the pore-fluid conductivity with depth and applying it to calculations of sediment porosity using Archie's Law results in very high porosities in certain places along the SDT profile (Figure 39).

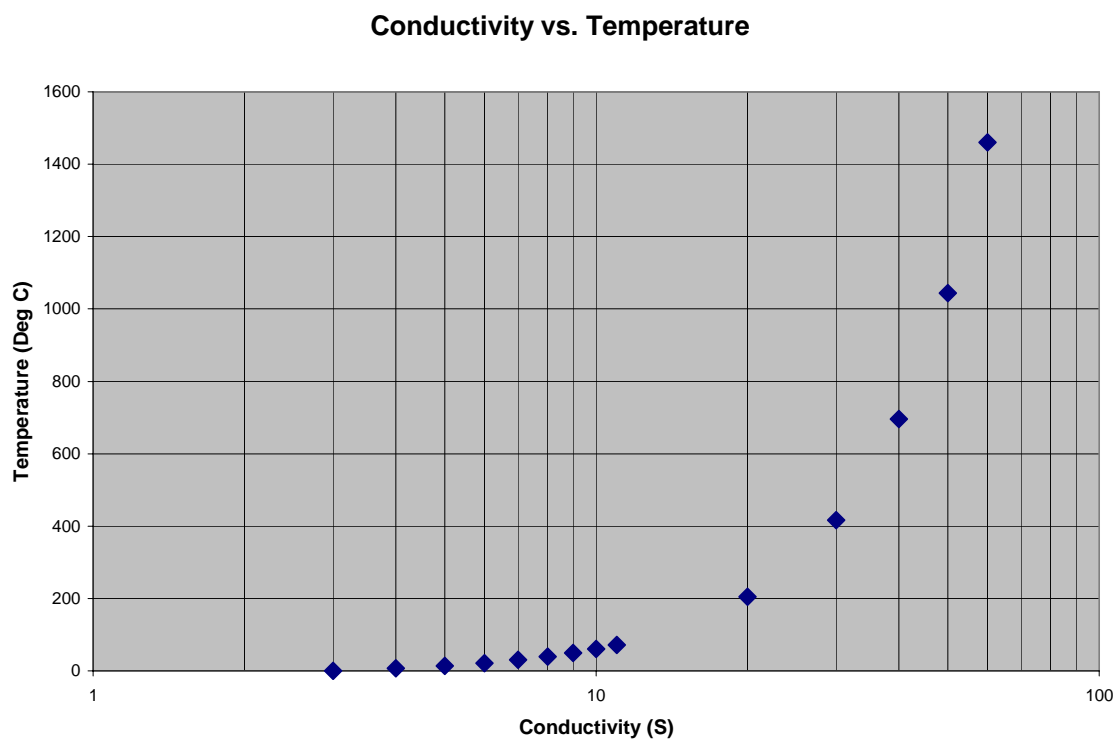


Figure 38. The variation of conductivity with increasing temperature, as calculated by Seama and Matsubayashi (2003).

Average porosity values for the SDT study area can be estimated from bulk density, using the gravity data provided by Ridgway and Zumberge (2002) (Figure 40, p. 76). One advantage of porosity inferred from density is that it does not depend on how the pore fluid is distributed, although we need to assume the density of the rock.

Other evidence for elevated temperatures through the region comes from geodynamic models for core-complex formation in the region (ten Brink et al., 2000). In their paper, ten

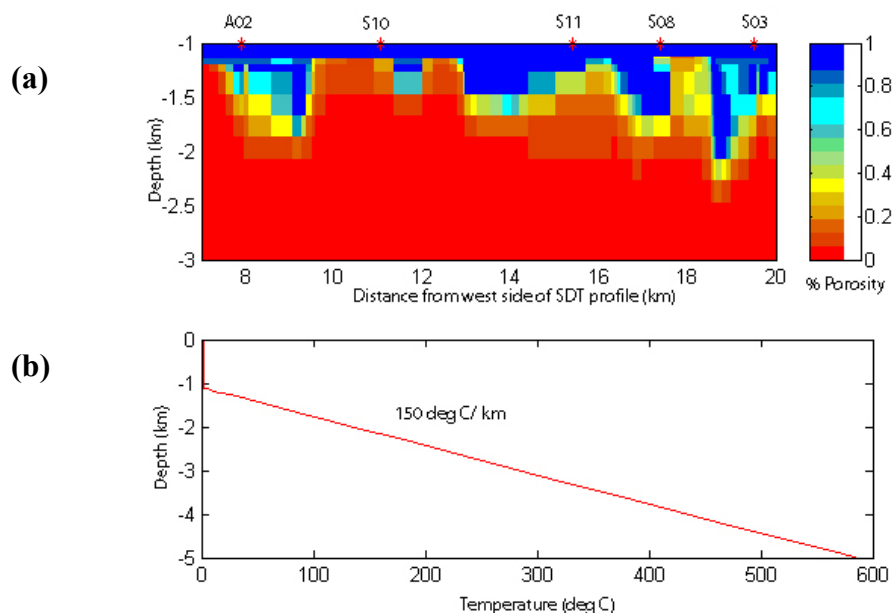


Figure 39. (a) Calculated pore-fluid conductivity with depth based on (b) a geothermal gradient of 150° C/ km.

Brink et al. document the initial thermal conditions prior to a rifting event and then calculate the present day geotherm. Their model predicts temperatures of 400° C at about 10 km depth and a lower thermal gradient than measured by the seafloor heat flow of Lee and Henyey. However, it is important to remember that while the sediments are likely cooled by thermal conduction and are likely to have a linear thermal gradient, the basement rocks likely have a component of advective cooling through hydrothermal circulation which will flatten the geotherm. Thus temperatures of around 300°C at the base of the sediments (at a depth of 3-4 km) are not unreasonable.

TURBIDITY CHANNELS

Porosity values from sedimentary rocks in the CCB region vary immensely, from 10.9% in Eocene sandstone (on San Nicholas Island) to over 30% in the friable, well-sorted sandstone unit of Oligocene age in the Cortes bank region (due west of the San Diego

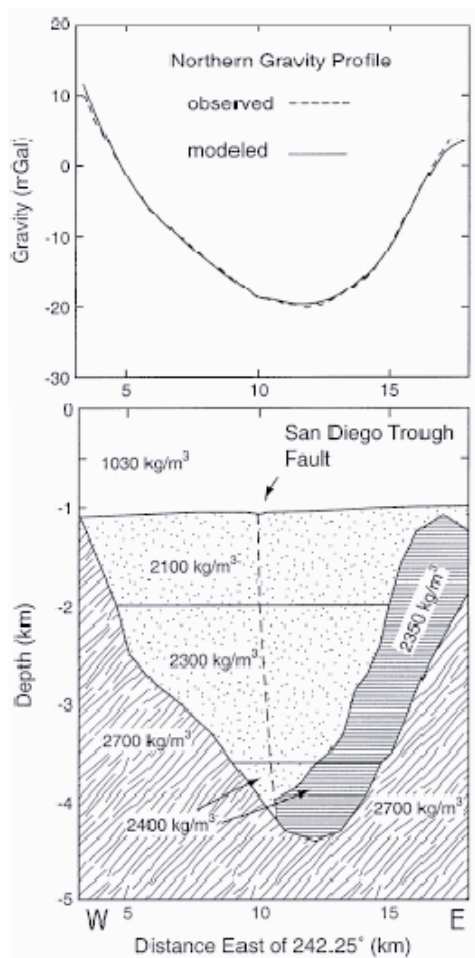


Figure 40. A 2-D gravity model of the towed gravity measurements across the San Diego Trough. The porosity values for the shallow sediments in the SDT study area are based on the top 1 km of structure (-1 to -2 km below sea level), which has a density of 2100 kg/m^3 . Source: Ridgway, J.R., and Zumberge, M.A., 2002, Deep-Towed Gravity Surveys in the Southern California Continental Borderland, *Geophysics*, 67, No. 3, p. 780.

Trough) (Vedder, 1987). The heat flow work that was done by Lee and Henyey (1975) refers to mapped turbidity current channels that run flow north to south parallel to strike in the San Diego Trough (Figure 41). According to Lee and Henyey (1975), the heat flow

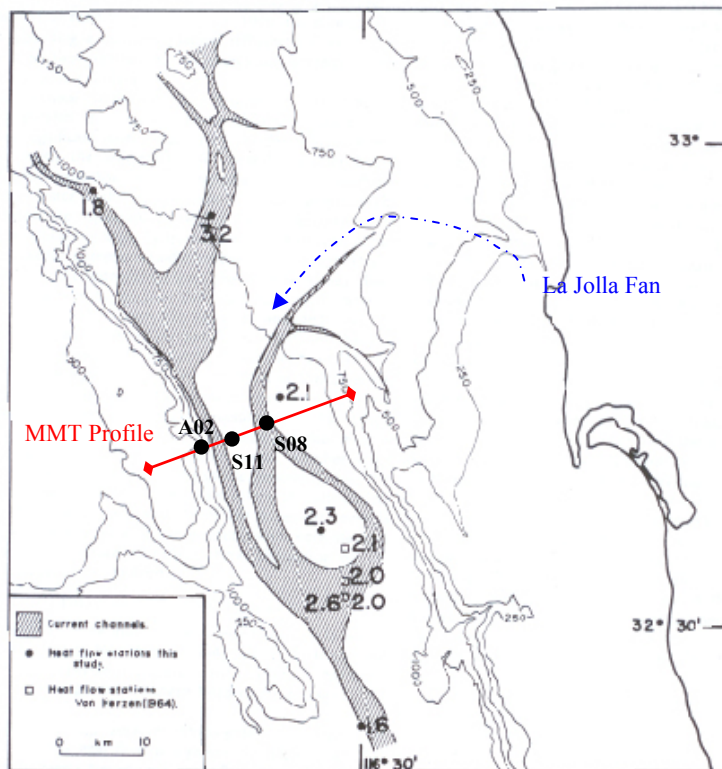


Figure 41. Heat flow distribution and turbidity current channels across the San Diego Trough. The turbidity current channels are marked in gray hashed areas; the closed circles are heat flow measurement values from Lee and Henyey; the open circles are from previous heat flow studies. The La Jolla Fan is annotated, as is the location of the MMT profile and the MMT sites that are closest to the channels.

Source: Lee, T., and Henyey, T.L., 1975, Heat flow through the southern California borderland: *J. Geophys. Res.*, 80, No. 26, p. 3738.

measurements that were taken in the center of the channels have anomalously high values, indicating rapid sedimentation and frequent flushing of the sea bottom by turbidity flows.

The turbidity channels weave along the strike of the basin, coming from the La Jolla fan in the north and flowing to deeper water towards the south. The locations of these channels coincide with proximity to the eastern flank of Thirtymile Bank (near site A02) and through the middle of the basin (near sites S11 and S08). Because turbidity flows seek out

the deepest parts of a basin, the location of the mapped channels may tell us something about the local shallow structure.

The deepest part of the San Diego Trough is on the eastern escarpment of Thirtymile Bank. This may be the surface expression of an active fault zone. Indeed, the seismic data from the 1986 Oceanside Fault was recently reprocessed (Astiz and Shearer, 2000) and the epicenters were found to be clustered at a depth of ~ 8 km directly along the fault plane of the Thirtymile Bank fault, though further to the north of the MMT study area. Similarly, the location of the San Diego Trough fault is mapped to trend directly through the middle of the basin. Close scrutiny of bathymetric maps reveals a linear surface depression that coincides with the seismically justified location of the SDT fault.

(2) Undulating Basal Boundary That Dips to the East

The resistivity responses abruptly transition from $\sim 50 \Omega\text{m}$ to $\sim 1000 \Omega\text{m}$ at a depth of 2 km (from sea level) on the west part of the basin beneath Thirtymile Bank (feature (2a) in Figure 36b). The transitional boundary slopes down to the east at an undulating but overall angle of approximately 30° up until the Coronado Bank where the transition disappears into a conductive region with average resistivity of $\sim 50 \Omega\text{m}$ (feature (2b) in Figure 36b). This boundary is more distinct in the TE mode than in the TM mode inversions, but the shape of this transition is the same.

The TE mode exhibits the above description with the resistive feature primarily residing on the western part of the profile. The boundary slopes down to the east as described above but there is a persistent conductive region in the western part of the basin. The abrupt transition from $50 \Omega\text{m}$ to $1000 \Omega\text{m}$ on the joint mode inversion is at a depth of ~ 2 km on the western part (sites S06 through S10) of the profile and ~ 5 km on the eastern

part (sites S11 through S03) of the profile. This resistive sloping boundary is most likely the response of the Catalina Schist which underlies the Miocene volcanoclastic sediments. As explained in Chapter 3, the expected resistivity of a metamorphic unit such as the Catalina Schist is on the order of 1000 - 10,000 Ωm . Furthermore, seismic evidence shows that the Catalina Schist basement shallows on the eastern flank of the Thirtymile Bank, and is overlain by only a veneer of Miocene volcanoclasts (Ridgway and Zumberge, 2002). The rise in resistivities between sites S07 and A02 are hypothesized to be due to the effect of a tilted block of volcanic rock that has slid down the surface of the Thirtymile Bank Fault and created 3-D effects on the seafloor as well as covered the in situ sediments in the local area.

One notable discontinuity in the shallow subsurface resistivity contours is the section between site S07 and A02, which is located just east of Thirtymile Bank (Figure 36). This 3 km-wide section (denoted as (2) in Figure 36) is a disruption to the basin fill sediments and shows evidence for a resistive body to approach the near surface. It is important to note that the presence of this discontinuity is primarily present in the TE mode but is robust enough to be a significant feature in the joint mode inversions.

A recent interpretation of seismic line USGS-112 shows a large tilted block of volcanic/volcanoclastic rocks that protrudes above the horizontal Pliocene sedimentary units on the eastern bank of Thirtymile Bank (Legg, personal communication, April 5, 2005). This tilted block is postulated to be formed by a submarine landslide. If the tilted block is composed of primarily volcanic rather than volcanoclastic rocks, this may explain why it appears that a resistive body approaches the near-surface, since volcanic rocks have a higher resistivity than sediment-based volcanoclastic rocks (Table 1). In addition to the postulated

landslide block, the local seafloor in this area may contain 3-D effects which have distorted the impedance tensor.

(3) Narrow Conductor in Eastern Part of the Basin

The TE mode and joint inversions require a conductive region (feature (3) on Figure 36) to reside in the eastern part of the basin, in the vicinity of the Coronado Bank. This requirement is robust enough to also be required in the joint mode inversions. The conductive region has a resistivity range of 5-50 Ωm and is situated from the surface down to a depth of about 30 km. The eastern flank of this feature has a steeper boundary than the western flank which has the 30° dipping conductive / resistive boundary. The core of the conductive region is a narrow zone of 20 Ωm resistivity values that comprise a zone 1 km wide.

The geographic location of this narrow conductive zone coincides with the approximate location of the Coronado Bank Fault Zone on the eastern flank of the Coronado Bank (Figure 36). This fault zone is well-characterized from earthquake seismic data, and is mapped to be the southern extension of the Oceanside Fault (Figure 42).

Conductive responses from the vicinity of a fault zone may indicate an active fault zone. Fluids migrating along an active fault zone would be responsible for the low resistivity in a linear pattern, similar to that observed by MT along active segments of the San Andreas Fault (e.g., Unsworth et al., 1997).

(4) Resistive Section Off the Profile to the East

Both TE and TM modes require a resistive section to exist off to the east of the study area at a depth of 3 – 25 km (feature (4) in Figure 36). The feature has a resistivity range of

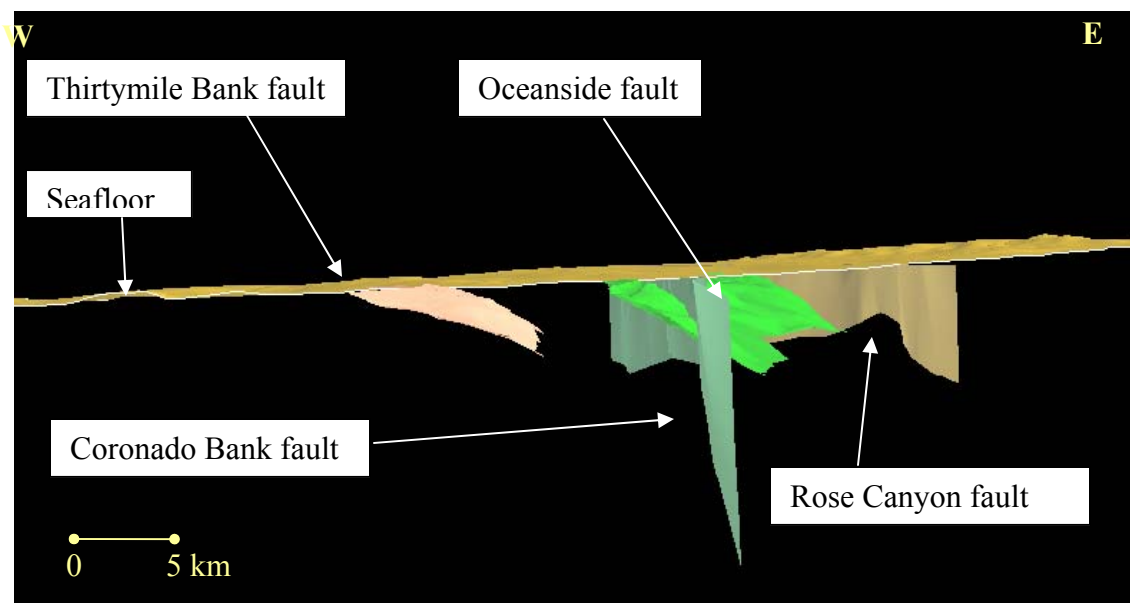


Figure 42. Fault plane geometries for the major faults in the San Diego Trough area, looking north (image is courtesy of Southern California Earthquake Center (SCEC)). No vertical exaggeration.

1000-5000 Ωm . The geographic location of this resistive body extends from the mainland to the east of the SDT study area. This feature is postulated to be the portion of continental crust east of the rift zone in ten Brink et al.'s model (ten Brink et al., 2000). This argument is further supported by previous land MT investigations (Hirasuna, 1995; Park et al., 1992) which measure the mainland southern California area in the vicinity of San Diego to have a relatively high resistivity signature ($\sim 1000 \Omega\text{m}$) compared to their offshore counterpart revealed during this investigation.

As shown in Plate 4 from ten Brink et al. (2000), the transition from oceanic crust to continental crust takes place somewhere in the vicinity of the ICB region (Figure 3). Although this schematic cross section is based on investigations that took place north of the SDT study area, the projected location of the SDT study area is essentially along strike to the south.

(5) Conductive Region Off the Profile to the West

Another feature of note is the conductive region (marked as (5) in Figure 36) in the west part of the section, off the profile and persistent in both the joint mode inversions as well as the TM only inversions. The conductive region is characterized by 20-50 Ωm responses. Although conductive anomalies off profile are common artifacts of inversions run in the *WinGLink* program, tests such as those described in Chapter 4 were run on this feature and found it to be required by the data.

The source of this conductive response is certainly related to the effects of seafloor bathymetry. As discussed in Chapter 3, any amount of seafloor bathymetry primarily affects the TM mode of data on the seafloor. Although a bathymetry model was factored into the *WinGLink* program for the region of the actual data profile, the effects of the bathymetry to the west of the profile were omitted. Therefore, the ocean depth at the western-most part of the profile, site S06, is at 375 m and this depth extends to the west through the end of the model space. However, this model does not properly simulate the seafloor bathymetry in this region. As Figure 2 shows, the regional bathymetry is rather complex. Therefore the source of this conductive response is probably that the conductive ocean is much deeper west of the San Diego Trough. The San Clemente Basin 50 km to the west has a maximum depth of 3500 m and the Patton Escarpment 240 km to the west marks the continental shelf break at a depth of 5000 m (Figure 2).

CHAPTER 6

CONCLUSIONS

The MMT study described in this thesis is the first of its kind conducted offshore California. The entire CCB region is known to be tectonically active. It is a major part of the complex boundary between the North American and Pacific plates. Within the CCB, the SDT region contains several anomalous geophysical phenomena, including a relatively high heat flow signature and several seismically identified faults. This MMT study provides yet another data set that can be used to help unravel the complex relationships present in the CCB.

The inversion results generated from the San Diego Trough MMT profile have perhaps raised more questions than provided answers, but the study is qualified by overall good quality data and thorough analysis. However, some of the most interesting geoelectric structures lies just outside the boundaries of the profile. And thus, further investigation is required to truly justify the interpretation of inversion features that are outside the station limits of the SDT MMT profile. Some persistent features of these data may shed insight into previous work that has been done in the CCB region and may also lead to more focused geophysical investigations offshore southern California in the future.

The five persistent features that revealed by this investigation are:

1. A region of high conductivity ($0.25 - 10 \Omega\text{m}$) in the top 1-2 km below the seafloor, consistent with the presence of largely unconsolidated sediments.
2. An undulating basal boundary to the conductive part of the basin that shallows on the west end to less than 1 km and slopes eastward at approximately $30^\circ - 40^\circ$ to a depth of about 5 km.

3. A narrow region of conductive zones (10-50 Ωm) that are present from the surface down to 30 km in the eastern half of the basin, coincident with the Coronado Bank fault zone.
4. A resistive section off to the east of the profile that is present from the surface down to 50 km.
5. A conductive section off to the west of the profile that is present from the surface down to 50 km.

ACTIVE FAULTING

The SDT area contains three significant faults: Thirtymile Bank fault, San Diego Trough fault and the Coronado Bank fault zone. The presence of a vertical zone of high electrical conductivity along the Coronado Bank fault zone suggests that this fault zone is active. This conclusion is supported by the association of a vertical, highly conductive zone coincident with active portions of the San Andreas fault in California (e.g., Unsworth et al., 1997; Unsworth and Bedrosian, 2004). The presence of a highly resistive section immediately east of this fault zone suggests that it marks the boundary between the Catalina terrane and the Santa Ana terrane. As discussed in Chapter 2, this terrane boundary has been drawn in several places near the vicinity of the San Diego Trough and is known to separate the Catalina Schist basement from the plutonic basement of the Santa Ana batholith.

The Thirtymile Bank fault exhibits strong evidence for landslides and slumping, thought to be the result of Miocene volcanic rocks lying directly over the Catalina Schist detachment surface. Although at one time this fault was certainly active, it does not contain a conductive signature to indicate that it is active in the same way as the Coronado Bank fault zone. However, the 3-D seafloor topographic effects of volcanic blocks that have slid may have influenced the magnetotelluric inversion results in this area.

The San Diego Trough fault offsets recent Pliocene and Pleistocene sediments, and may be active as a strike-slip fault as well, but there is no MT evidence for an anomalously conductive signature. However, the lack of MT evidence does not necessarily imply that the fault is not active (e.g., Mackie et al., 1997; Unsworth et al., 1999) – it may be locked or a conductive zone may be too narrow for detection with the site spacing utilized in this survey.

SIMILARITIES TO THE SAN ANDREAS FAULT

The correlation between conductive features in MT analysis and the character of fault activity is thoroughly investigated in California in terms of “creeping” vs. “locked” fault segments (e.g., Unsworth et al., 1997; Bedrosian et al., 2002). The conductive zones that have been observed at creeping segments of the San Andreas fault are thought to be caused by the presence of low resistivity fluids that reside in the fault zone. These fluids may have entered the zone between earthquake episodes or the fluids may have migrated into the zone from nearby crustal aquifers. The MT method is highly sensitive to the presence of connected fluids. Attempting to image a narrow, vertical conductive zone may be simply imaging the network of connected fluid-filled cracks that are maintained by the motion of the creeping fault, as suggested by Unsworth and Bedrosian (2004).

The state of activity along the major faults in the SDT area can be estimated based on the MT signatures discovered in the present survey. It appears that the Coronado Bank fault zone is the most active and possibly exhibits the same “creeping” behavior that the San Andreas fault is in the Parkfield area (Bedrosian et al., 2002). The Thirtymile Bank fault was active in the recent past, at least in terms of providing a surface for overlying volcanic blocks to slide down but no conductive anomalies were detected. The San Diego Trough fault is thought to be presently active based on reflection seismic data, but there is no

magnetotelluric evidence for this, suggesting that the fault is either locked or the resolution of this MMT study was too broad.

REFERENCES

- Archie, G.E., 1942, The electrical resistivity log as an aid in determining some reservoir characteristics: *J. Pet. Technol.*, **5**, 1-8.
- Astiz, L., and Shearer, P.M., 2000, Earthquake location in the Inner Continental Borderland, offshore southern California: *Seismological Society of American Bulletin*, **90**, 425-449.
- Atwater, T., and Stock, J., 1998, Pacific-North America plate tectonics of the Neogene southwestern United States: An update: *Int. Geol. Rev.*, **40**, 375-402.
- Baba, K., and Chave, A.D., 2004, Correction of seafloor magnetotelluric data for topographic effects during inversion: *J. Geophys. Res.*, submitted.
- Baba, K., and Seama, N., 2002, A new technique for the incorporation of seafloor topography in electromagnetic modeling: *Geophys. J. Int.*, **150**, 392-402.
- Bedrosian, P.A., Unsworth, M.J., and Egbert, G.D., 2002, Magnetotelluric imaging of the creeping segment of the San Andreas Fault near Hollister: *Geophys. Res. Lett.*, **29**, 1506.
- Bedrosian, P.A., Unsworth, M.J., Egbert, G.D., and Thurber, C.H., 2004, Geophysical images of the creeping segment of the San Andreas Fault near Hollister: Implications for the role of crustal fluids in the earthquake process: *Tectonophysics*, **385**.
- Bohannon, R.G., and Geist, E., 1998, Upper crustal structure and Neogene tectonic development of the California continental borderland: *Bull. Geol. Soc. Am.*, **188**, 779-800.
- Cagniard, L., 1953, Basic theory of the magnetotelluric method of geophysical prospecting: *Geophysics*, **18**, 605-635.
- Cann, L., 1985, Slide-mudflow Fishermans Cove area, Santa Catalina Island, *in* Gath, E.M., and Bottoms, M.M., Eds., *Geology of Santa Catalina Island: South Coast Geological Society*, 73-81.
- Chave, A.D., and Smith, J.T., 1994, On electric and magnetic galvanic distortion tensor decompositions: *J. Geophys. Res.*, **99** (B3), 4669-4682.
- Chave, A.D., and Thomson, D.J., 2003, A bounded influence regression estimator based on the statistics of the hat matrix: *J. Roy. Stat. Soc., Series C (Appl. Statist.)*, **52**, 307-322.

- Constable, S., and Constable, C. 2004, Satellite magnetic field measurements: Applications in studying the deep Earth, *in* Sparks, R.S.J., and Hawkesworth, C.T., Eds., State of the planet: Frontiers and challenges in geophysics: Am. Geophys. Union, Geophys. Mono. **150**, 147-159.
- Constable, S. C., Orange, A., Hoversten, G. M., and Morrison, H. F., 1998, Marine magnetotellurics for petroleum exploration, Part 1: A sea-floor equipment system: Geophysics, **63**, 816–825.
- Constable, S.C., Parker, R.L., and Constable, C.G., 1987, Occam's inversion: A practical algorithm for generating smooth models from electromagnetic sounding data: Geophysics, **52**, No. 3, 289-300.
- Constable, S.C., Shankland, T.J., and Duba, A., 1992, The electrical conductivity of an isotropic olivine mantle: J. Geophys. Res., **97**(B3), 3397-3404.
- Crouch, J.K. and Suppe, J., 1993, Late Cenozoic tectonic evolution of the Los Angeles basin and inner California borderland: A model for core complex-like crustal extension: Bull. Geol. Soc. Am., **105**, 1415-1434.
- de Groot-Hedlin, C., and Constable, S., 2004, Inversion of magnetotelluric data for 2-D structure with sharp resistivity contrasts: Geophysics, **69**, No. 1, 78-86.
- Evans, R.L., 1994, Constraints on the large scale porosity of young oceanic crust from seismic and resistivity data: Geophys. J. Int., **119**, 869-879.
- Evans R.L., and Everett, M. E., 1992, Magnetotellurics and Mid-Ocean Ridge Melt Transport: A 2-D Perspective, *in* Morgan, J.P., Blackman, D., and Sinton, J., Eds., Mantle flow and melt generation at mid-ocean ridges: Am. Geophys. Union, Geophys. Mono. **71**, 353-361.
- Filloux, J.H., 1987, Instrumentation and experimental methods for oceanic studies, *in* Jacobs, J., ed., Geomagnetism: Academic Press, 143-248.
- Groom, R.W., and Bailey, R.C., 1989, Decomposition of magnetotelluric impedance tensors in the presence of local three-dimensional galvanic distortion: J. Geophys. Res., **94**, No. B2, 1913-1925.
- Grove, M., and Bebout, G.E., 1995, Cretaceous tectonic evolution of coastal southern California: Insights from the Catalina Schist: Tectonics, **14**, No. 5, 1290-1308.
- Hashin, Z., and S. Shtrikman, 1962, A variational approach to the theory of effective magnetic permeability of multiphase materials: J. Appl. Phys., **33**, 3125-3131.
- Hauksson, E., and Jones, L., 1988, The July 1986 Oceanside (M_L = 5.3) earthquake sequence in the Continental Borderland, southern California: Seismological Society of America Bulletin, **78**, 1885-1906.

- Heinson, G., and S. Constable, 1992, The electrical conductivity of the oceanic upper mantle: *Geophys. J. Int.*, **110**, 159-179.
- Hirasuna, B.K., 1995, Correction of magnetotelluric data influenced by static shift in a batholithic terrane, northern Peninsular Ranges, California: M.Sc. thesis, Univ. of Cal., Riverside.
- Hoehn, G.L., and Warner, B.N., 1960, Magnetotelluric measurements in the Gulf of Mexico at 20 m ocean depths, in *Handbook of geophysical exploration at sea*: CRC, 397-416.
- Hoversten, G.M, Constable, S.C., and Morrison, H.F., 2000, Marine magnetotellurics for base-of-salt mapping: Gulf of Mexico field test at the Gemini structure: *Geophysics*, **65**, 1476-1488.
- Hoversten, G. M., Morrison, H.F., and Constable, S., 1998, Marine Magnetotellurics for petroleum exploration part 2: Numerical analysis of subsalt resolution: *Geophysics*, **63**, 826-840.
- Howell, D.G., and Vedder, J., 1981, Structural implications of stratigraphic discontinuities across the Southern California borderland, *in* Ernst, W.G. and Rubey, I., Eds., *The geotectonic development of California*: Prentice Hall, 535-538.
- Jackson, P.D., Taylor-Smith, D., and Stanford, P.N., 1978, Resistivity-porosity-particle shape relationships for marine sands: *Geophysics*, **43**, 1250-1268.
- Jegen, M.D., and Edwards, R.N., in press, On the physics of marine magnetotelluric sounding.
- Jiracek, G.R., 1990, Near-surface and topographic distortions in electromagnetic induction: *Surveys in Geophysics*, **11**, 163-203.
- Jiracek, G.R., Haak, V., and Olsen, K.H., 1995, Practical magnetotellurics in continental rift environments, *in* Olsen, K.H., Ed., *Continental rifts: evolution, structure and tectonics*: Elsevier, 103-129.
- Jones, A.G., Chave, A.D., Egbert, G., Auld, D. and Karsten, B., 1989, A comparison of techniques for magnetotelluric response function estimation: *J. Geophys. Res.*, **94**, No. 10, 14,201-14,213.
- Jones, A.G., and Groom, R.W., 1993, Strike-angle determination from the magnetotelluric impedance tensor in the presence of noise and local distortion: rotate at your peril!: *Geophys. J. Int.*, **113**, 524-534.
- Karato, S., 1990, The role of hydrogen in the electrical conductivity of the upper mantle: *Nature*, **347**, 272-273.

- Kennedy, M.P., Clarke, S.H., Greene, H.G., and Legg, M.R., 1980, Recency and character of faulting offshore metropolitan San Diego, California: Cal. Div. of Min. and Geol., Map Sheet 42, Scale 1: 50,000.
- Key, K. W., 2003, Application of broadband marine magnetotelluric exploration to a 3D salt structure and a fast-spreading ridge, Ph.D. dissertation, Univ. of Cal., San Diego.
- Lee, T., and Henyey, T.L., 1975, Heat flow through the southern California borderland: J. Geophys. Res., **80**, No. 26, 3733-3743.
- Legg, M.R., 1985, Geologic structure and tectonics of the inner continental borderland offshore northern Baja California, Mexico, Ph.D. dissertation, Univ. of Cal., Santa Barbara.
- Legg, M.R., and Kamerling, M.J., 2003, Large-scale basement-involved landslides, California Continental Borderland: Pure and Applied Geophysics, **160**, 2033-2051.
- Legg, M.R., and Kennedy, M.P., 1991, Oblique divergence and convergence in the California continental borderland, *in* Abbott, P.L., and Elliott, W.J., Eds., Environmental perils of the San Diego region: San Diego Association of Geologists, 1-16.
- Legg, M., Nicholson, C., and Sorlien, C., 1992, Active faulting and tectonics of the Inner California Continental Borderland: USGS lines 114 and 112: Eos (Trans., American Geophysical Union), **73**, 588.
- Legg, M.R., C. Nicholson, C. Goldfinger, R. Milstein and M.J. Kamerling, 2004, Large enigmatic crater structures offshore southern California: Geophys. J. Int, **159**, 803-815.
- Luyendyk, B.P., 1991, A model for Neogene crustal rotations, transtension, and transpression in southern California: Geol. Soc. Am. Bull., **103**, 1528-1536.
- Luyendyk, B.P., M.J. Kamerling, and R.R. Terres, 1980, Geometric model for Neogene crustal rotations in southern California: Geol. Soc. Am. Bull., **91**, 211-217.
- Mackie, R.L., Livelybrooks, D.W., Madden, T.R., Larsen, J.C., 1997, A magnetotelluric investigation of the San Andreas fault at Carrizo Plain, California: Geophys. Res. Lett., **24**, 1847-1850.
- Mann, P., and Gordon, M.B., 1996, Tectonic uplift and exhumation of blueschist belts along transpressional strike-slip fault zones, *in* Bebout, G.E., Scholl, D.W., Kirby, S.H., and Platt, J.P., Eds., Subduction: Top to bottom: Am. Geophys. Union, Geophys. Monogr. Ser. **96**, 143-154.
- McNiece, G.W., and Jones, A.G., 2001, Multisite, multifrequency tensor decomposition of magnetotelluric data: Geophysics, **66**, No. 1, 158-173.

- Moore, D.G., 1969, Reflection profiling studies of the California continental borderland; Structure and Quaternary turbide basins: Geol. Soc. Am. Special Paper, **107**.
- Nicholson, C., Sorlien, C., Atwater, T., Crowell, J.C., and Luyendyk, B.P., 1994, Microplate capture, rotation of the western Transverse Ranges, and initiation of the San Andreas transform as a low-angle fault system: *Geology*, **22**, 491-495.
- Nicholson, C., Sorlien, C., and Legg, M., 1993, Crustal imaging and extreme Miocene extension of the Inner California Continental Borderland: Geological Society of America Abstracts with Programs, **25**, No. 6, A-418.
- Nolasco, R., Tarits, P., Filloux, J.H., and Chave, A.D., 1998, Magnetotelluric imaging of the Society Islands hotspot: *J. Geophys. Res.*, **103**, No. B12, 30, 287-309.
- Orange, A.S., 1989, Magnetotelluric exploration for hydrocarbons: *Proceedings of the IEEE*, **77**, No. 2, 287-317.
- Pacheco, J., and Nabelek, J., 1988, Source mechanisms of three moderate California earthquakes of July, 1986: *Bull. Seismol. Soc. Am.*, **78**, 1907-1929.
- Park, S.K., Jiracek, G.R., and Johnson, K.M., 1992, Magnetotelluric evidence for a brittle-ductile transition, Peninsular Ranges Batholith, southern California?: *Geophys. Res. Letters*, **19**, 1242-1250.
- Parker, R.L., and Booker, J.R., 1996, Optimal one-dimensional inversion and bounding of magnetotelluric apparent resistivity and phase measurements: *Phys. Earth Planet. Int.*, **98**, 269-282.
- Pellerin, L., and Hohmann, G.W., 1990, Transient electromagnetic inversion: A remedy for magnetotelluric static shifts: *Geophysics*, **55**, 1242-1250.
- Platt, J.P., 1975, Metamorphic and deformational processes in the Franciscan Complex, California: Some insights from the Catalina schist terrane: *Geol. Soc. Am. Bull.*, **86**, 1337-1347.
- Ridgway, J.R., 1997, The development of a deep-towed gravity meter, and its use in marine geophysical surveys of offshore southern California, and an airborne laser altimeter survey of Long Valley, California: Ph.D. dissertation, Univ. of Cal., San Diego.
- Ridgway, J.R., and Zumberge, M.A., 2002, Deep-towed gravity surveys in the southern California continental borderland, *Geophysics*, **67**, No. 3, 777-787.
- Rivero, C., Shaw, J.H., and Mueller, K., 2000, Oceanside and Thirtymile Bank blind thrusts: Implications for earthquake hazards in coastal southern California: *Geology*, **28**, No. 10, 891-894.
- Rodi, W., and Mackie, R.L., 2001, Nonlinear conjugate gradients algorithm for 2-D magnetotelluric inversion: *Geophysics*, **66**, No. 1, 174-187.

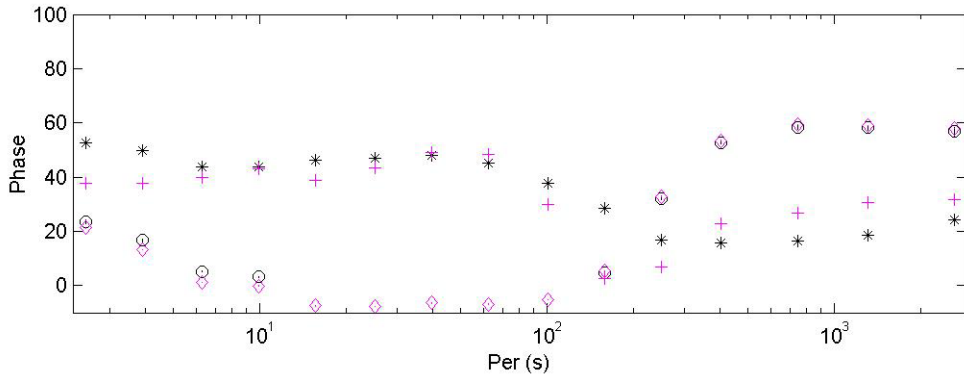
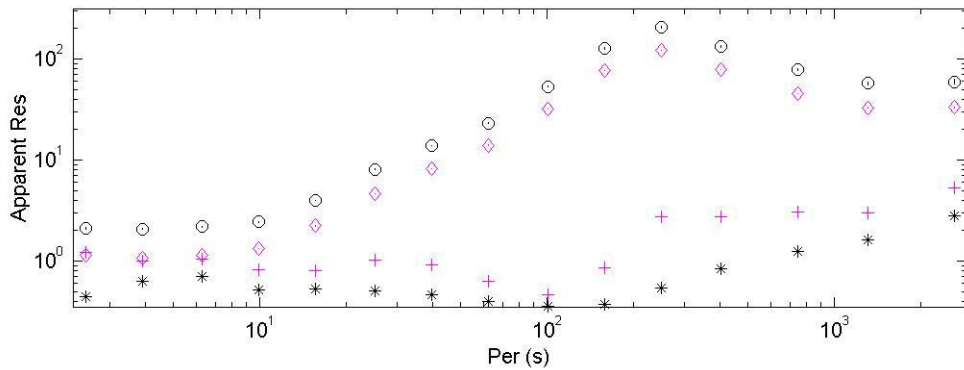
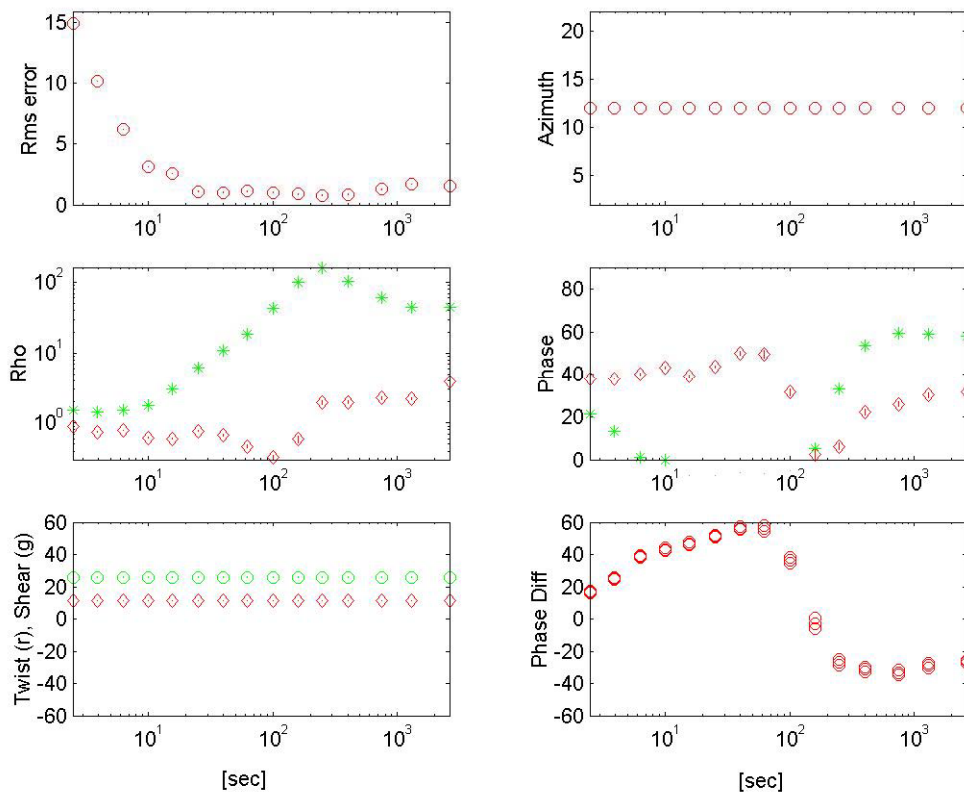
- Schmeling, H., 1986, Numerical models on the influence of partial melt on elastic, anelastic, and electrical properties of rocks Part II: Electrical conductivity: *Phys. E. Pl. Int.*, **43**, 123-136.
- Schwalenberg, K., and Edwards, R.N., 2004, The effects of seafloor topography on magnetotelluric fields: An analytical formulation confirmed with numerical results: *Geophys. J. Int.*, **159**, 607-621.
- Seama, N., and Matsubayashi, S., 2003, Recent progress in technology for marine geophysical research: *J. Japan Soc. Mar. Surv. Tech.*, **15**, 71-87.
- Shor, G.G., Jr., Raitt, R.W., and McGowan, D.D., 1976, Seismic refraction studies in the southern California borderland, 1949-1974: *Scripps Inst. Ocean. Ref.* **76-13**.
- Sorensen, S.S., Bebout, G.E., and Barton, M.D., 1991, A field guide to the geology, petrology, and geochemistry of the Catalina Schist on Santa Catalina Island: Evidence for fluid-rock interaction, thermal evolution, and metasomatic alteration in a paleosubduction zone, *in* Walawender, M.J., and Hanan, B.B., Eds., *Geological excursions in Southern California and Mexico: Geol. Soc. Am. Annual Meeting Guidebook*, 272-296.
- Sorlien, C., Nicholson, C., and Luyendyk, B., 1993, Miocene collapse of the California continental margin: *Geological Society of America Abstracts with Programs*, **25**, No. 6, A-311.
- ten Brink, U.S., Zhang, I., Brocher, T.M., Okaya, D.A., Klimgard, K.D. and Fuis, G.S., 2000, Geophysical evidence for the evolution of the California inner continental borderland as a metamorphic core complex: *J. Geophys. Res.*, **105**, 5835-5857.
- Teng, L.S., and Gorsline, D.S., 1991, Stratigraphic framework of the continental borderland basins, southern California: *in* Dauplin, J.P., and Simone, B.R.T., Eds., *The gulf and peninsular province of the Californias*, **47**: *Am. Assn. Petr. Geol.*, 127-143.
- Tikhonov, A.N., 1950, Determination of the electrical characteristics of the deep strata of the earth's crust: *Dok. Acad. Nauk., USSR*, **73**, No. 2, 295-297.

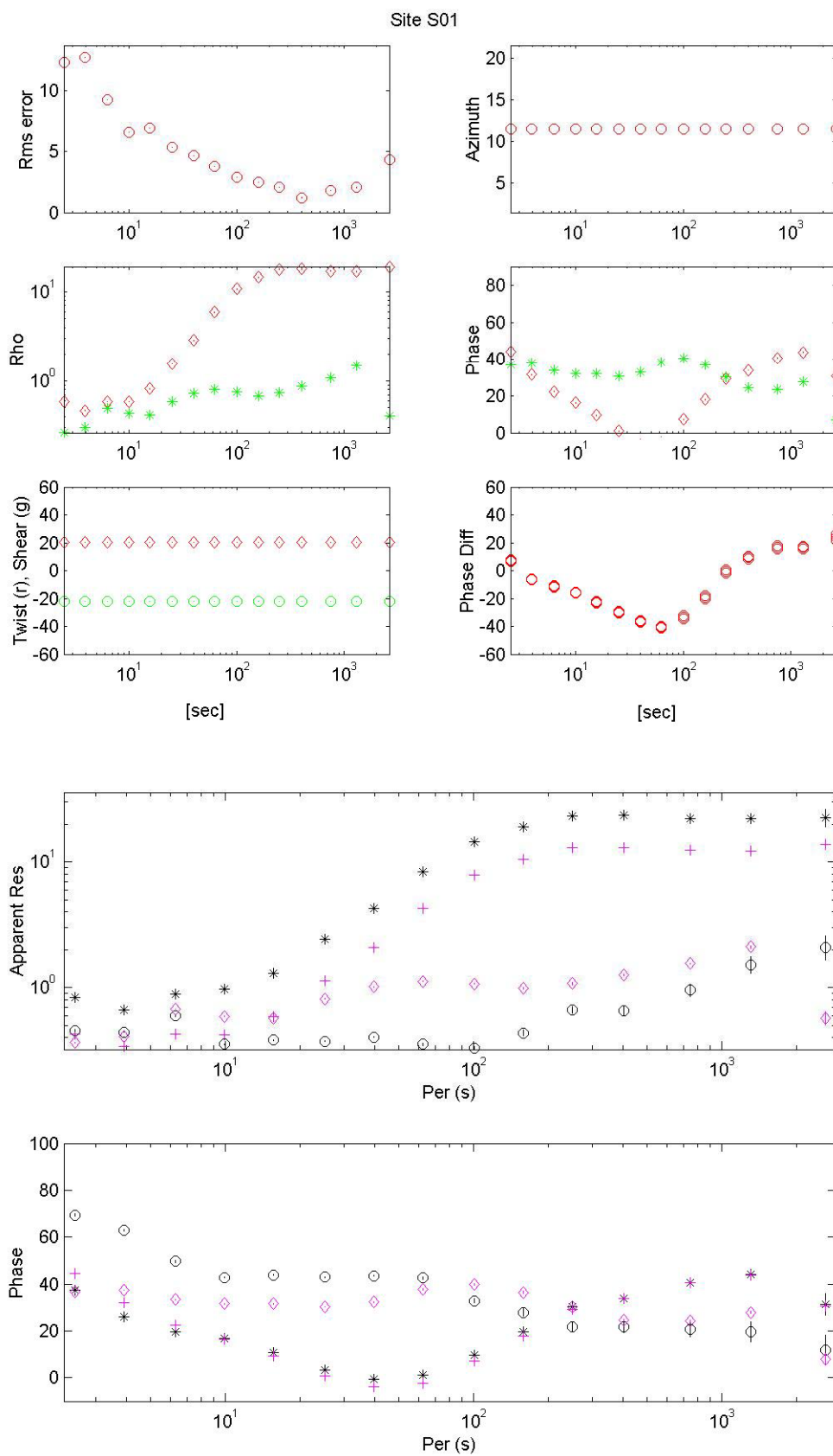
- Tyce, R.C., 1976, Near-bottom observations of 4 kHz acoustic reflectivity and attenuation: *Geophysics*, **41**, No. 4, 673-699.
- Unsworth, M.J., Egbert, G.D., and Booker, J.R., 1999, High resolution electromagnetic imaging of the San Andreas fault in Central California: *J. Geophys. Res.*, **104**, 1131-1150.
- Unsworth, M.J., Malin, P., Egbert, G.D., and Booker, J.R., 1997, Internal structure of the San Andreas fault at Parkfield, California: *Geology*, **25**, 359-362.
- Unsworth, M.J., and Bedrosian, P.A., 2004, On the geoelectric structure of major strike-slip faults and shear zones: *Earth Planets Space*, **56**, 1177-1184.
- Vedder, J.G., 1987, Regional geology and petroleum potential of the southern California borderland, *in* Scholl, D.W., Grantz, A. and Vedder, J.G., Eds., *Geology and resource potential of the continental margin of western North America and adjacent ocean basins – Beaufort Sea to Baja California*, Vol. 6: Circum-Pacific Council for Energy and Mineral Resources, 403-447.
- Vedder, J.G., 1990, Maps of California Continental Borderland showing compositions and ages of bottom samples acquired between 1968 and 1979, *Miscellaneous Field Studies Map MF-2122*, scale 1:250,000, U.S. Geological Survey, sheets 1-3.
- Vedder, J.G., Beyer, L.A., Junger, A., Moore, G.W., Roberts, A.E., Taylor, J.C., and Wagner, H.C., 1974, Preliminary report on the geology of the Continental Borderland of southern California: U.S. Geological Survey, *Miscellaneous Field Studies Map MF-624*, Scale 1:500,000.
- Wannamaker, P.E., Booker, J.R., Filloux, J.H., Jones, A.G., Jiracek, G.R., Chave, A.D., Tarits, P., Waff, H.S., Egbert, G.D., Young, C.T., Stodt, J.A., Martinez, G.M., Law, L.K., Yukutake, T., Segawa, J.S., Ehite, A., and Green, A.W., 1989, Subduction system in the EMSLAB project: *J. Geophys. Res.*, **94**, No. B10, 14,111-14,125.
- Ward, S.H., 1990, Resistivity and induced polarization methods, *in* Ward, S.H., Ed., *Geotechnical and environmental geophysics*, Vol. 1: Society of Exploration Geophysicists, 147-189.
- Ward, S.H., and G.W. Hohmann, 1988, Electromagnetic theory for geophysical applications: *in* Nabighian, M.N., Ed., *Electromagnetic methods in applied geophysics*, Vol. 1: Society of Exploration Geophysics, 131-311.
- Wiegand, P.W., 1994, Timing and cause of Middle Tertiary magmatism in onshore and offshore southern California: *AAPG Bull.*, **78**, 676.
- Wildenschild, D., Roberts, J.J., and Carlberg, E.D., 2000, On the relationship between microstructure and the electrical and hydraulic properties of sand-clay mixtures: *Geophys. Res. Letts.*, **27**, 3085-3088.

Xu, Y.S., Shankland, T.J., and Duba, A.G., 2000, Pressure effect on electrical conductivity of mantle olivine: *Phys. E. Pl. Int.*, **118**, 149-161.

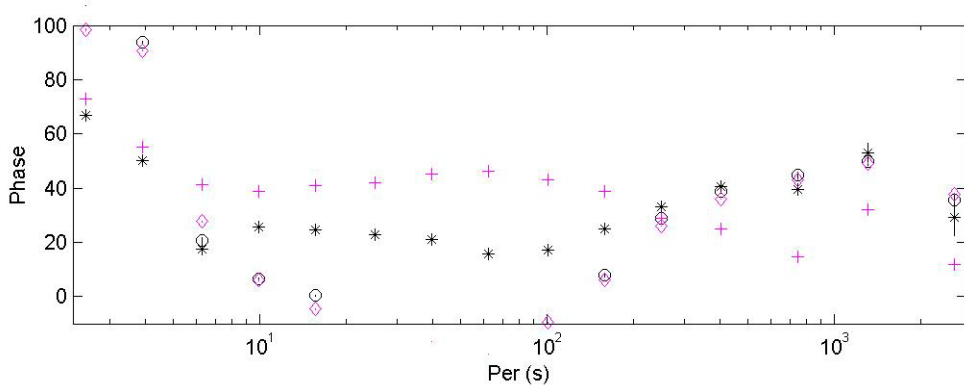
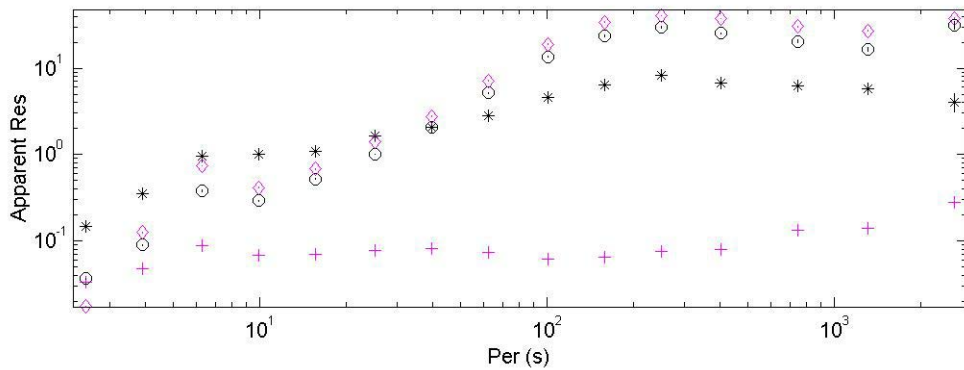
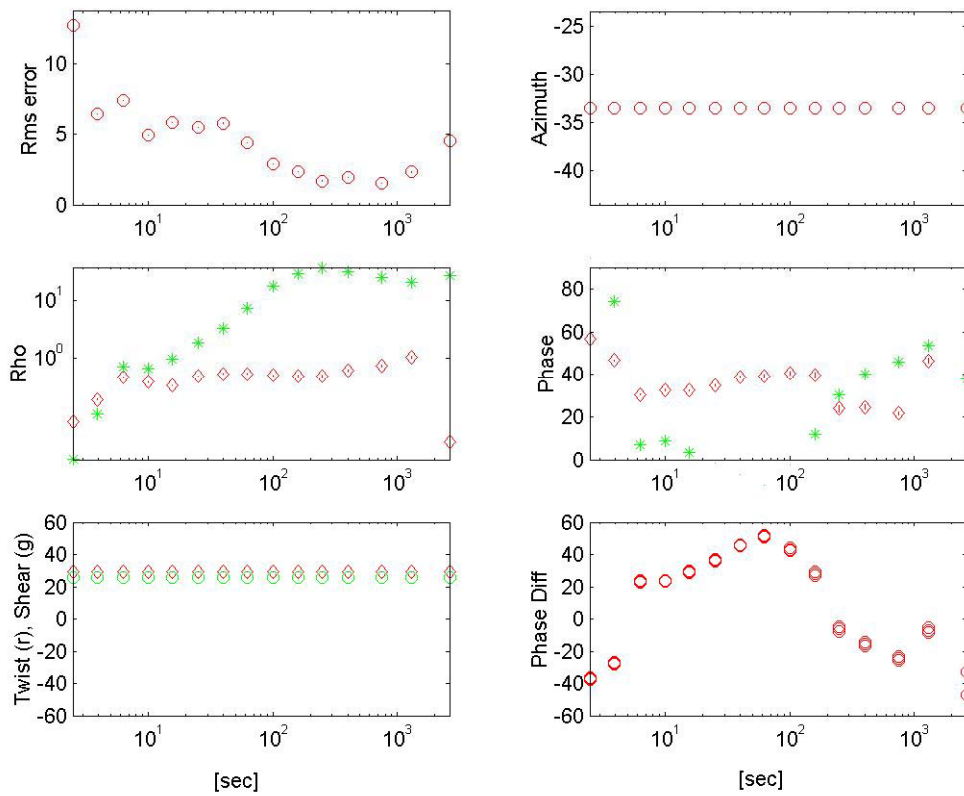
APPENDIX A**GROOM-BAILEY DECOMPOSITION**

Site A02

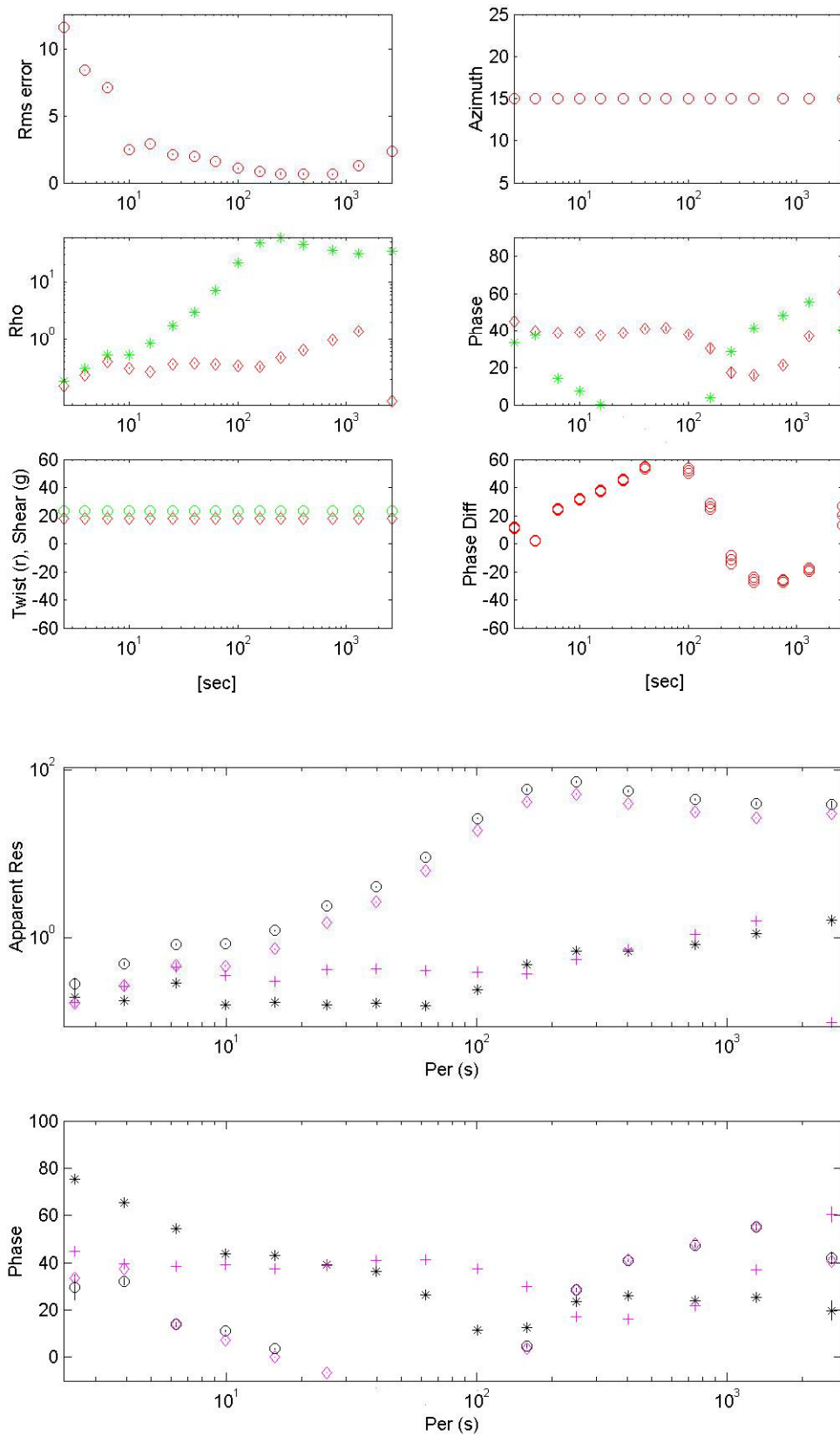




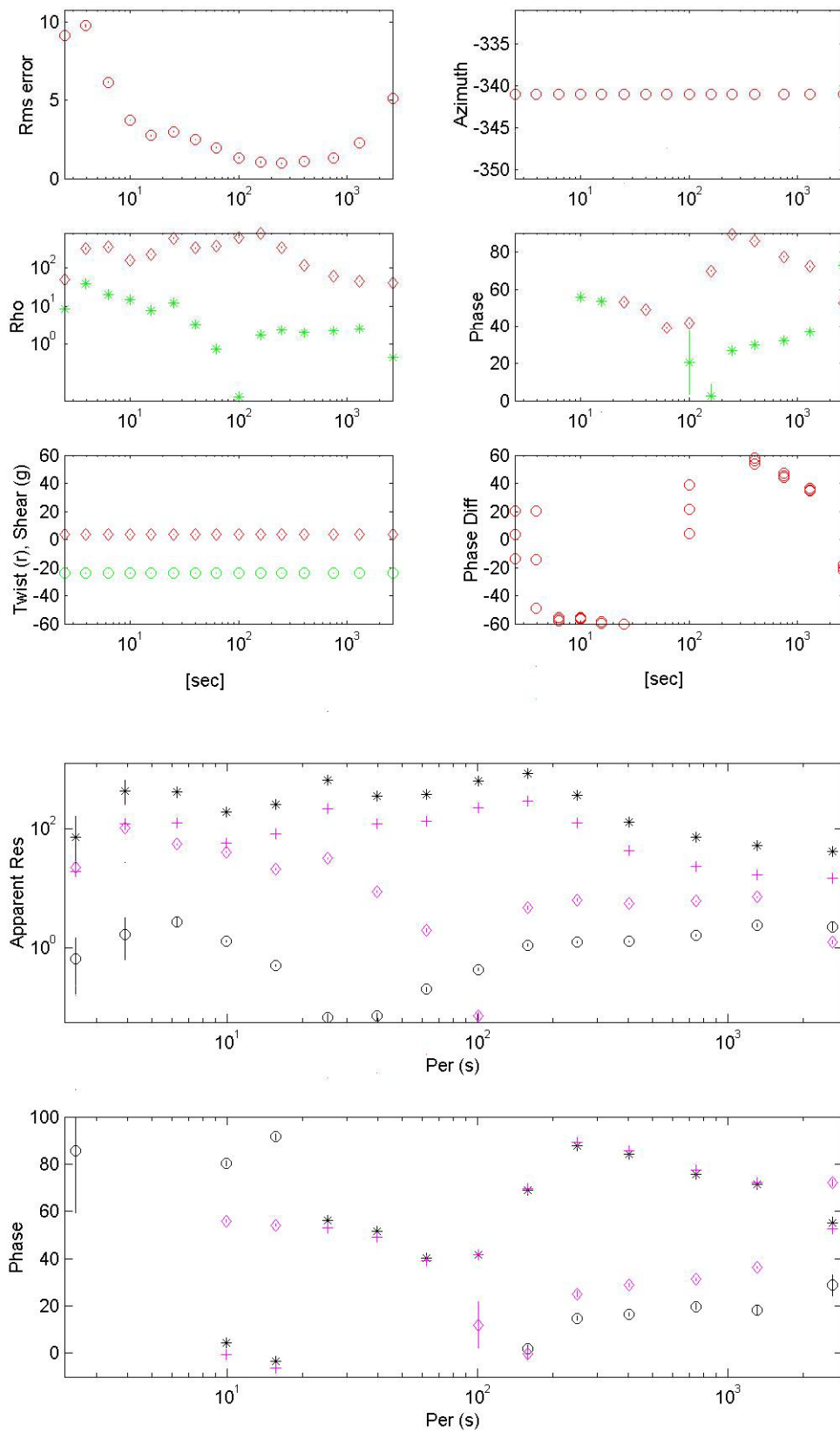
Site S02



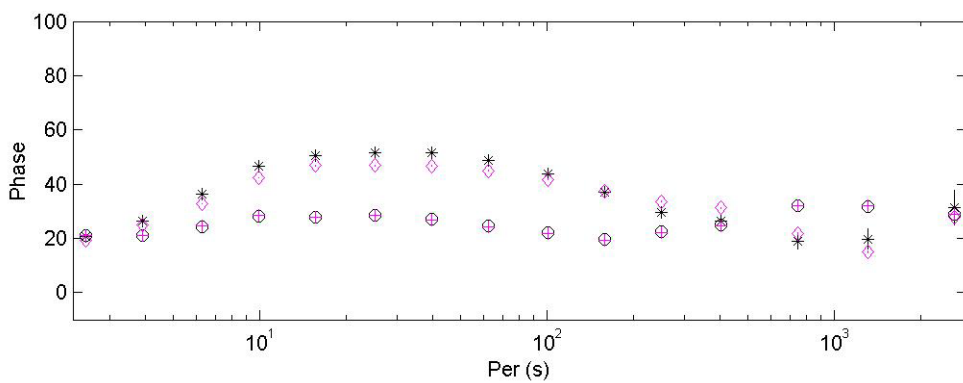
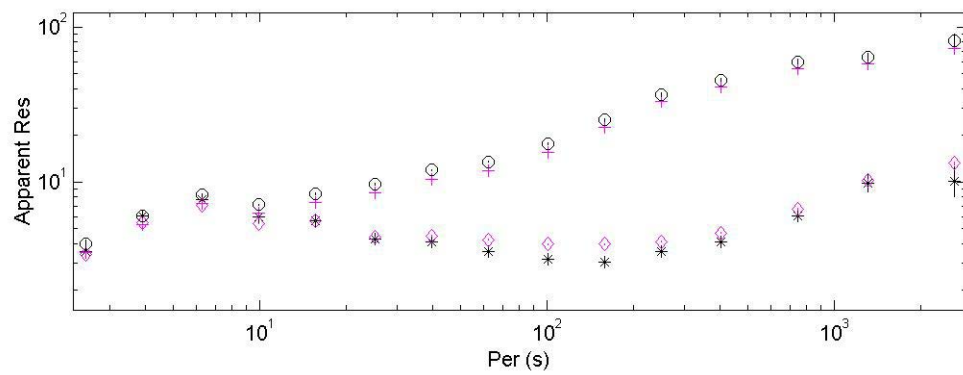
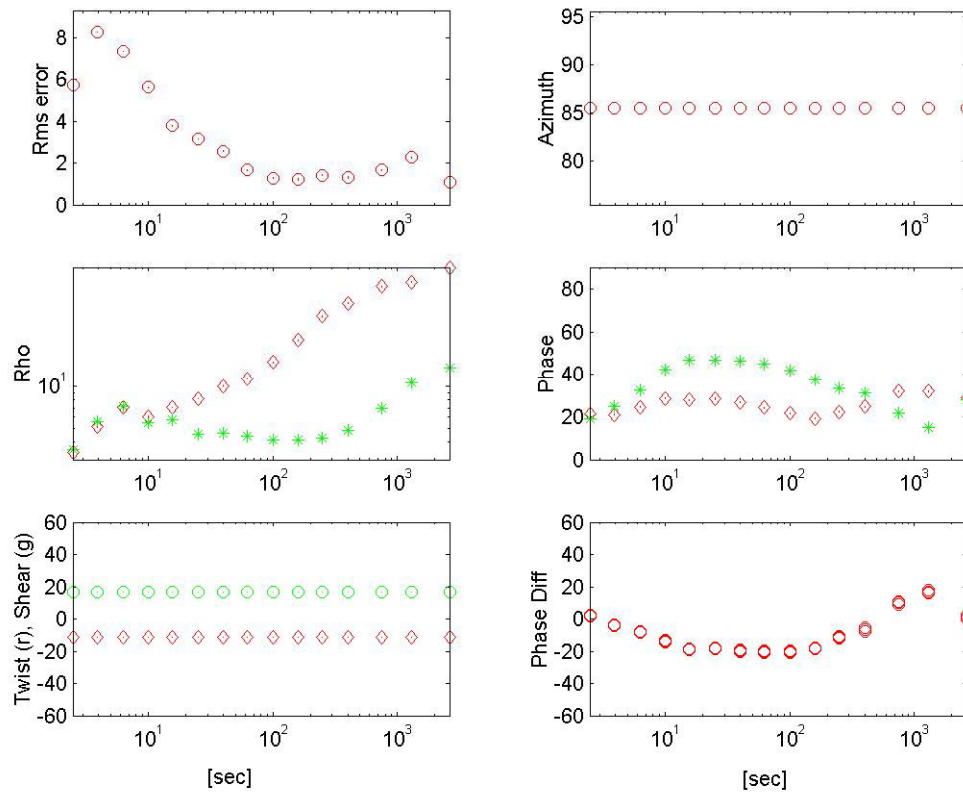
Site S03



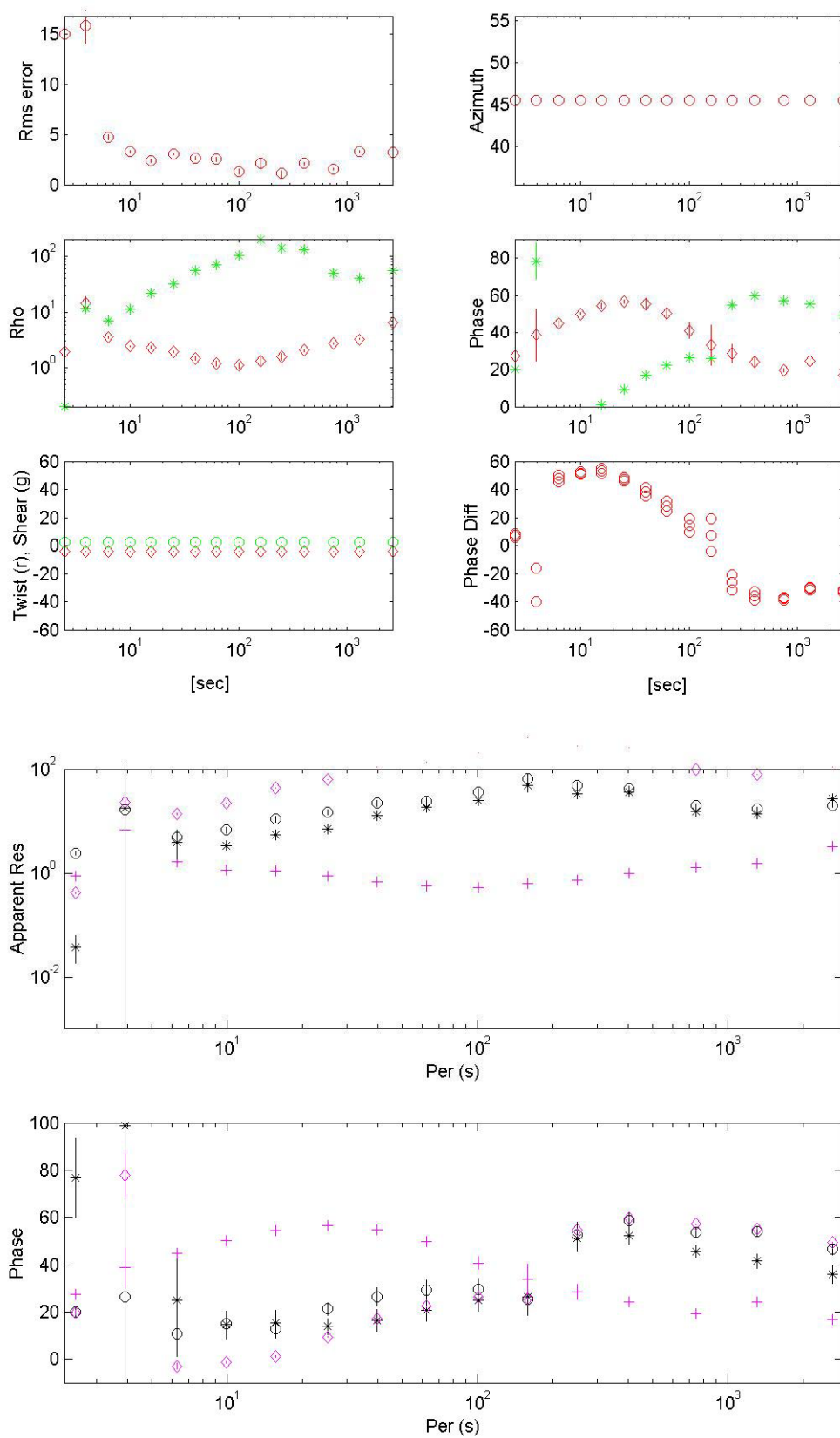
Site S05



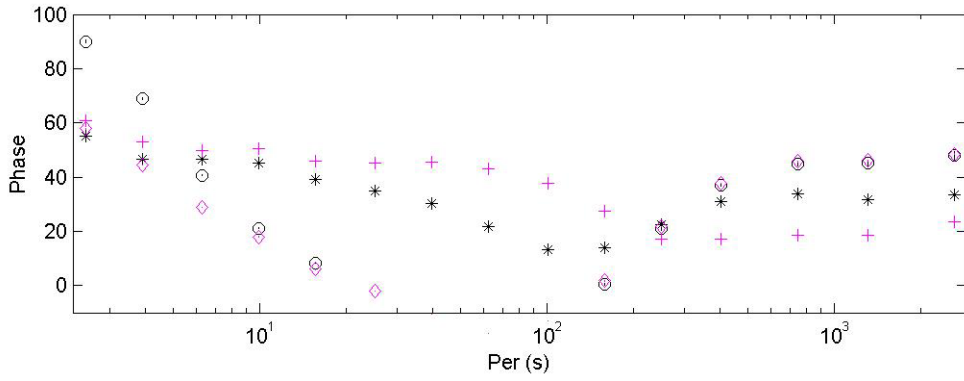
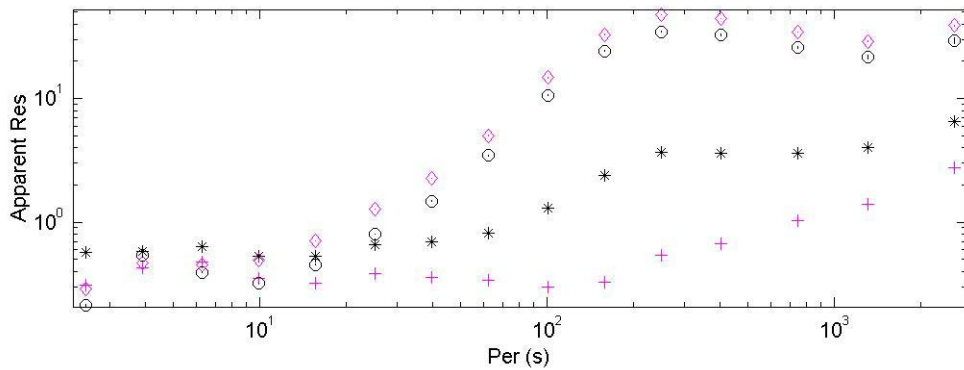
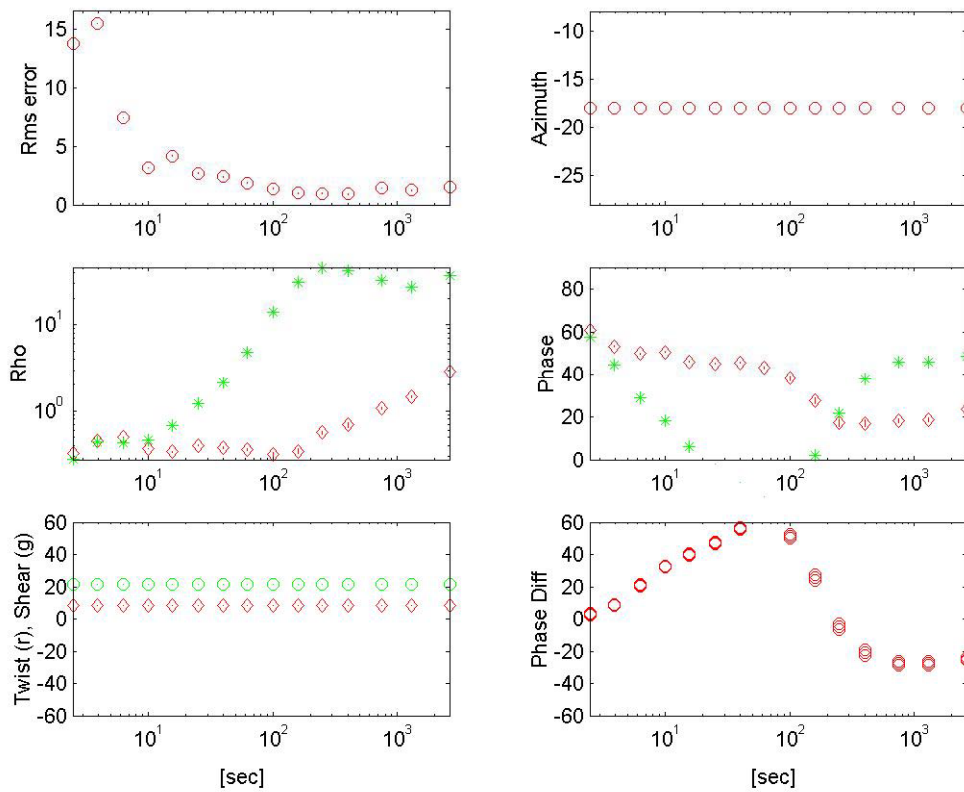
Site S06



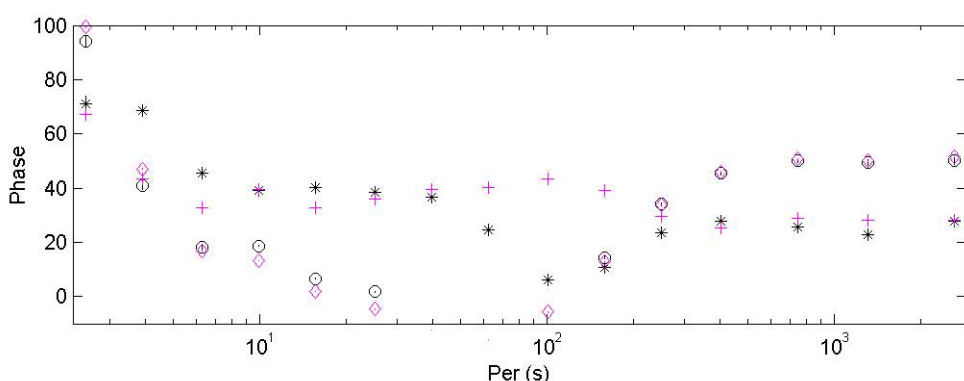
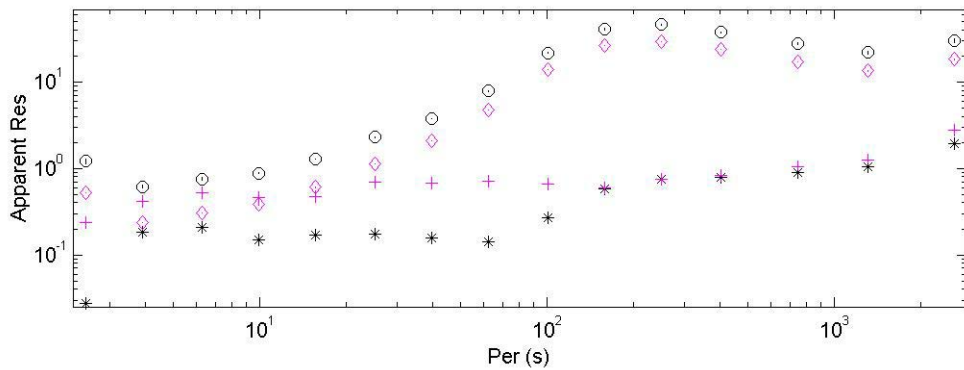
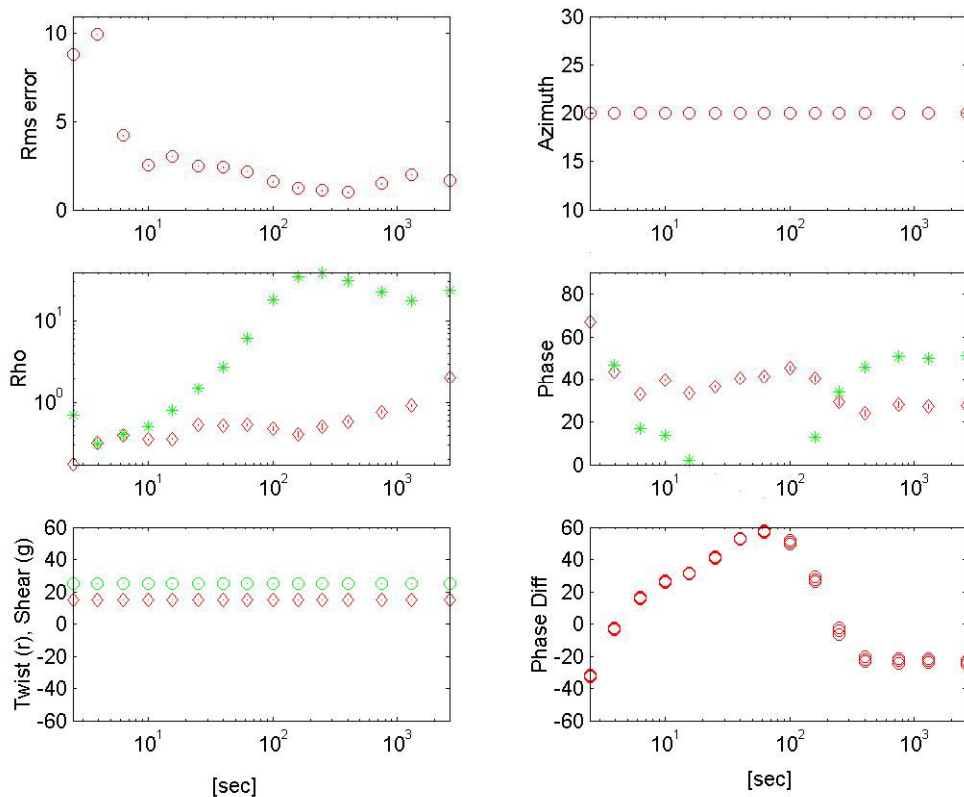
Site S07



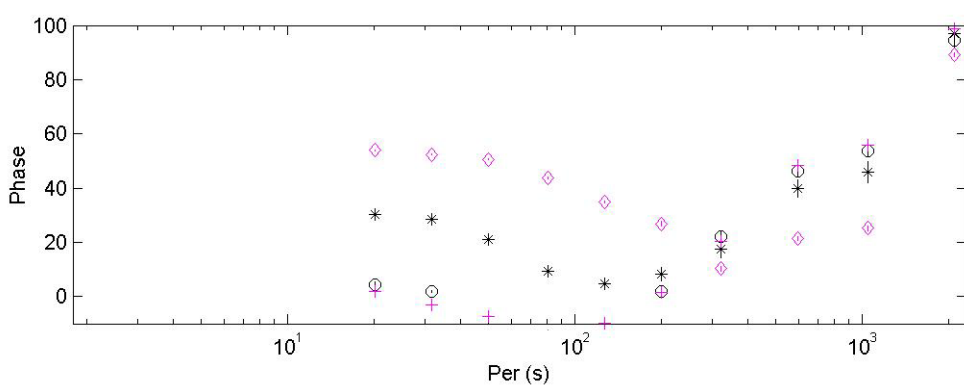
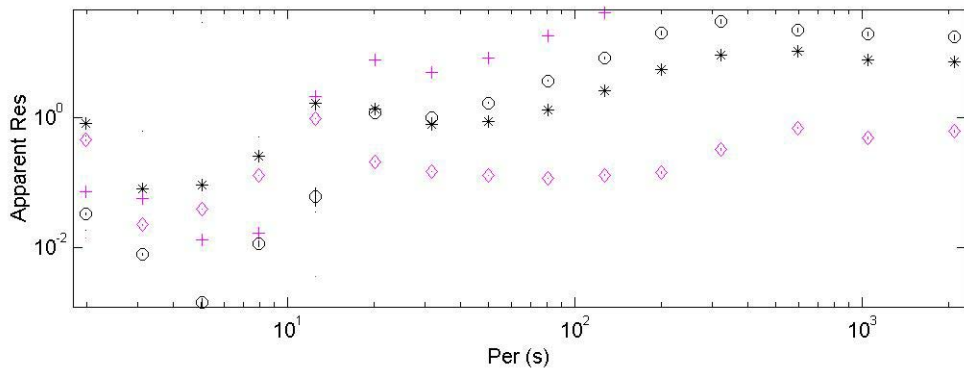
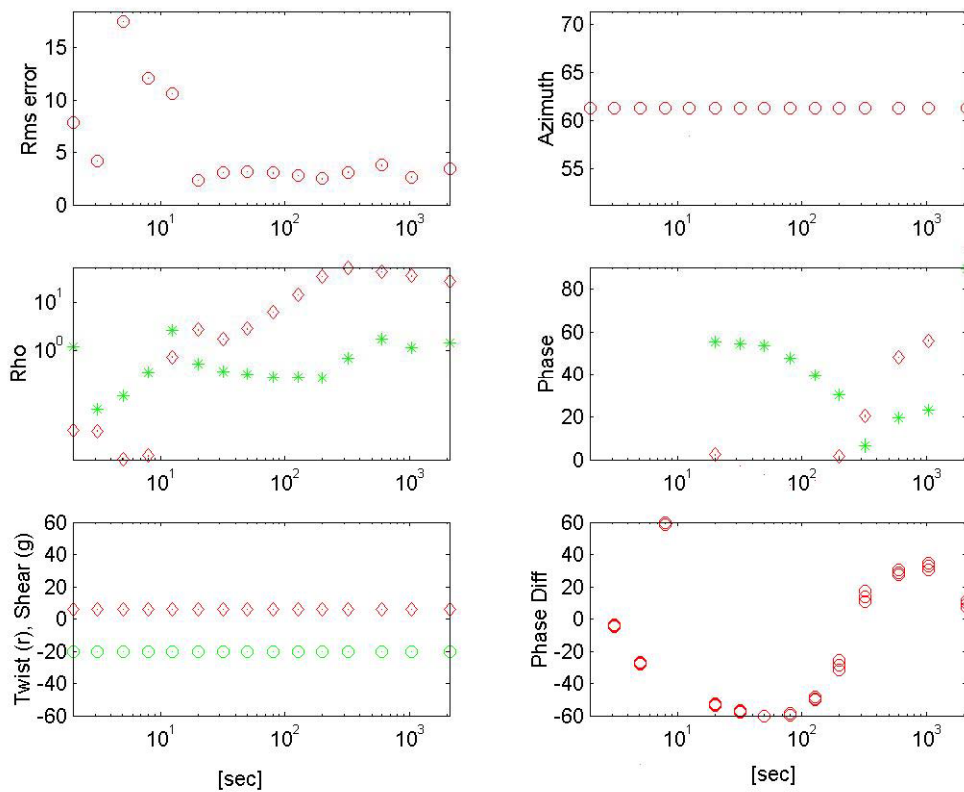
Site S08



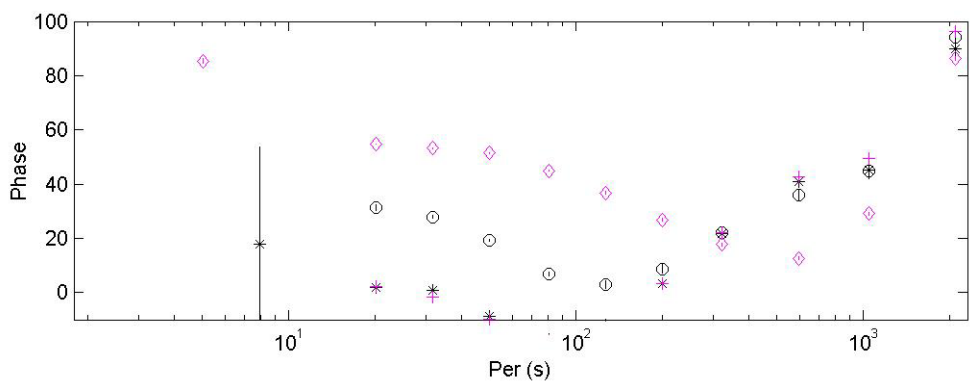
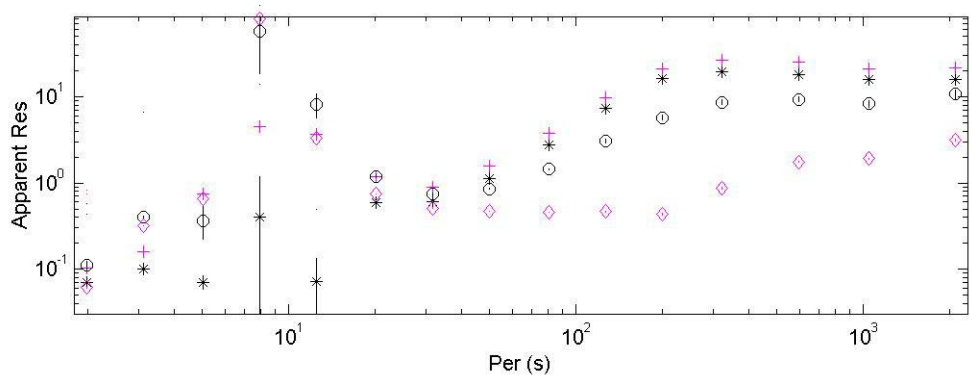
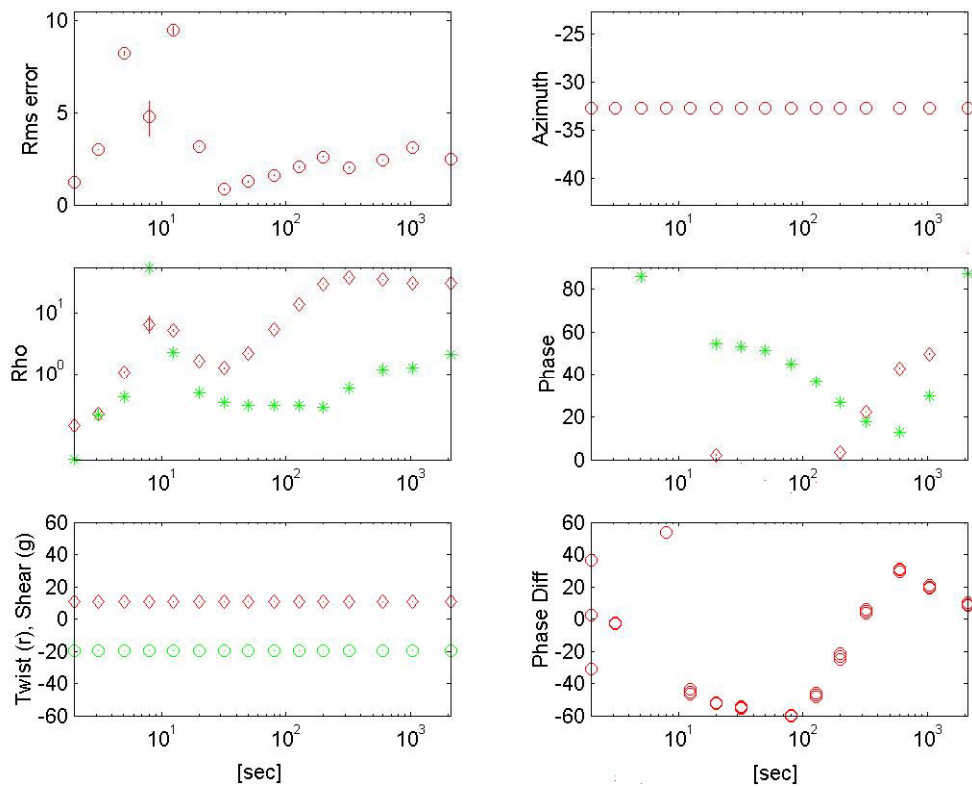
Site S09



Site S10



Site S11



APPENDIX B

APPARENT RESISTIVITY AND PHASE PLOTS

Polar diagrams for each of the seafloor sites used in this investigation.

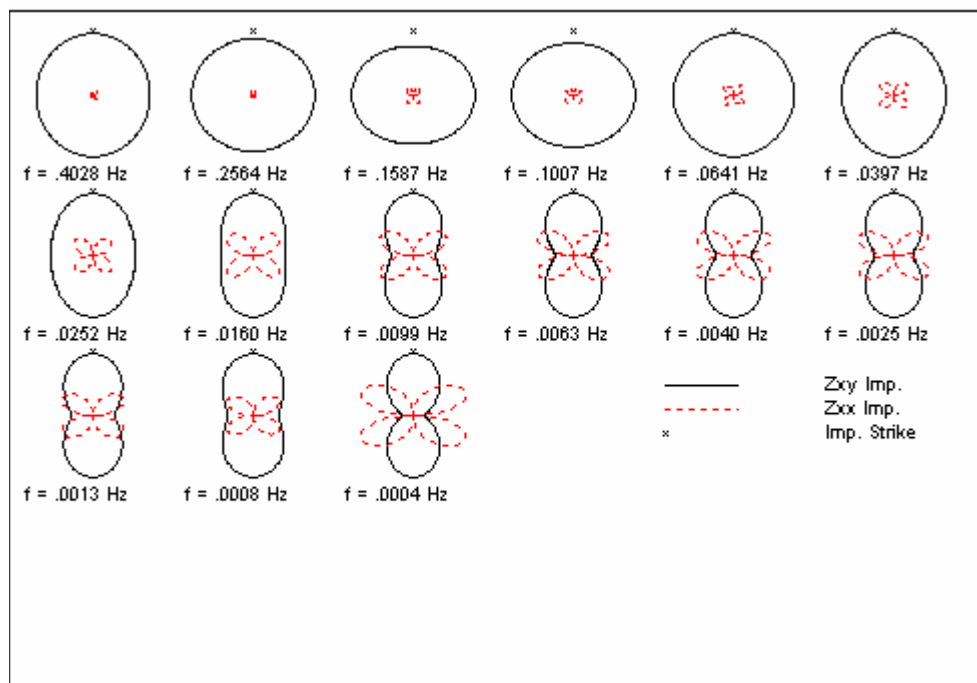


Figure 43. Polar diagram of site S01.

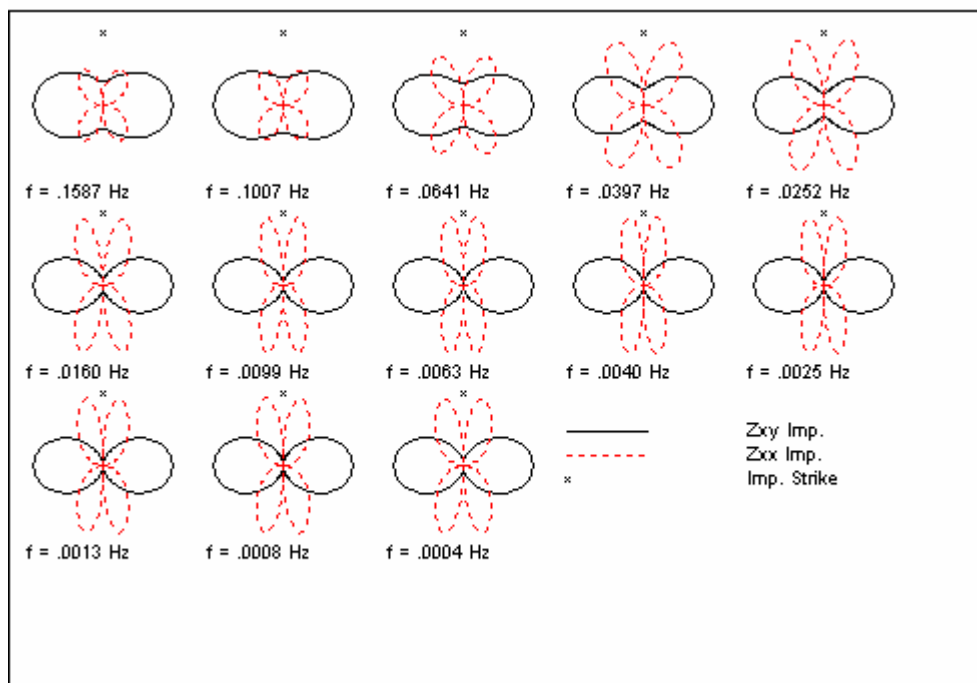


Figure 44. Polar diagram of site S02.

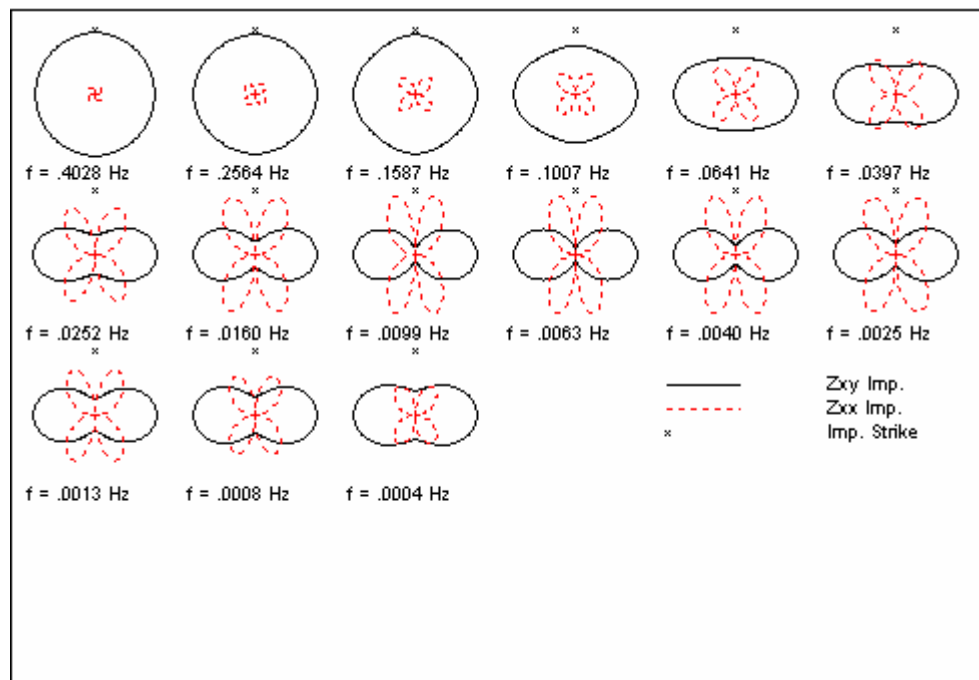


Figure 45. Polar diagram of site A02.

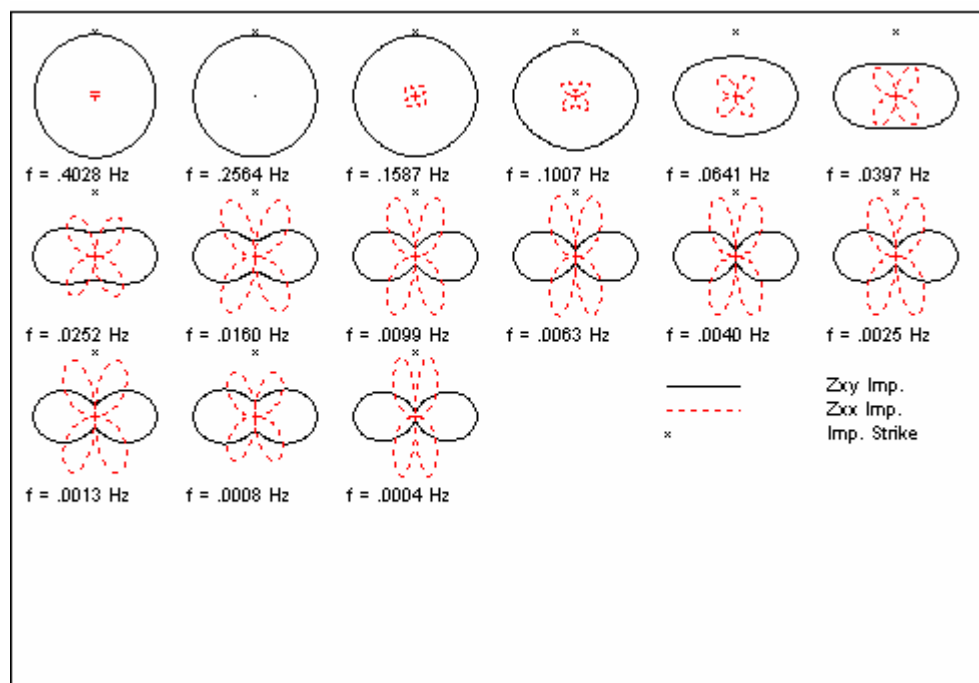


Figure 46. Polar diagram of site S03.

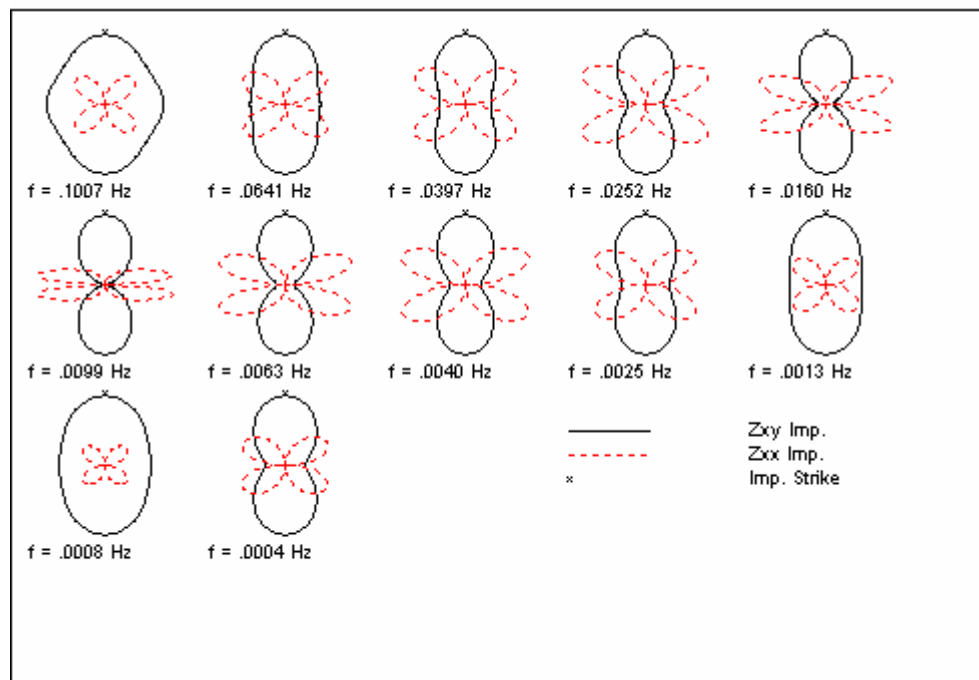


Figure 47. Polar diagram of site S05.

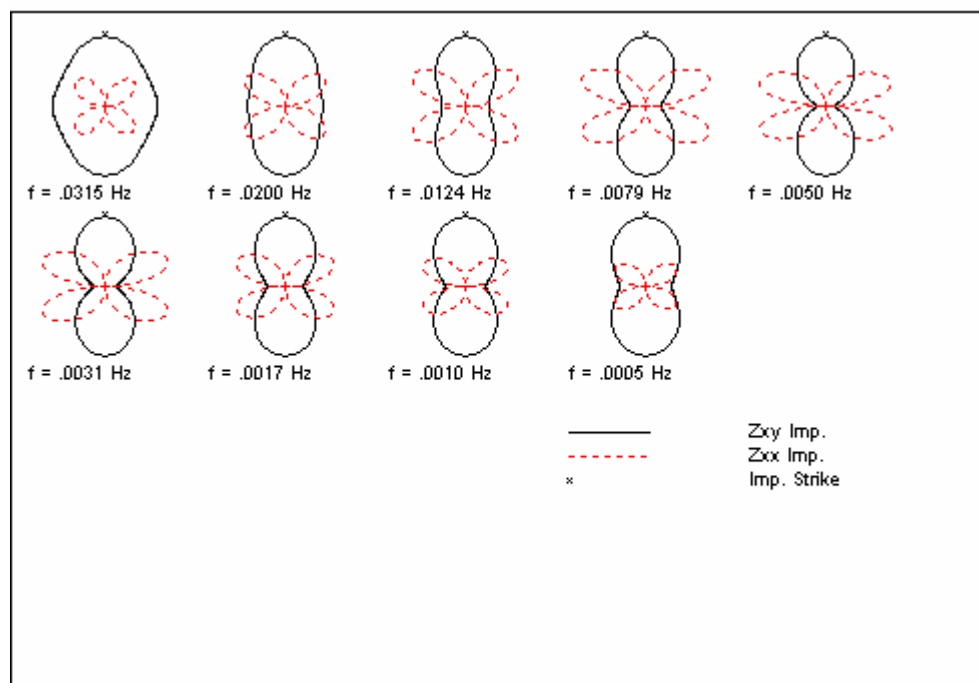


Figure 48. Polar diagram of site S11.

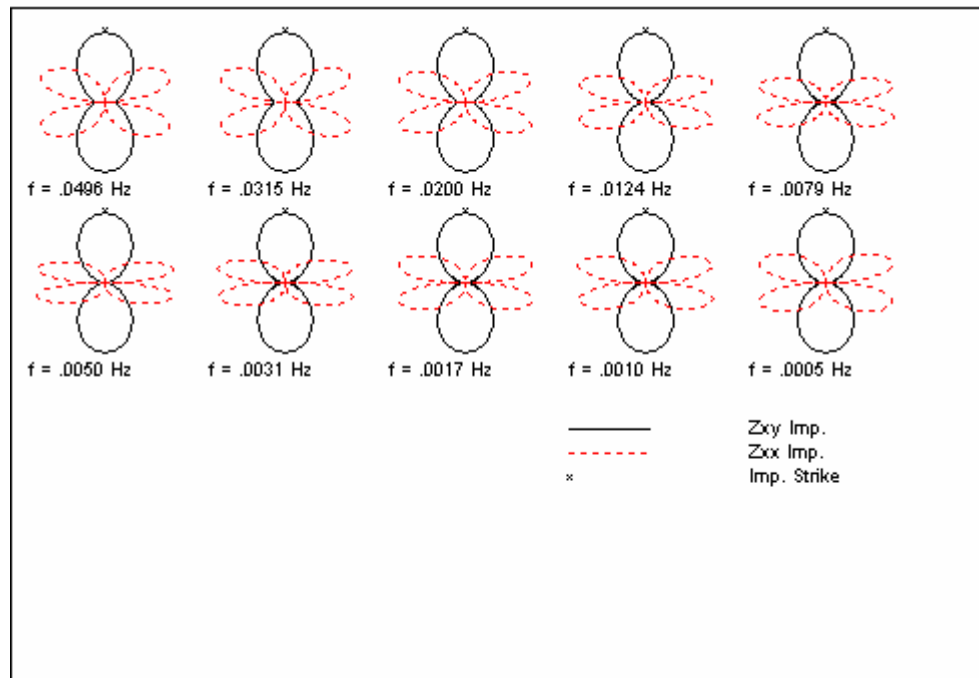


Figure 49. Polar diagram of site S10.

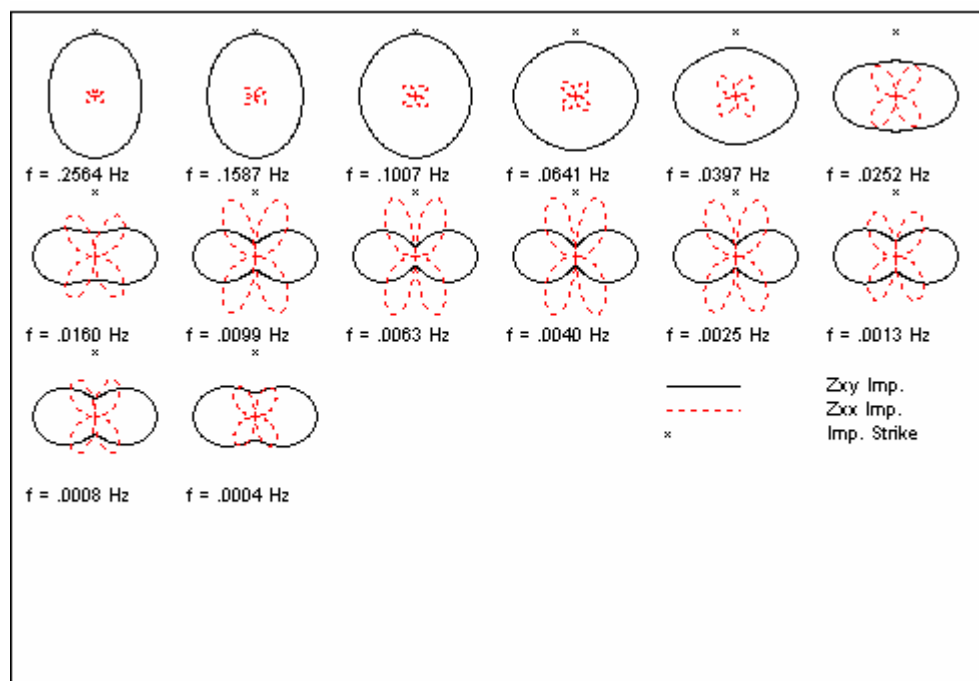


Figure 50. Polar diagram of site S09.

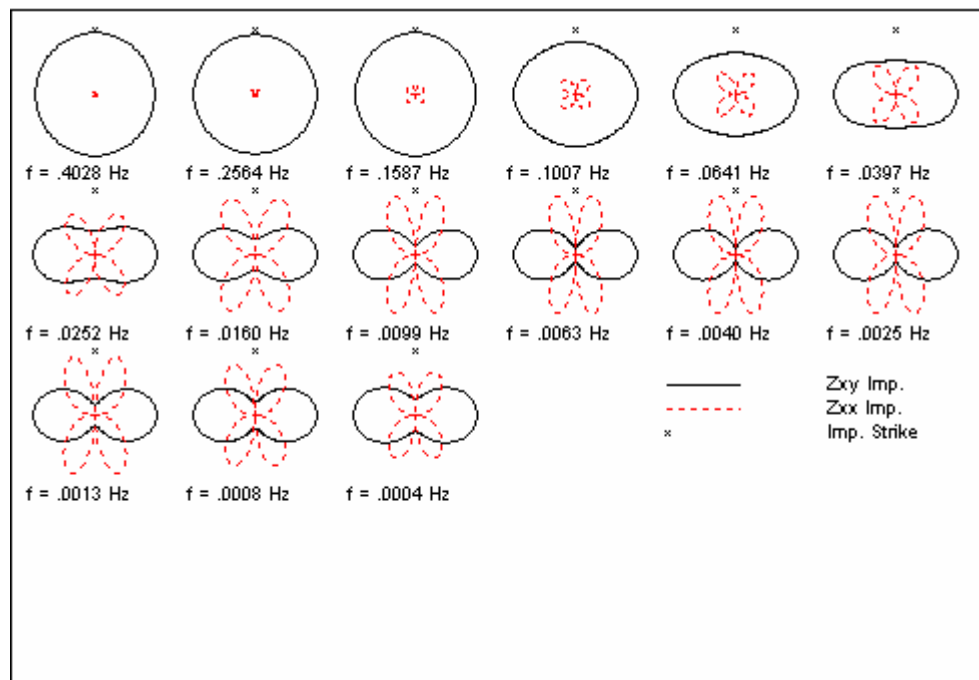


Figure 51. Polar diagram of site S08.

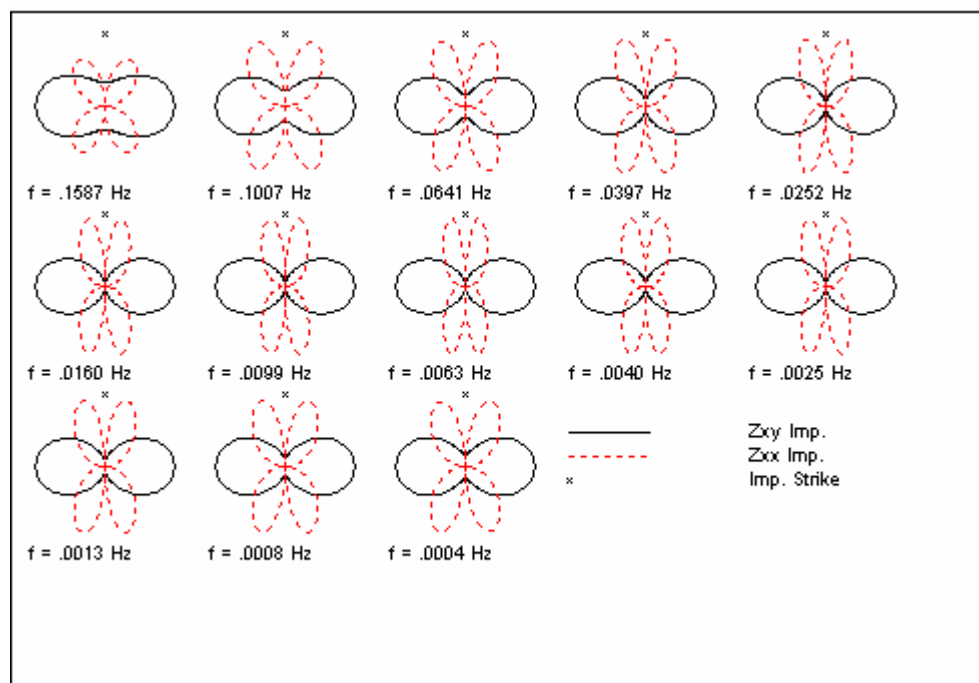


Figure 52. Polar diagram of site S07.

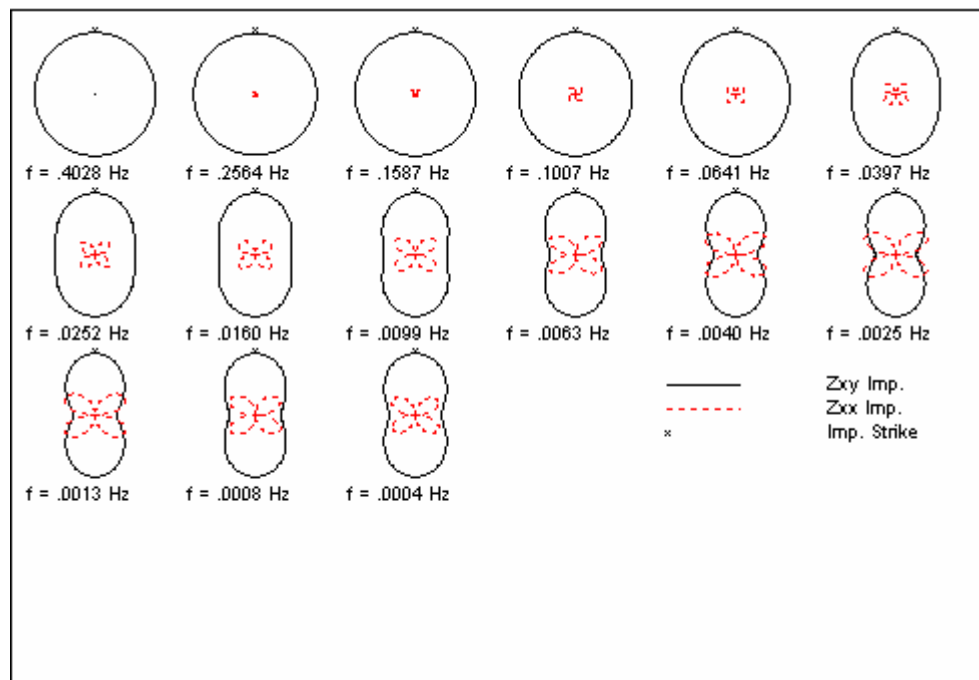


Figure 53. Polar diagram of site S06.

APPENDIX C

DATA FITS

The fits of the preferred model to the raw data are detailed below in the following ten figures, from west to east along the SDT MMT profile.

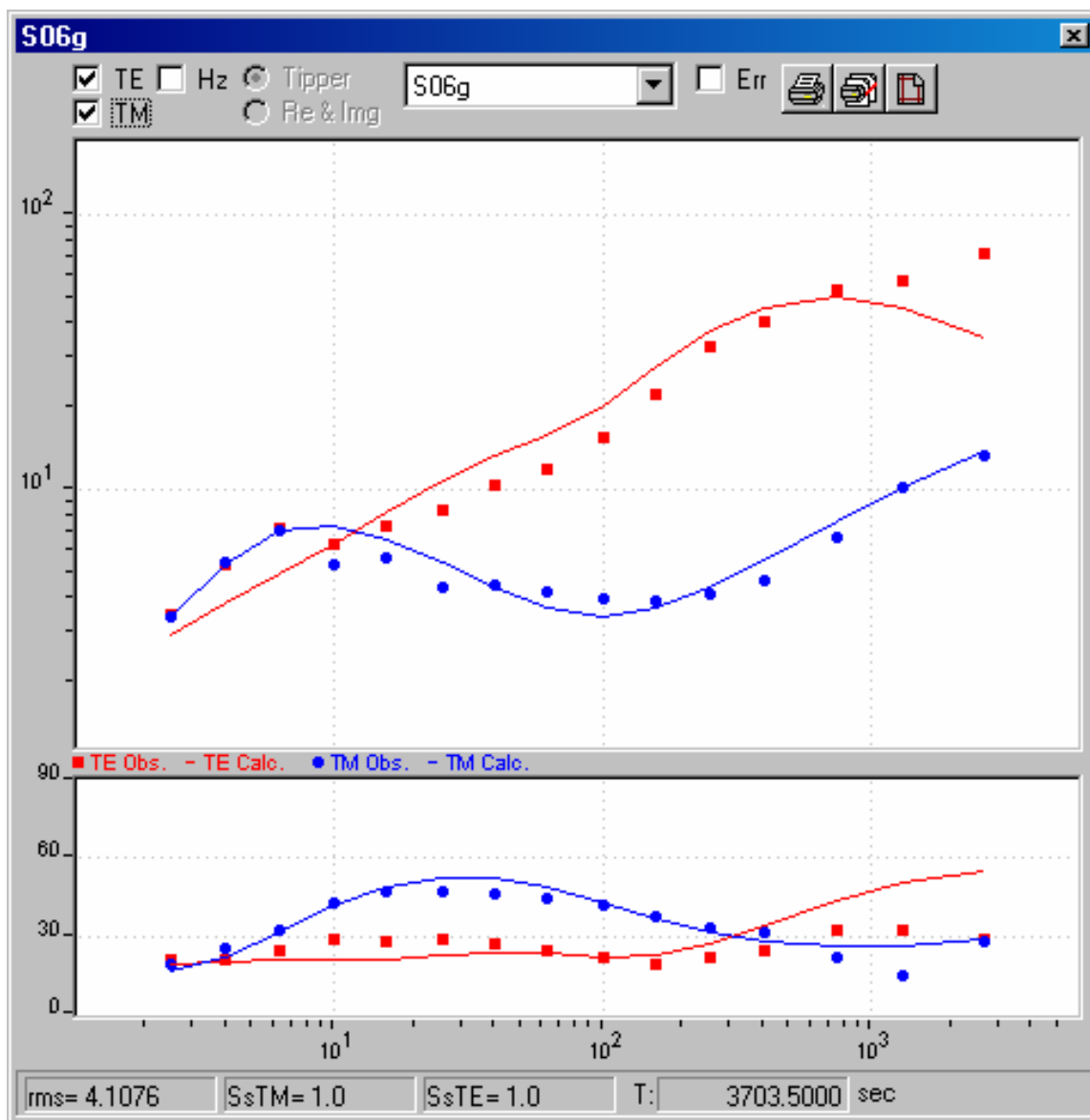


Figure 54. Site S06 (westernmost site), with TE in red and TM in blue. The RMS misfit for this site is 4.11

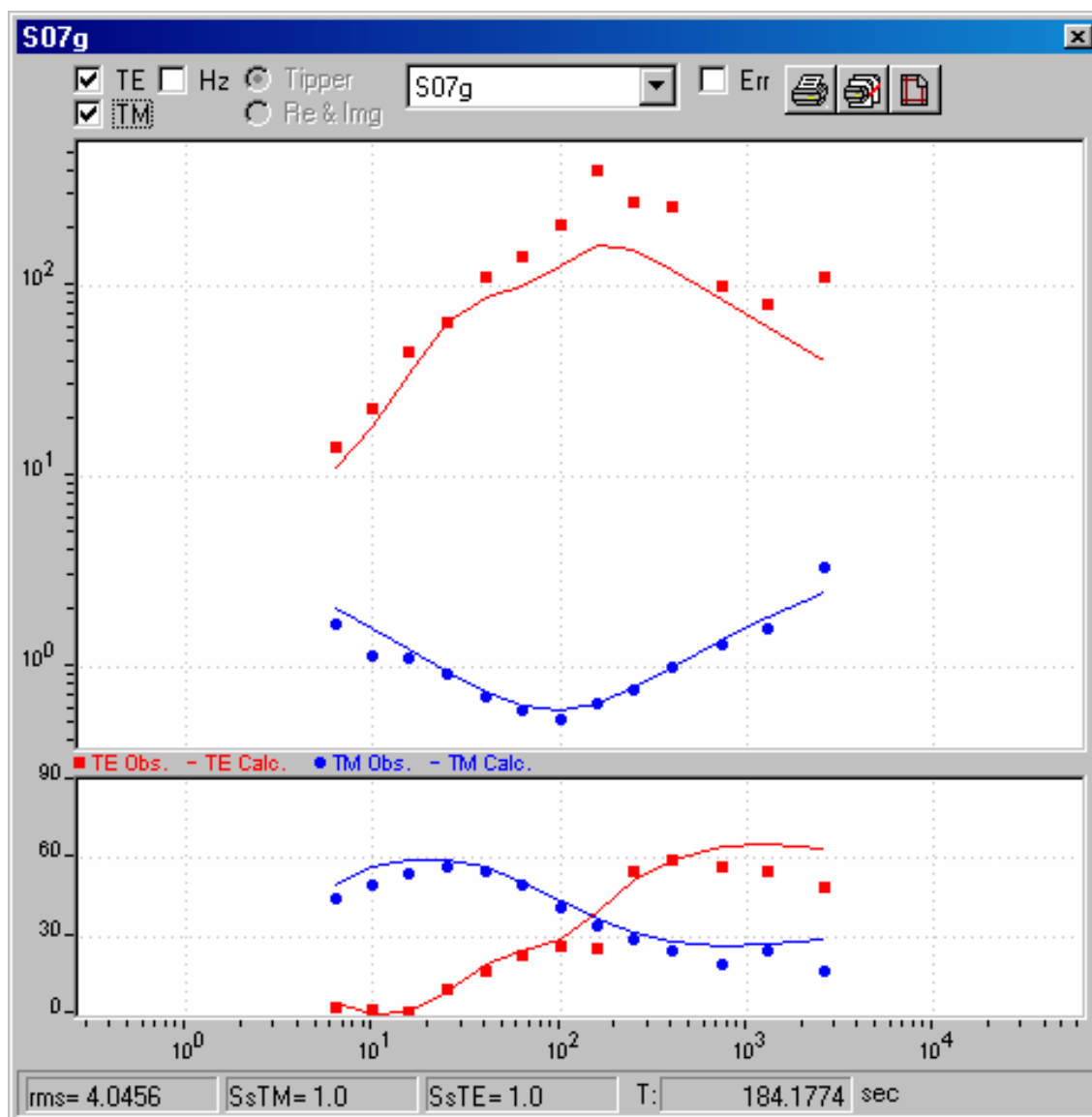


Figure 55. Site S07, with TE in red and TM in blue. The RMS misfit for this site is 4.04

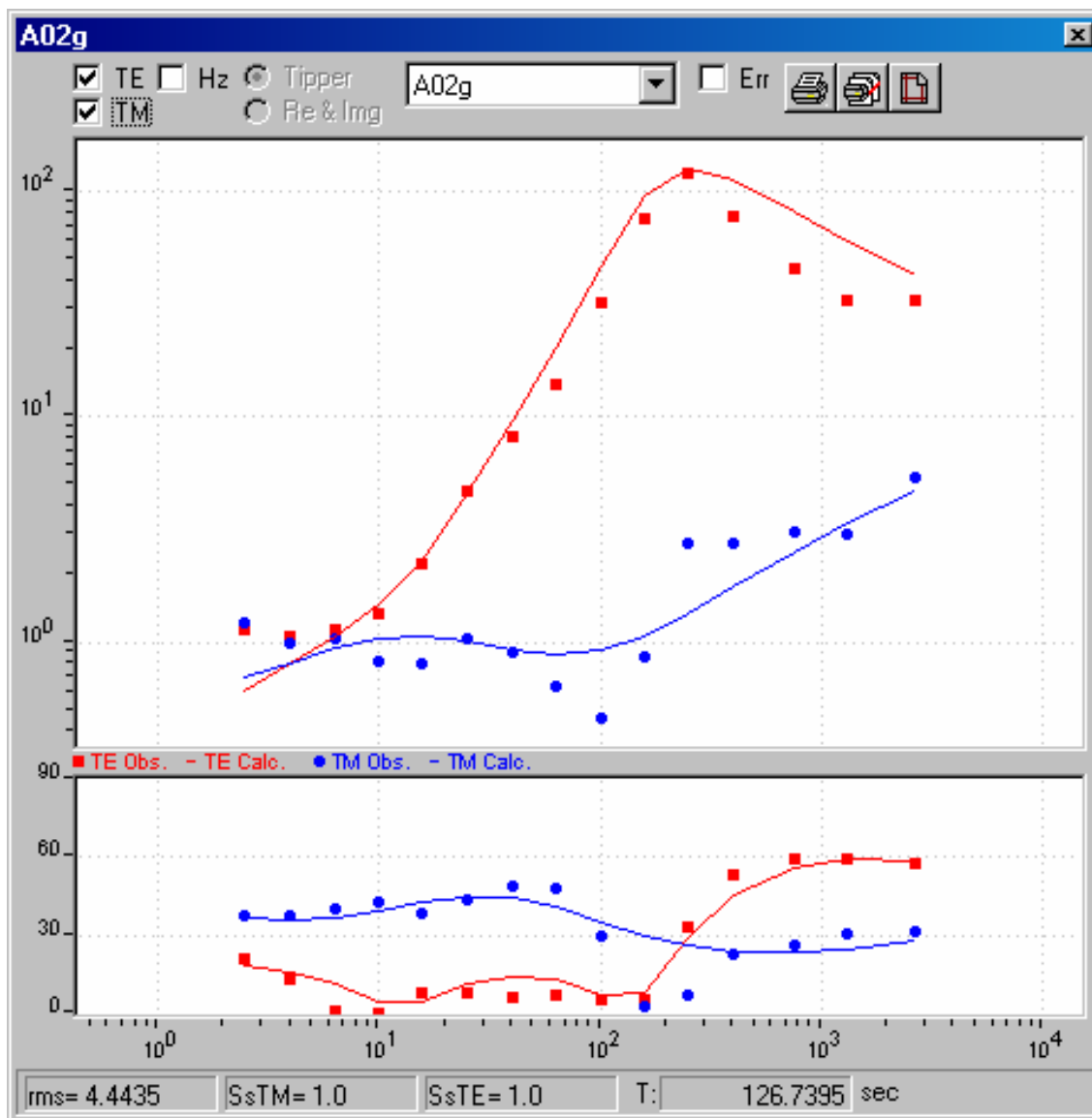


Figure 56. Site A02, with TE in red and TM in blue. The RMS misfit for this site is 4.44.

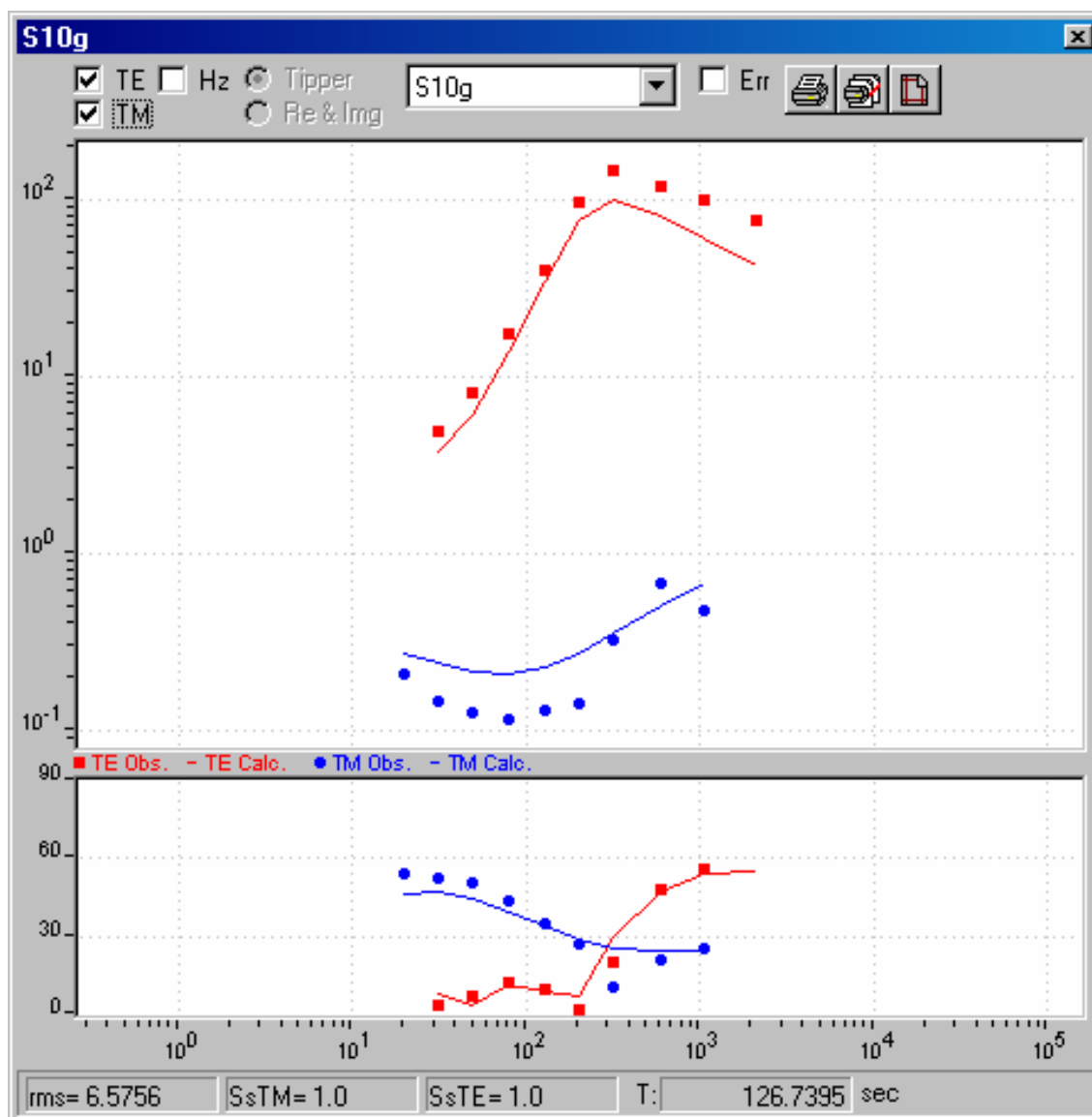


Figure 57. Site S10, with TE in red and TM in blue. The RMS misfit for this site is 6.57.

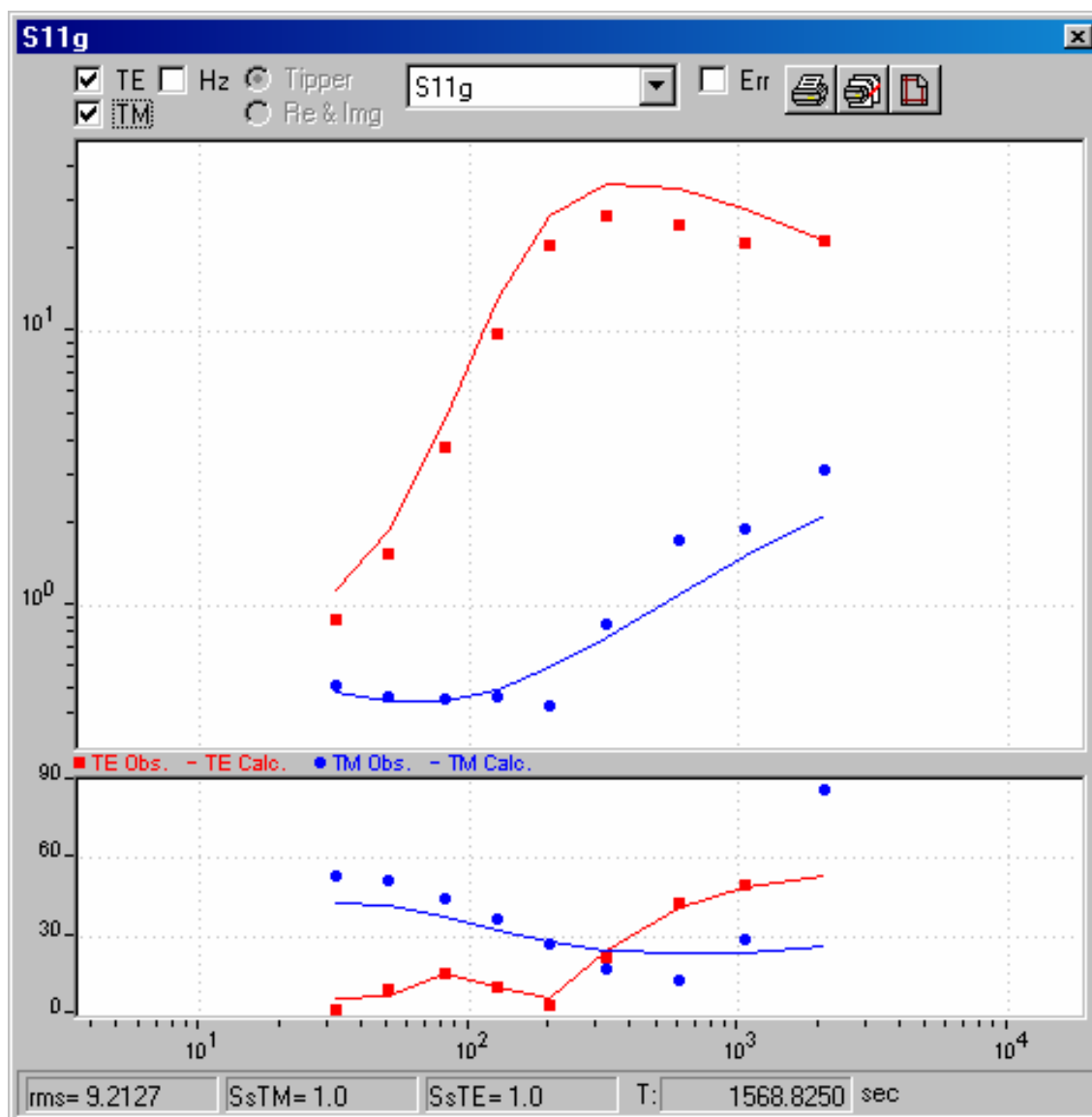


Figure 58. Site S11, with TE in red and TM in blue. The RMS misfit for this site is 9.21.

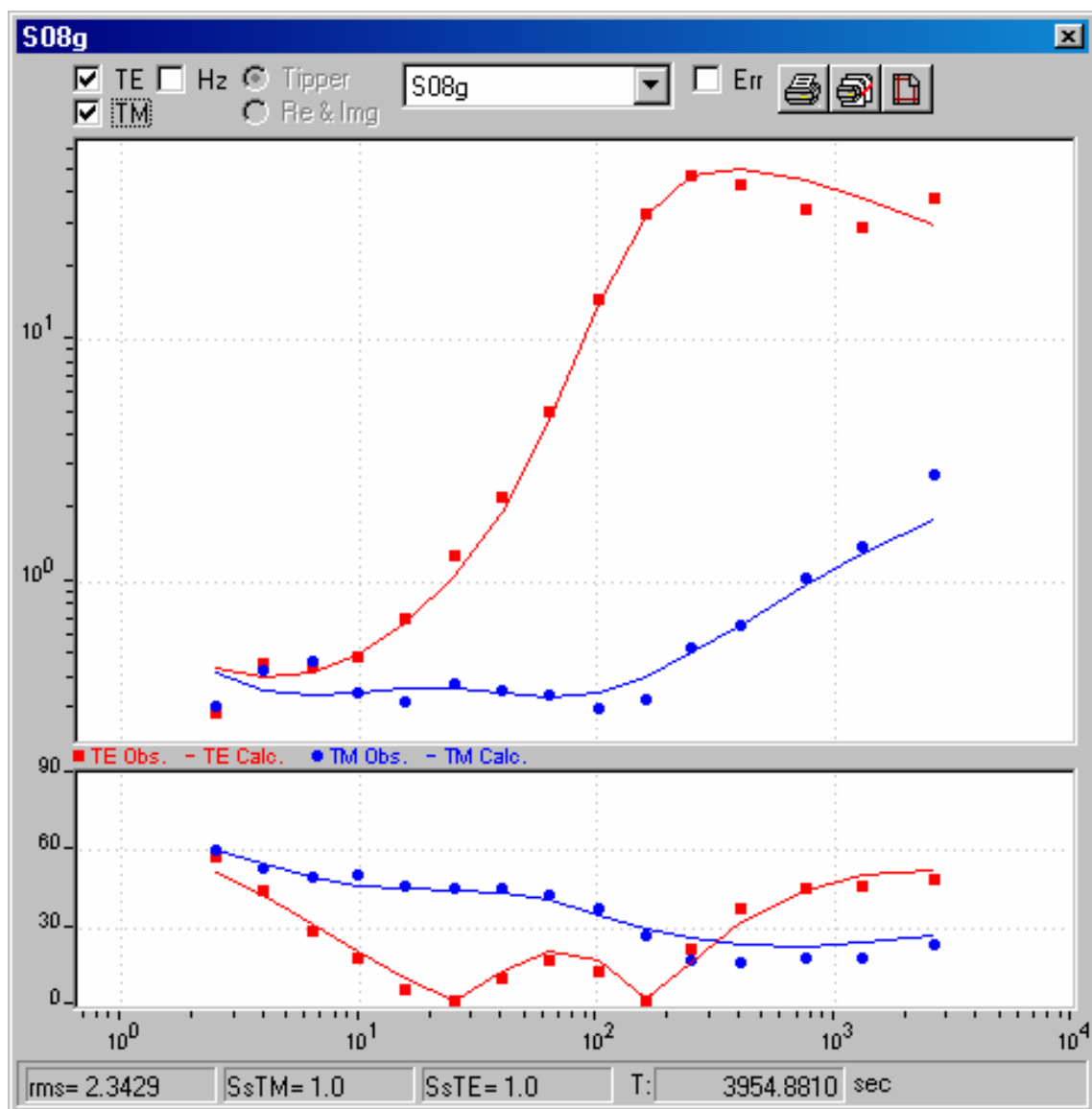


Figure 59. Site S08, with TE in red and TM in blue. The RMS misfit for this site is 2.34.

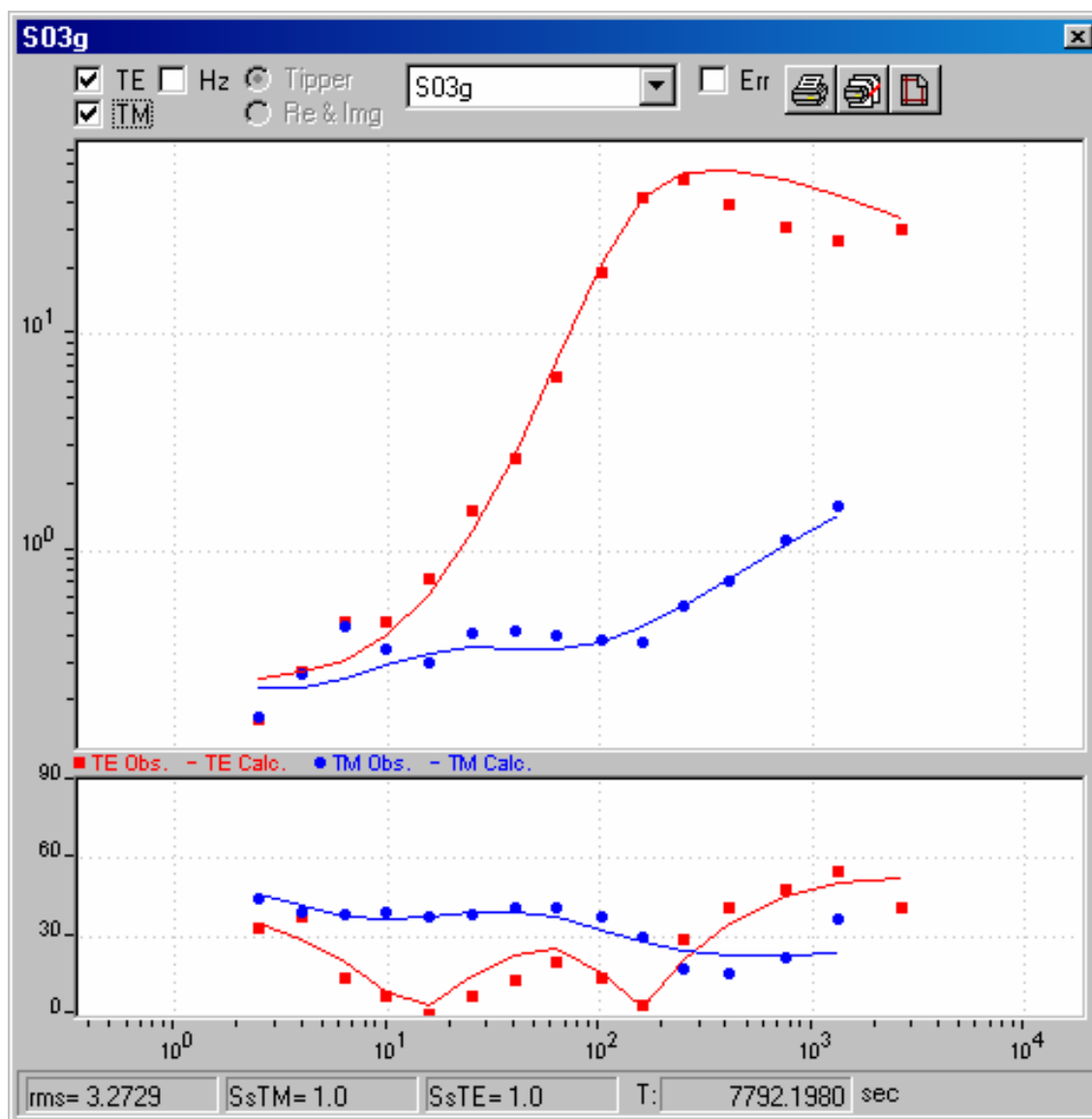


Figure 60. Site S03, with TE in red and TM in blue. The RMS misfit for this site is 3.27.

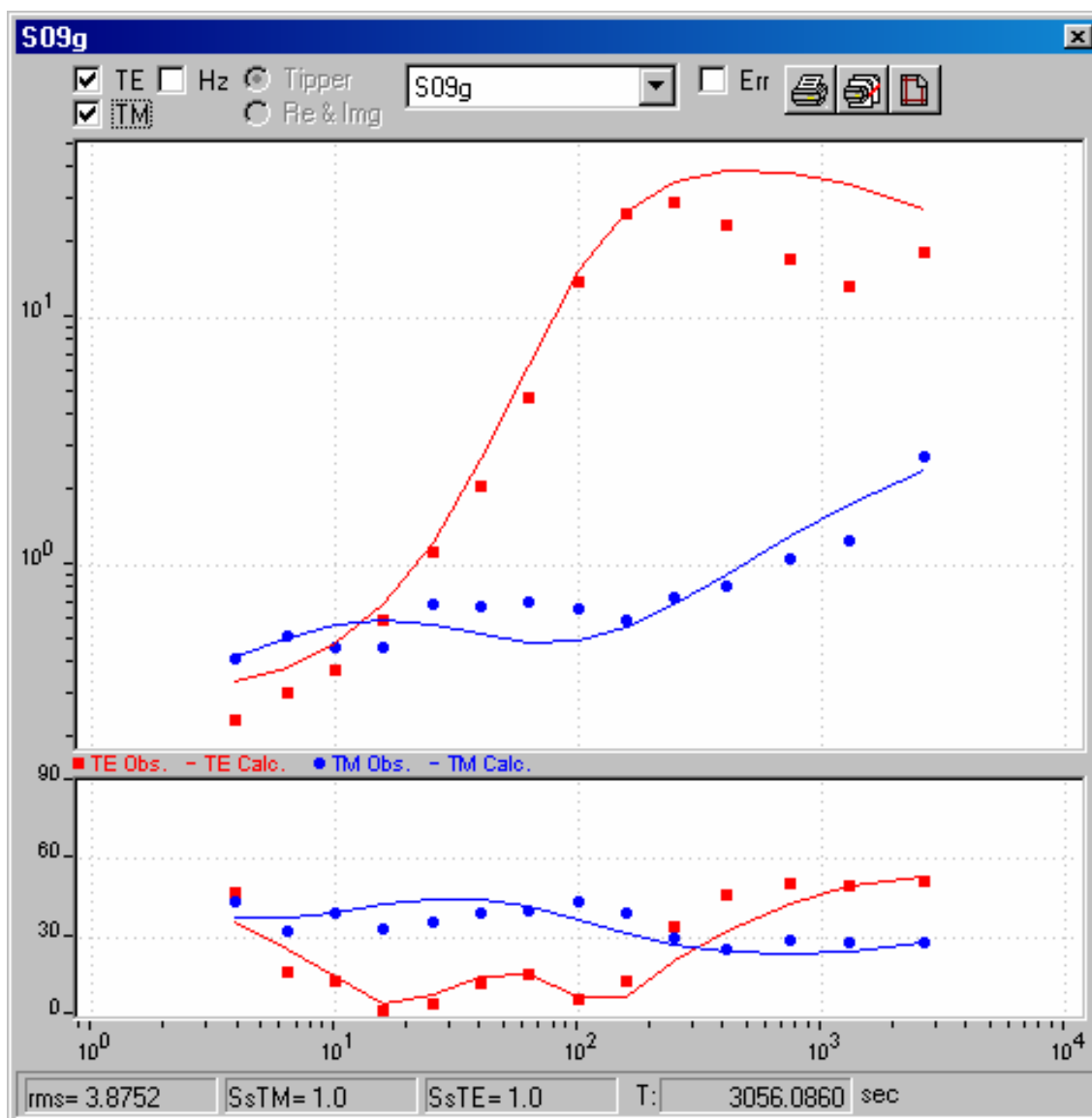


Figure 61. Site S09, with TE in red and TM in blue. The RMS misfit for this site is 3.87.

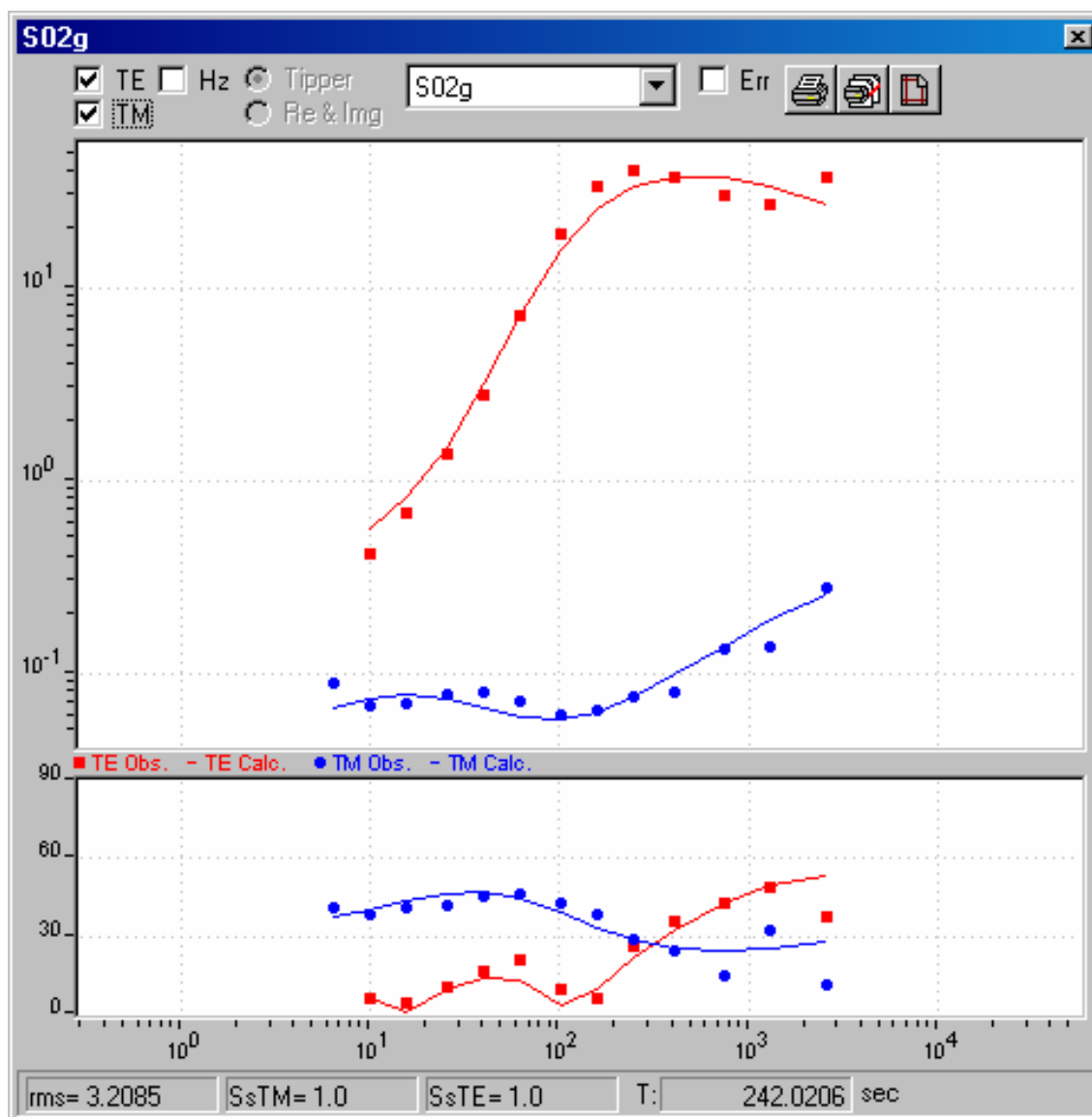


Figure 62. Site S02, with TE in red and TM in blue. The RMS misfit for this site is 3.21.

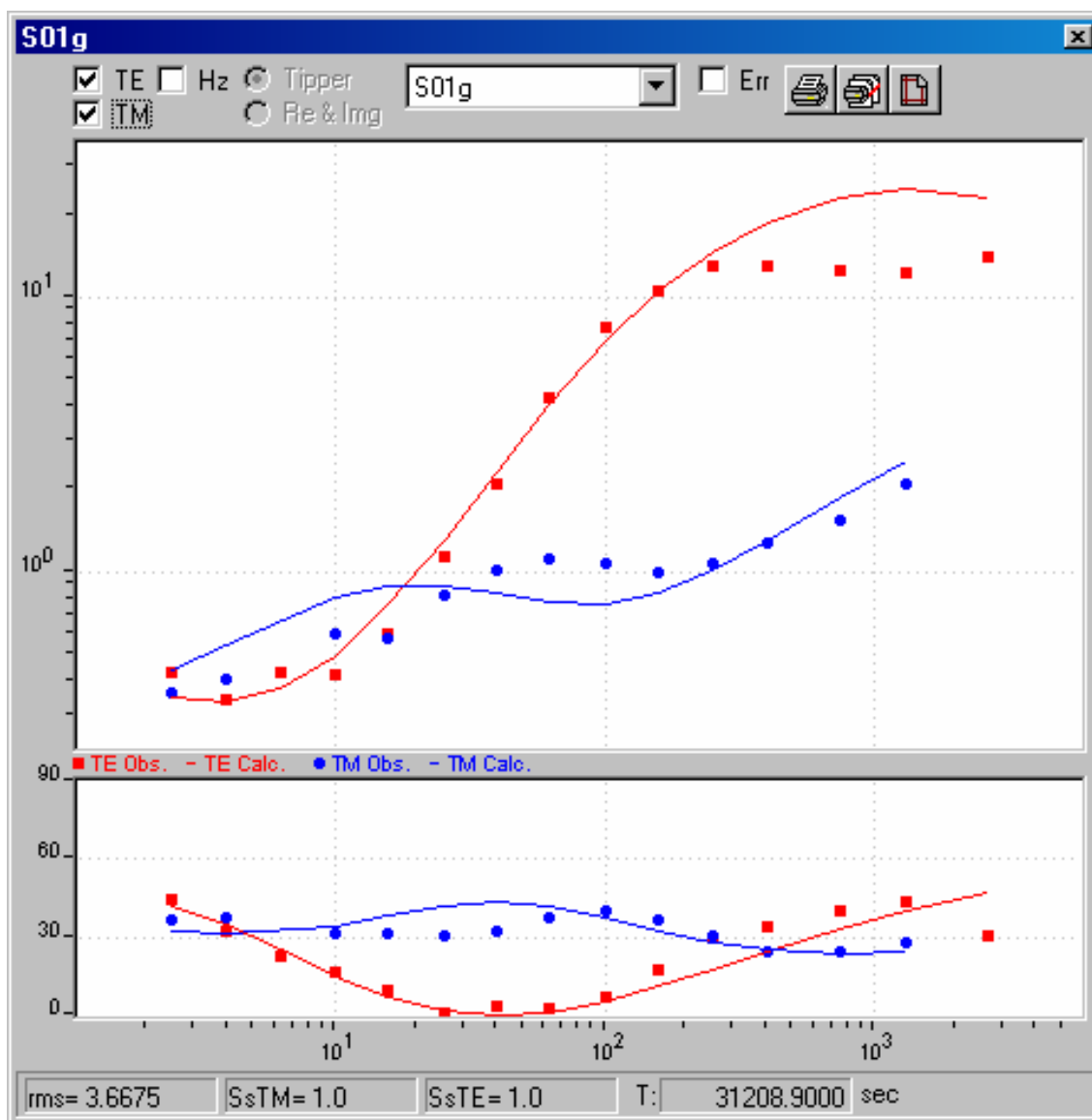


Figure 63. Site S01, with TE in red and TM in blue. The RMS misfit for this site is 3.66.

ABSTRACT OF THE THESIS

A Marine Magnetotelluric Study of the San Diego Trough,
Pacific Ocean, USA

by

Lisl Laura Lewis
Master of Science in Geological Sciences
San Diego State University, 2005

Several expeditions to the San Diego Trough (SDT) offshore San Diego resulted in the acquisition of ten marine magnetotelluric (MMT) seafloor sites in a profile across the SDT. The MMT method measures the passive electric and magnetic signals from the Earth's interaction with the Sun, and results in calculations of the subsurface resistivity at the location of the seafloor sites.

The SDT is an 1100 m deep basin located 30 miles west of the city of San Diego and flanked by the Thirtymile Bank to the west and the Coronado Bank to the east. These bathymetric features are part of the California continental borderland, the broad tectonic plate boundary between the Pacific and North American plates. Previous geophysical and geological studies conducted in the region have resulted in the mapping and interpretation of the shallow (top 2-3 km below the seafloor) geologic structure, but no studies have been able to image the deeper structure of the SDT area.

The data from this MMT investigation suggest a geoelectric structure that agrees with the seismic data in the top 2-3 km but introduces new evidence for deeper structure. Several faults are identified in the San Diego Trough and evidence suggests that the Coronado Bank Fault Zone is active, perhaps similar to the "creeping" segment of the San Andreas Fault in Parkfield, California.